

AN ABSTRACT OF THE THESIS OF

Daniel Melendy for the degree of Master of Science in

Electrical and Computer Engineering presented on November 22, 2002.

Title: Modelling of On-Chip Spiral Inductors for Silicon RFICs.

Abstract approved: _____

Redacted for privacy

Andreas Weisshaar

In high-frequency circuit design, performance is often limited by the quality of the passive components available for a particular process. Specifically, spiral inductors can be a major bottle-neck for Voltage-Controlled Oscillators (VCOs), Low-Noise Amplifiers (LNAs), mixers, etc. For designers to correctly optimize a circuit using a spiral inductor, several frequency-domain characteristics must be known including the quality factor (Q), total inductance, and the self-resonant frequency. This information can be difficult to predict for spirals built on lossy silicon substrates because of the complicated frequency-dependent loss mechanisms present.

The first part of this research addresses the need for a scalable, predictive model for obtaining the frequency domain behavior of spiral inductors on lossy silicon substrates. The technique is based on the Partial Element Equivalent Circuit (PEEC) method and is a flexible approach to modelling spiral inductors. The basic PEEC technique is also enhanced to efficiently include the frequency dependent eddy-currents in the lossy substrate through a new complex-image method. This enhanced PEEC approach includes all of the major non-ideal effects including the conductor-skin and proximity effects, as well as the substrate-skin effect. The

approach is applied to octagonal spiral inductors and comparisons with measurements are presented.

To complement the scalable enhanced-PEEC model, a new wide-band compact equivalent circuit model is presented which is suitable for time-domain simulations. This model achieves wide-band accuracy through the use of “transformer-loops” to model losses caused by the magnetic field. A fast extraction technique based on a least squares fitting procedure is also described. Results are presented for a transformer-loop compact model extracted from measurements.

The combination of an accurate scalable model and a wide-band compact equivalent-circuit model provides a complete modelling methodology for spiral inductors on lossy silicon.

©Copyright by Daniel Melendy

November 22, 2002

All rights reserved

Modelling of On-Chip Spiral Inductors for Silicon RFICs

by

Daniel Melendy

A THESIS

submitted to

Oregon State University

in partial fulfillment of
the requirements for the
degree of

Master of Science

Presented November 22, 2002
Commencement June 2003

Master of Science thesis of Daniel Melendy presented on November 22, 2002

APPROVED:

Redacted for privacy

Major Professor, representing Electrical and Computer Engineering

Redacted for privacy

Chair of the Department of Electrical and Computer Engineering

Redacted for privacy

Dean of the Graduate School

I understand that my thesis will become part of the permanent collection of Oregon State University libraries. My signature below authorizes release of my thesis to any reader upon request.

Redacted for privacy

Daniel Melendy, Author

ACKNOWLEDGMENTS

A heartfelt thank you to my wife, Holly, whose unconditional support, love, and guidance has been a constant source of inspiration to me to be successful in my educational endeavors as well as life in general.

I would also like to thank my major professor, Dr. Andreas Weisshaar. He provided me the opportunity to do this research and shared a great deal of his time and thoughts on my work. His guidance, encouragement, and support through my years at Oregon State University have made possible the completion of this thesis work.

I would also like to thank Dr. Raghu Kumar Settaluri, my minor professor, for his help as well as the wonderful lectures he gave in class.

Thanks is due to Dr. Tom Plant and Graduate Council Representative Dr. Bruce D'Ambrosio for serving on my graduate committee, reviewing the manuscript, and giving suggestions.

Thanks to my colleagues, Amy Luoh, Hai Lan, and Ji Zheng, for their encouragement, useful discussions, contributions to this work, and invaluable friendships.

Thanks must also be given to National Semiconductor Corporation for its generous support with measurement data.

Finally, thanks to Ferne Simendinger and Sarah O'Leary for their help throughout my years at OSU.

TABLE OF CONTENTS

	<u>Page</u>
1 INTRODUCTION	1
1.1 Background and Motivation	1
1.2 Loss Mechanisms of Spiral Inductors on Silicon Substrates	3
1.2.1 Electric Field Losses	4
1.2.2 Magnetic Field Losses	4
1.3 Spiral Inductor Improvements	7
1.4 Conventional Characterization and Modelling Techniques	9
1.5 Organization of the Study	11
2 SCALABLE MODELLING	13
2.1 Introduction	13
2.2 Simplified PEEC Model of Rectangular Spiral Inductor	14
2.2.1 Branch Voltages	21
2.2.2 Partial Resistances	22
2.2.3 Partial Self and Mutual Inductances	22
2.2.4 Partial Capacitances	23
2.2.5 Complete Partial Element Equivalent Circuit	26
2.3 Extensions to the Basic PEEC Model	27
2.3.1 Spiral-Substrate Interaction Through the \vec{H} -Field	28
2.3.2 Conductor Skin and Proximity Effects	36
2.3.3 Spiral-Substrate Coupling Through the \vec{E} -Field	38
2.4 Solution of the Complete Equivalent Circuit	41
2.4.1 RLM Sub-Circuit	44
2.4.2 GC Sub-Circuit	48
2.5 Conclusion	50
3 COMPACT EQUIVALENT-CIRCUIT MODELLING	52

TABLE OF CONTENTS (Continued)

	<u>Page</u>
3.1 Introduction.....	52
3.2 Frequency Domain Trends of Spiral Inductors.....	53
3.3 Nine-Element Compact Model.....	57
3.4 Transformer-Loop Compact Model.....	59
3.4.1 Series Circuit.....	60
3.4.2 Shunt Circuit.....	61
3.5 Extraction Procedure.....	62
3.5.1 Series Circuit.....	63
3.5.2 Shunt Circuit.....	68
3.6 Conclusion.....	68
4 RESULTS.....	69
4.1 Octagonal Spiral on High-Loss Substrate.....	69
4.1.1 Scalable Model Results.....	70
4.1.2 Compact Model Results.....	74
4.2 Octagonal Spiral on Low-Loss Substrate.....	78
4.3 Conclusion.....	80
5 CONCLUSIONS AND FUTURE RESEARCH.....	83
5.1 Conclusions.....	83
5.2 Future Research.....	84
BIBLIOGRAPHY.....	86
APPENDICES.....	91
APPENDIX A Integral Formulation for PEEC.....	92

TABLE OF CONTENTS (Continued)

	<u>Page</u>
APPENDIX B Automated Layout of Spiral Inductors	94
APPENDIX C Partial Inductance Formulas	103

LIST OF FIGURES

<u>Figure</u>	<u>Page</u>
1.1 Shunt electric field in an on-chip spiral inductor.	5
1.2 Lateral electric field interaction in an on-chip spiral inductor.	6
1.3 Magnetic field interactions related to the proximity and skin effects in an on-chip spiral inductor.	7
1.4 Magnetic field coupling to the lossy substrate.	8
2.1 Single-turn rectangular spiral inductor in free-space.	15
2.2 Ratio of segment length to free-space wavelength for microstrip.	17
2.3 Current directions in inductor structure.	18
2.4 Example charge cell divisions.	19
2.5 Equivalent circuit for single turn inductor.	27
2.6 Single-turn rectangular spiral on lossless substrate.	28
2.7 Coupled segments above perfect ground plane.	29
2.8 Partial inductances of coupled segments as the distance to the ground plane is varied.	30
2.9 Standard Si-SiO ₂ silicon substrate.	31
2.10 Real part of h_{eff} as a function of frequency for various substrate resistivities.	32
2.11 Complex image spiral replacing the lossy substrate.	33
2.12 Frequency dependent partial inductance and resistance of coupled segments on silicon.	34
2.13 Standard epi-layer substrate crosssection.	35
2.14 Skin depth for aluminum conductor.	36
2.15 Sub-division of segments into multiple filaments.	37
2.16 Equivalent circuit including the proximity and conductor skin-effect.	38
2.17 2.5 turn spiral inductor with one- and two nearest-neighbor coupling.	39

LIST OF FIGURES (Continued)

<u>Figure</u>	<u>Page</u>
2.18 Symmetric 3-coupled transmission lines as approximation to spiral inductor segments.	40
2.19 1.25 turn rectangular spiral inductor.	41
2.20 Equivalent circuit for 1.25 turn spiral inductor.	42
2.21 Current and voltage definitions for Y-parameters.	43
2.22 Series R-L-M sub-circuit for 1.25 turn spiral inductor.	45
2.23 G-C coupling sub-circuit for 1.25 turn spiral inductor.	49
3.1 Generic Two-Port Y-parameter Pi-model.	53
3.2 Frequency-dependent pi-model for spiral inductors on silicon substrates.	54
3.3 Trends for $L_{12}(\omega)$ and $R_{12}(\omega)$	55
3.4 Trends for shunt G and C.	57
3.5 Nine-element compact model.	58
3.6 Trends for L12 and R12 for the 9 element model.	59
3.7 Wide-band compact equivalent-circuit model for spiral inductors on lossy substrates.	60
3.8 Trends for L12 and R12 for the transformer-loop model.	61
3.9 Trends for $C_{X0}(\omega)$ and $G_{X0}(\omega)$ for the C-GC shunt circuit.	62
3.10 Pole-zero map for the series circuit of the transformer-loop model.	67
4.1 Layout of the 3.5 turn, 2.0 nH, octagonal spiral inductor on high-loss substrate.	69
4.2 $L_{11}(\omega)$ and $R_{11}(\omega)$ for the 2.0nH spiral compared with PEEC model results.	70
4.3 $Q_{11}(\omega)$ of the 2.0nH spiral compared with PEEC model results.	71
4.4 Series inductance of the 2.0nH spiral compared with PEEC model results.	72

LIST OF FIGURES (Continued)

<u>Figure</u>	<u>Page</u>
4.5 Series resistance of the 2.0nH spiral compared with PEEC model results.	72
4.6 Shunt capacitance at port one of 2.0nH spiral compared PEEC model results.	73
4.7 Shunt conductance at port one of 2.0nH spiral compared with PEEC model results.	73
4.8 $L_{11}(\omega)$ and $R_{11}(\omega)$ for the 2.0nH spiral compared with transformer-loop compact model results.	74
4.9 $Q_{11}(\omega)$ for the 2.0nH spiral compared with transformer-loop compact model results.	75
4.10 Series inductance and resistance of the 2.0nH spiral compared with the extracted single- and double-loop series circuits.	76
4.11 Shunt capacitance and conductance of the 2.0nH spiral compared with the extracted C-GC and C-GC-GC shunt circuits.	76
4.12 Layout of the 4.3 nH octagonal spiral inductor on low-loss substrate.	78
4.13 $L_{11}(\omega)$ and $R_{11}(\omega)$ for the 4.3nH spiral compared with PEEC model results.	79
4.14 $Q_{11}(\omega)$ of the 4.3nH spiral compared with PEEC model results.	80
4.15 Frequency dependent partial inductance and resistance of coupled segments on silicon.	81
4.16 Shunt capacitance at port one of 4.3nH spiral compared PEEC model results.	81
4.17 Shunt conductance at port one of 4.3nH spiral compared with PEEC model results.	82

LIST OF TABLES

<u>Table</u>		<u>Page</u>
4.1	Component values for the single- and double-loop series circuits for the transformer-loop compact model of the 2.0nH spiral.	77
4.2	Component values for the C-GC and C-GC-GC shunt circuits for the transformer-loop compact model of the 2.0nH spiral.	77

LIST OF APPENDIX FIGURES

<u>Figure</u>	<u>Page</u>
B.1 Layout of 2.5 turn rectangular spiral inductor.	94
B.2 PEEC approximation of 2.5 turn rectangular spiral inductor.	96
B.3 Linear equations describing all end-points of the PEEC approximation for the rectangular spiral inductor.	97
B.4 Filamental PEEC approximation of the 2.5 turn rectangular spiral inductor.	98
B.5 Layout of 2.5 turn octagonal spiral inductor.	99
B.6 PEEC approximation of 2.5 turn octagonal spiral inductor.	100
B.7 Linear equations describing all end-points of the PEEC approximation for the octagonal spiral inductor.	101
B.8 Filamental PEEC approximation of the 2.5 turn octagonal spiral inductor.	102
C.1 Parallel rectangular bars.	104
C.2 Parallel filaments.	105
C.3 Unequal angled filaments meeting at a point.	106
C.4 Unequal angled filaments in the same plane, not touching.	107
C.5 Unequal angled filaments in any position, not touching.	109

Modelling of On-Chip Spiral Inductors for Silicon RFICs

1. INTRODUCTION

1.1. Background and Motivation

Since its invention in 1958 [1], the integrated circuit (IC) has influenced nearly every part of modern life. First, and so far most importantly, the IC enabled the development of the modern microprocessor. This early focus on digital applications began a continuing trend of higher levels of integration, reduced power consumption, and higher clock speeds. More recently, mixed-signal ICs have become increasingly popular, with an emphasis on multi-gigahertz frequencies and increased levels of integration, i.e. “System on a Chip” (SoC). To reduce the cost of creating such ICs, manufacturers have focused their efforts on silicon processes with well-developed CMOS devices. To enable the design of analog circuits for the 1 to 10 GHz region, SiGe “BiCMOS” processes have been developed that combine low-cost CMOS technology with high performance heterojunction bipolar transistors (HBTs) having transition frequencies (F_t) in the 50 GHz region [2].

In spite of these advances, passive devices remain a major bottle-neck for high performance mixed-signal radio-frequency ICs (RFICs). A particularly frustrating example is the planar spiral inductor originally developed for use on printed circuit boards [3]. As with all other passive components, the inductor was destined to make its way onto silicon, although its path was perhaps the roughest. In 1966,

researchers at Motorola were among the first to publish results for a spiral inductor fabricated on a silicon substrate [4]. Their 20-turn spiral measured 0.33 inches in diameter and was deposited on silicon having a resistivity of 50 Ω -cm. After reporting an inductance of 2.3 μ H and peak quality factor (Q) of approximately 5, they summarized their findings by stating that "... it seems likely that any necessary inductance will be placed external to the monolithic circuit." Eleven years later, in 1977, researchers Temes and Lapatra used a more theoretical argument to show that on-chip inductors were impractical [5]. Essentially, they showed that if all linear dimensions of an inductor are scaled by a factor x , where $0 < x < 1$, the quality factor of an inductor scales in proportion to x^2 . They also listed five convincing drawbacks to using inductors in microelectronic applications, including noise coupling, size, etc. Research in spiral inductors continued, however, and by the late 1980's many researchers had demonstrated the usefulness of spiral inductors on low-loss substrates such as GaAs [6]. The final step of demonstrating a successful implementation of spiral inductors on a silicon IC came in 1990 and can be attributed to Meyer and Nguyen [7]. These researchers showed that a passive five-pole maximally-flat low-pass filter designed with a cutoff frequency of 880 MHz could be successfully implemented in a commercial silicon process using two rectangular spiral inductors. They were able to obtain very good results in spite of the fact that the inductors had Q's of less than 10. Meyer and Nguyen attributed their success, in part, to advances in lithographic techniques which allowed metal widths and pitches in the low micron range, thereby increasing the inductance per unit area. In all, it took nearly 25 years of engineering before spiral inductors were successfully used in a silicon integrated circuit.

As the wireless revolution forces more designs to operate in the 1 to 10 GHz region, the on-chip spiral inductor has emerged as indispensable for numerous applications. At the time of this writing, spiral inductors are commonly used in silicon RFICs and enable high performance circuits such as Low Noise Amplifiers (LNAs) [8], Voltage-Controlled Oscillators (VCOs) [9], mixers, power amplifiers [10], and filters [11]. It is easy to assume, in light of their present popularity, that spiral inductors on silicon substrates are simple to model. In fact, spiral inductors on silicon suffer from several non-ideal loss effects that must be taken into account to create a successful design. The next section discusses several of these loss effects qualitatively as well as ideas researchers have proposed to reduce their impact on the performance of spiral inductors.

1.2. Loss Mechanisms of Spiral Inductors on Silicon Substrates

The major loss mechanisms present in spiral inductors on silicon substrates can, for the most part, be divided into two categories: electric field losses and magnetic field losses. A third category involving radiation losses can be included, but for the purposes of this research these losses are assumed to be negligible. This assumption is discussed in more detail in Chapter 2. The electric and magnetic fields around a spiral inductor are caused by the time-varying surface-charges and conductor currents that are impressed on and inside the inductor metallization. These fields can penetrate deep into the silicon substrate below a spiral inductor. Because of the resistive nature of the substrate, the time-varying fields result in frequency-dependent ohmic losses. The interaction between the spiral inductor and

the lossy substrate is at the root of many of the difficulties in modelling spiral inductors on silicon.

1.2.1. Electric Field Losses

The electric field created by charges on the surfaces of the spiral inductor not only couples the spiral inductor to the substrate but also creates electric coupling among the various segments of the inductor. The interaction between the time-varying electric field and the substrate is illustrated in Figure 1.1. At low frequencies the electric field causes shunt displacement currents to flow through the oxide and mostly conduction currents in the substrate. As frequency increases, the currents in the substrate become increasingly dominated by displacement currents. Differences in electric potential between various parts of the spiral metallization can also generate frequency dependent losses. Figure 1.2 illustrates the “nearest-neighbor” coupling which leads to lateral displacement currents. The lateral electric field interaction can also generate ohmic losses in the substrate depending on the distance of the spiral inductor from the surface of the substrate.

1.2.2. Magnetic Field Losses

A time-varying magnetic field is created by the the impressed currents flowing in the metallization of the spiral inductor. This magnetic field not only links each of the segments, but also links the spiral inductor to the substrate.

The proximity and conductor- skin effects can be attributed to the more localized magnetic fields between the spiral segments. Figure 1.3 shows some of the magnetic field lines that are created by one segment and pierce another. There

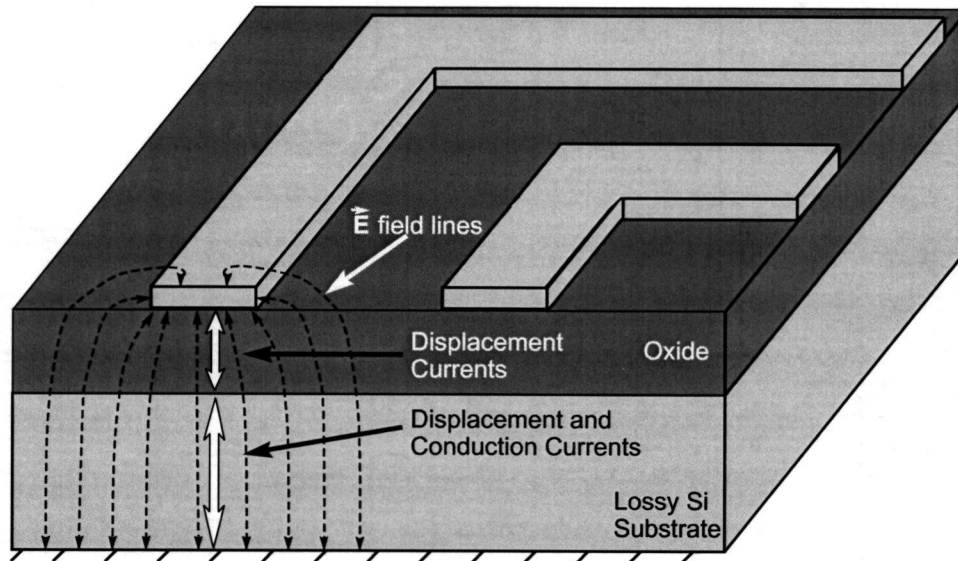


FIGURE 1.1. Shunt electric field in an on-chip spiral inductor.

are also local internal magnetic fields inside each of the segments. These self and mutual magnetic fields lead to the conductor-skin and proximity effects, respectively, which are similar in nature. Both of these effects are geometry-, frequency-, and conductivity-dependent and lead to a non-uniform current distribution inside the spiral segments.

Larger field lines also exist around the spiral inductor which can couple the spiral metallization to the lossy substrate, as illustrated in Figure 1.4. Only a portion of the magnetic field has been shown to simplify the figure. In reality, the magnetic field lines would encircle the entire spiral inductor. The time-varying nature of the magnetic field generates currents in the substrate (also known as eddy-currents) similar to the way power transformers generate eddy-currents in an iron core. The eddy-currents flowing in the resistive substrate generate ohmic losses which are

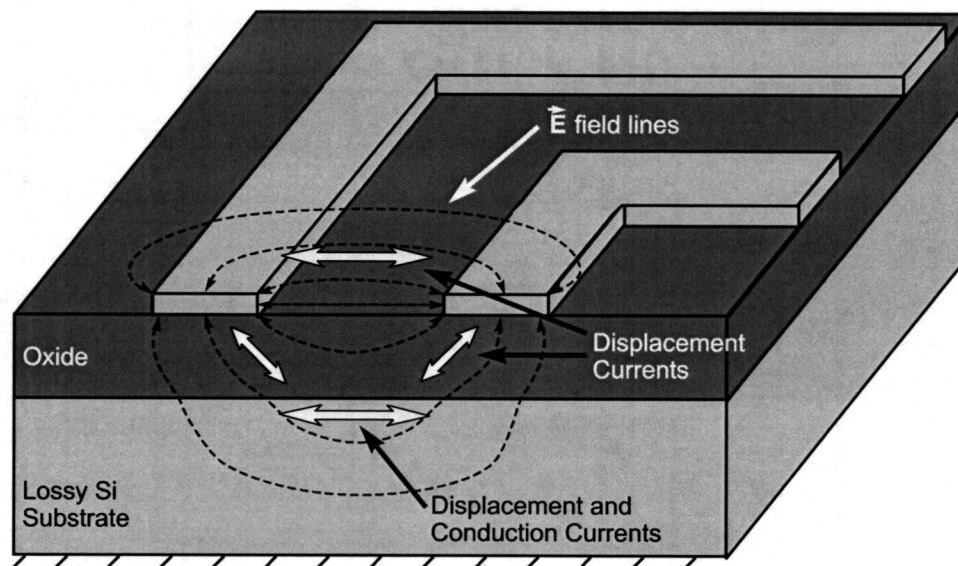


FIGURE 1.2. Lateral electric field interaction in an on-chip spiral inductor.

reflected back into the spiral inductor as an increased series resistance. The series inductance is also decreased by the opposing magnetic field generated by the eddy-currents. As frequency increases, the skin-depth in the bulk silicon decreases and the eddy-currents move closer to the spiral inductor. This combination of increased series resistance and decreased series inductance caused by the frequency dependent eddy-currents can significantly lower the Q of spiral inductors on low resistivity substrates.

The combination of magnetic- and electric-field losses often results in spiral inductors with Q 's less than ten, as opposed to off-chip inductors with Q 's in the 100's. In light of this, circuit designers have often struggled to create circuits which do not rely on the Q of on-chip inductors. Increasing demand for improved inductor performance has led to several interesting modifications to the basic spiral inductor.

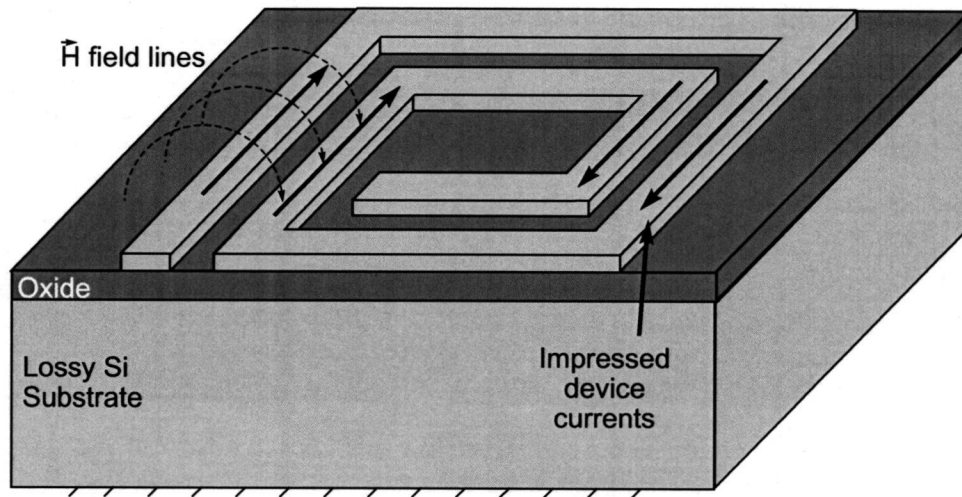


FIGURE 1.3. Magnetic field interactions related to the proximity and skin effects in an on-chip spiral inductor.

1.3. Spiral Inductor Improvements

Researchers have continuously sought to improve the performance of spiral inductors on silicon. One of the most common methods for increasing the Q of a spiral is to reduce the series resistance. This is typically done by using several metal layers connected by vias in a shunt fashion [12]. Another common practice is to create “hollow” spirals where the inner-most turns are not included, as these turns have a large DC resistance and contribute little to the inductance [13]. It is also becoming common for designers to use a process option such as a thick, possibly copper, “inductor metal” layer as the top metal layer [14]. The use of copper reduces the impact of the conductor skin effect as well as lowers the DC resistance. Usually, the inductor-metal is several microns thick and is separated from the next metal

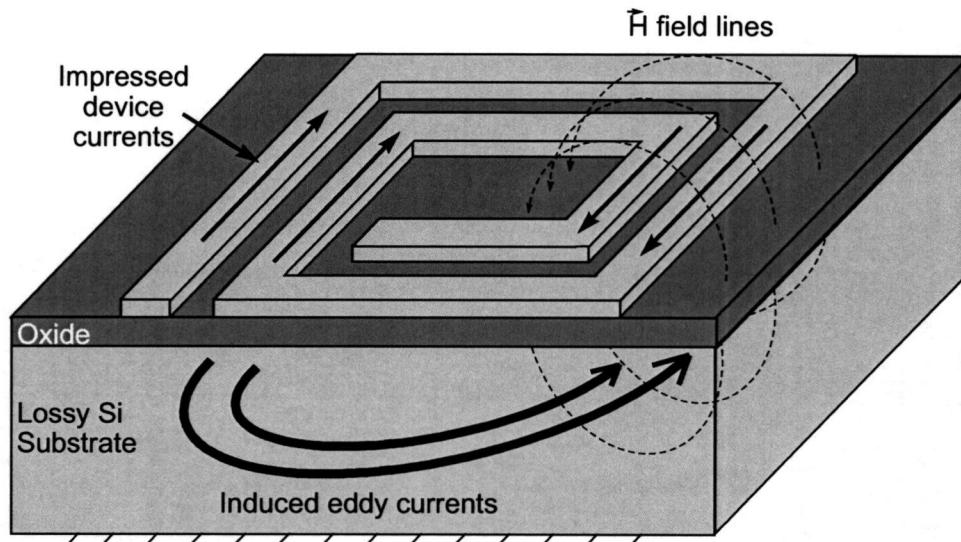


FIGURE 1.4. Magnetic field coupling to the lossy substrate.

layer with a thick dielectric layer in an attempt to reduce the interaction with the substrate.

Several other improvements have been developed which can increase the inductance-to-area ratio, an example being the differential spiral inductor which can also have an improved Q factor [15]. Another method involves fabricating spiral inductors on several different metal layers and then connecting them in series-solenoidal fashion [16].

Patterned-ground shields have also been explored as a means to reduce the shunt losses generated in the substrate [17], [18]. These shields are usually created at a conductive polysilicon layer to maximize their distance from the spiral inductor. Unfortunately, this method involves a trade-off between higher Q and lower self-resonant frequency. This is due to the increased capacitance between the spi-

ral inductor and the grounded shield. Approaching the problem from a completely different angle, several researchers have proposed to simply remove the offending silicon from below a spiral inductor [19]- [21]. Using special etching techniques, a spiral can be suspended, virtually in free-space, above the ground-plane. Unfortunately, the area surrounding the spiral inductor is rendered less-usable for active devices because of the diminished substrate.

Perhaps the most exotic improvement to date is the development of vertical planar spiral inductors using Plastic Deformation Magnetic Assembly (PDMA) [22], [23]. This method reduces interactions between the substrate and the spiral inductor by aligning the spiral inductor perpendicular to the surface of the substrate.

While all of these methods provide some improvement to the spiral inductors performance, they are incremental at best. Until a new, much improved, generation of inductors is developed for silicon ICs, designers must be able to accurately predict how a proposed spiral inductor will be affected by electric- and magnetic-field losses before they can use it in a design. In general, modern spiral inductors must be analyzed using rigorous EM-based simulations. There are currently several options available to the RF designer when choosing a simulation tool.

1.4. Conventional Characterization and Modelling Techniques

Currently, several different methods exist for characterizing spiral inductors. Commercial “2.5-D” simulators such as Agilent’s Momentum [24] and Sonnet Software’s Sonnet Suites [25] are both based on the Method of Moments (MoM) and can provide accurate results for a range of planar spiral inductor structures. Complex multi-layer inductors may require full-wave, 3-D simulators such as Ansoft’s HFSS

[26] which can provide very accurate results using the Finite Element (FE) method at the cost of long simulation times. An alternative analysis method known as the Partial Element Equivalent Circuit (PEEC) method has recently been gaining in popularity. Originally applied to micro-electronics problems by A.E. Ruehli in 1974 [27], PEEC provides a methodology for replacing complicated 3-D electromagnetic problems with ideal equivalent circuits. It has since been used in both commercial and public-domain simulation tools. Examples of current PEEC-based software for analyzing spiral inductors include Cadence Design Systems' Passive Component Modeler (part of the Spectre-RF simulator) [28], National Technical University of Athens's SISP [29], and University of California, Berkeley's ASITIC [30]. The major drawback of the traditional PEEC approach is the need to subdivide all conductive portions of a structure, including the substrate for a spiral inductor problem. The research presented in this thesis concentrates, in part, on an alternative PEEC formulation where the effects of the lossy substrate are included using a complex image approach coupled with closed-form equations for partial inductance.

While the programs and techniques already mentioned are useful for finding the frequency domain behavior of a spiral inductor, there is also a need for compact equivalent-circuit models which circuit designers can use in time- and frequency-domain circuit simulations. These equivalent-circuit models typically consist of a minimum number of ideal circuit elements. One of the most popular compact models for spiral inductors is the "nine-element" model [31], [32]. Unfortunately, this model neglects several major magnetic-field loss effects present in spiral inductors on lossy silicon substrates. This restricts the use of the nine-element model to narrow-band applications. A major portion of the research presented in this thesis concentrates on a new, wide-band, compact equivalent-circuit model suitable for spiral inductors on

high-loss substrates, as well as a fast extraction technique to obtain the component values of the model from S-parameter data.

1.5. Organization of the Study

This thesis presents a complete modelling methodology for spiral inductors on lossy silicon substrates. Emphasis is given to rectangular and octagonal spiral inductors as these are currently the most popular geometries on common CMOS and BiCMOS process. The research is divided into two major parts, scalable modelling and compact, equivalent circuit modelling of spiral inductors.

Chapter 2 describes a scalable, predictive model for spiral inductors on lossy silicon substrates. The chapter begins by developing the basic PEEC model for a simple rectangular spiral inductor. The PEEC analysis allows the complex electromagnetic problem to be replaced by an equivalent distributed circuit model. The basic model is then extended to include the skin and proximity effects through discretization of the spiral segments. Magnetic field losses in the substrate are efficiently included using a complex image approach coupled with available closed-form equations for partial inductance. Electric field effects are included through a transmission-line approximation based on a fast Spectral Domain Approach (SDA). It is then discussed how the complete equivalent circuit can be solved for the two-port Y-parameters using modified nodal analysis (MNA).

Chapter 3 presents a wide-band, compact equivalent circuit model for spiral inductors on heavily doped substrates. The model is based on the transformer analogy of the coupling between the spiral metallization and the lossy substrate. This “transformer-loop” model consists of only ideal components and is suitable

for time-domain simulations. The new compact model is complemented by a fast extraction methodology based on a least-squares fitting procedure.

Chapter 4 shows results for the scalable model for spiral inductors on high- and low-loss silicon substrates. The new compact model is also extracted from measurements from the spiral inductor on high-loss substrate. A comparison with measurements from the two spiral inductors is shown for both models.

Chapter 5 concludes the study and suggests possible directions for future research.

2. SCALABLE MODELLING

2.1. Introduction

The design of spiral inductors for high-frequency applications can be a difficult task. In many circuits, the success of the design can depend almost entirely on several aspects of the frequency domain behavior of the integrated spiral inductors. The inductors self-resonant frequency, for instance, must occur far enough above the circuit's bandwidth so as to not interfere with the circuits operation. It is also vital in many applications that the one-port Q , Q_{11} , is above a certain level in the frequency range of interest. The total inductance, L_{11} , can vary with frequency and must be within acceptable limits. These characteristics and several others must be verified before a circuit using a spiral inductor is fabricated, as the cost of producing multiple generations can be prohibitive. Unfortunately, the frequency-dependent losses associated with a silicon substrate can make it especially difficult to predict (with any accuracy) a spiral inductors frequency domain behavior. Typically, a time-consuming full-wave simulation is performed to verify the prospective spiral design. If the goal is to optimize as well as verify the layout of the spiral, the time involved is multiplied by the number of design iterations.

For these reasons, a quasi-static characterization technique has been developed, based on the PEEC approach. This method utilizes the relationship between electromagnetic analysis and circuit theory. The PEEC approach has already been used to analyze spiral inductors with varying degrees of success ([29], [30], [33]). What makes this implementation different is its ability to efficiently include the effects of the lossy substrate. In the traditional PEEC approach, the conductive substrate would be sub-divided along with all other conductors, involving much

computation time and leading to a very large equivalent circuit. A simple, efficient alternative is presented which uses complex image theory combined with closed-form equations for partial inductance to eliminate the need to discretize the substrate. This approach is similar to that presented in [34] for analyzing on-chip transmission lines. The major draw-back to this technique is that the resulting equivalent circuit contains frequency dependent components. This implies that the circuit must be assembled and solved at each frequency point of interest if traditional circuit solution techniques are to be used.

To clarify the PEEC approach, Section 2.2 describes the mathematical development of the traditional PEEC model. Section 2.3 builds on this basic model by including the conductor skin and proximity effects. Sub-sections 2.3.1 and 2.3.3 describe methods for efficiently including substrate effects. Finally, Section 2.4 describes how Modified Nodal Analysis (MNA) can be used to solve the enhanced PEEC model at each frequency point.

2.2. Simplified PEEC Model of Rectangular Spiral Inductor

In order to make this development more meaningful to the specific problem of modeling spiral inductors, the PEEC model for a single turn rectangular spiral inductor is described. It can be assumed, for the time being, that this spiral inductor is suspended in a lossless dielectric half-space above a perfectly conducting ground plane. This simplified model is useful for showing the relationship between Maxwell's equations and basic circuit theory. In the following, a formulation similar to the Method of Moments will be used to transform the differential equation (2.1) into a summation of coupled circuit equations which describe the partial element equivalent

circuit for the structure shown in Figure 2.1. Ports have been placed according to

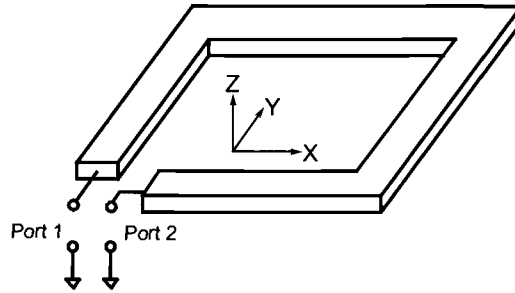


FIGURE 2.1. Single-turn rectangular spiral inductor in free-space.

where the structure would most likely be excited. The sources of the electric field in the structure can be summed as

$$\mathbf{E}_o(\mathbf{r}, t) = \nabla\Phi(\mathbf{r}, t) + \frac{\partial\mathbf{A}(\mathbf{r}, t)}{\partial t} + \frac{\mathbf{J}(\mathbf{r}, t)}{\sigma} \quad (2.1)$$

where \mathbf{E}_o is the applied electric field and the terms on the RHS of (2.1) are due to charges and currents flowing in the conductors. This relationship can be developed from Maxwell's equations and is derived in Appendix A. The first term on the RHS, $\nabla\Phi$, is due to free charges on the surfaces of the conductor system, the second term, $\frac{\partial\mathbf{A}}{\partial t}$, is related to the magnetic field due to time-varying currents, while the third term, $\frac{\mathbf{J}}{\sigma}$, describes the ohmic relationship between the electric field and current. The vector magnetic potential \mathbf{A} and the electric potential, Φ , can be related to the currents and charges of the structure using the following quasistatic relationships

$$\mathbf{A}(\mathbf{r}, t) = \int_{v'} G_A(\mathbf{r}, \mathbf{r}') \mathbf{J}(\mathbf{r}', t) dv' \quad (2.2)$$

$$\Phi(\mathbf{r}, t) = \int_{v'} G_{\Phi}(\mathbf{r}, \mathbf{r}') \rho(\mathbf{r}', t) dv' \quad (2.3)$$

where G_A and G_{Φ} are appropriate Green's functions. In both of these formulas the retardation effects have been neglected. This assumption effectively removes any radiation losses from our model.

It is important to make a distinction between the lack of radiation losses in the model and the possibility of distributed effects, i.e. transmission line effects. It is well known that typical spiral inductors are constructed from segments of on-chip microstrip transmission lines. In light of this, it can be expected that at a high enough frequency, a spiral inductor would exhibit transmission-line behavior such as standing wave phenomena and a noticeable time delay between ports. The PEEC approach, as described in [27], inherently includes these effects by allowing the voltage and current to vary spatially in all three dimensions as well as in time.

The amount of spatial variation allowed in the model (i.e. the “mesh size”) directly affects the complexity of the resulting equivalent circuit as well as the accuracy of the solution. At one extreme, the equivalent circuit will be very compact but inaccurate, at the other, more accurate extreme, the circuit becomes prohibitively large. Because of this tradeoff, it is important to understand which parts of a spiral inductor contain non-negligible spatial variations in current and voltage over the frequency range of interest. For now, the variation over the cross-section of the spiral inductor is ignored, this will be addressed in Section 2.3. Concentrating on the variation along the length of the spiral inductor, a convenient choice is to assume that the individual straight segments can be modelled as having negligible variation along their lengths. This assumption can be considered quantitatively by examining the ratio of the length of the longest spiral segment, R , and the wavelength, λ , on a similar microstrip transmission line. If this ratio is much less than unity over the

frequency range of interest then the spatial variation can be considered negligible, [35]. In this development the transmission line is considered to be suspended in free-space above a perfect ground plane similar to the single-turn spiral inductor in Figure 2.1. The resulting wavelength is given by

$$\lambda = \frac{1}{f\sqrt{\mu_0\epsilon_0}} \quad (2.4)$$

It is also assumed that the longest segment would be 300 microns, a very conservative estimate for modern spiral inductors. The result can be seen in Figure 2.2, it is obvious that the spatial variation along the length of each segment of a typical spiral inductor can be safely ignored until well above 10GHz.

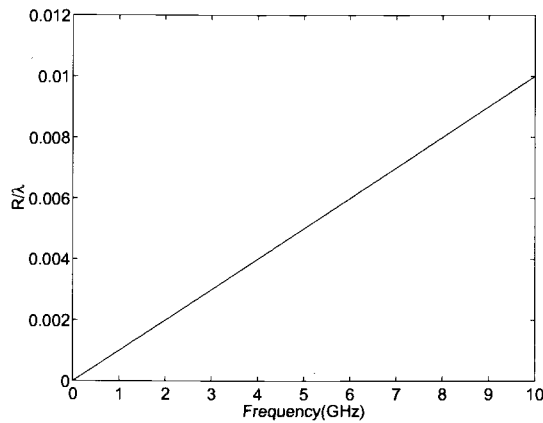


FIGURE 2.2. Ratio of segment length to free-space wavelength for microstrip.

Now that a mesh size has been chosen, the unknown currents in the spiral can be discretized accordingly.

$$\mathbf{J}(\mathbf{r}, t) = \sum_{i=1}^4 p_i I_i(t) \hat{l}_i \quad (2.5)$$

Equation 2.5 involves a summation over the four segments that make up the single-turn inductor structure. The function p_i is defined as

$$p_i = \begin{cases} \frac{1}{a_i} & \text{inside segment } i \\ 0 & \text{otherwise} \end{cases} \quad (2.6)$$

where a_i is the crosssectional area of segment i . The direction of each of the terms in the summation is defined by the unit vectors l_i with orientations that are described in Figure 2.3. These unit vectors describe the assumed direction for positive current in

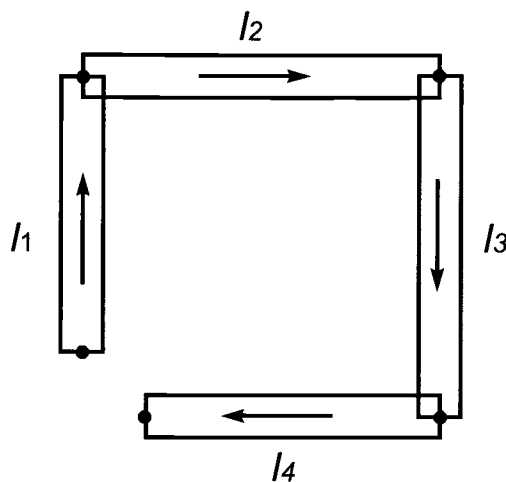


FIGURE 2.3. Current directions in inductor structure.

each of the segments. The time varying magnitude of the current in each segment is described by $I_i(t)$. It should be pointed out that the ends of the segments in Figure 2.3 have been extended to meet at a half-way point in the 90 degree angle, as opposed to discretizing the corners. This simplification is made to reduce the complexity of the equivalent circuit. Circuit nodes are conveniently placed at the

end points of all of the segments. Finally, it is important to notice that (2.5) assumes that the segment currents are uniform over the crosssection of each segment. This simplification effectively removes the conductor skin and proximity effects which are addressed in Section 2.3.

Next, the unknown charge distribution is discretized

$$\rho(\mathbf{r}, t) = \sum_{m=1}^5 u_m q_m(t) \quad (2.7)$$

where u_m is defined as

$$u_m = \begin{cases} 1 & \text{on charge surface } m \\ 0 & \text{otherwise} \end{cases} \quad (2.8)$$

and $q_m(t)$ is the time-varying surface charge density on charge cell m . Figure 2.4 shows an appropriate choice of surface charge cell divisions. Because the potential

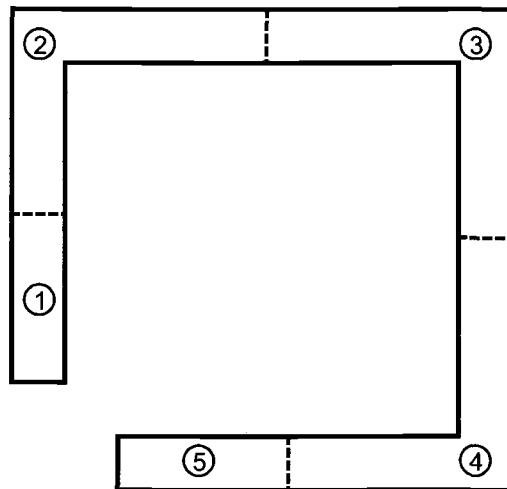


FIGURE 2.4. Example charge cell divisions.

is assumed to be constant over each of the surface charge cells it is important that they only contact one node each.

Next, (2.5) and (2.7) can be substituted into (2.2) and (2.3)

$$\begin{aligned}\mathbf{A}(\mathbf{r}, t) &= \int_{v'} G_A(\mathbf{r}, \mathbf{r}') \left(\sum_{i=1}^4 p_i I_i(t) \hat{l}_i \right) dv' \\ &= \sum_{i=1}^4 \left[\frac{I_i(t) \hat{l}_i}{a_i} \cdot \left(\int_{v'_i} G_A(\mathbf{r}, \mathbf{r}') dv'_i \right) \right]\end{aligned}\quad (2.9)$$

and,

$$\begin{aligned}\Phi(\mathbf{r}, t) &= \int_{v'} G_\Phi(\mathbf{r}, \mathbf{r}') \left(\sum_{m=1}^5 u_m q_m(t) \right) dv' \\ &= \sum_{m=1}^5 \left[q_m(t) \left(\int_{s'_m} G_\Phi(\mathbf{r}, \mathbf{r}') ds'_m \right) \right]\end{aligned}\quad (2.10)$$

By combining (2.1), (2.5), (2.9), and (2.10) the following result is obtained

$$\begin{aligned}\mathbf{E}_o(\mathbf{r}, t) &= \frac{\sum_{i=1}^4 p_i I_i(t) \hat{l}_i}{\sigma} \\ &+ \sum_{i=1}^4 \left[\frac{\partial I_i(t)}{\partial t} \cdot \frac{\hat{l}_i}{a_i} \cdot \left(\int_{v'_i} G_A(\mathbf{r}, \mathbf{r}') dv'_i \right) \right] \\ &+ \sum_{m=1}^5 \left[q_m(t) \nabla \left(\int_{s'_m} G_\Phi(\mathbf{r}, \mathbf{r}') ds'_m \right) \right]\end{aligned}\quad (2.11)$$

Next, to generate a set of coupled equations that describe the circuit, the inner product of both sides of (2.11) is taken with an appropriate testing function:

$$\begin{aligned}\langle \mathbf{E}_o(\mathbf{r}, t), p_j \hat{l}_j \rangle &= \left\langle \frac{\sum_{i=1}^4 p_i I_i(t) \hat{l}_i}{\sigma}, p_j \hat{l}_j \right\rangle \\ &+ \left\langle \sum_{i=1}^4 \left[\frac{\partial I_i(t)}{\partial t} \cdot \frac{\hat{l}_i}{a_i} \cdot \left(\int_{v'_i} G_A(\mathbf{r}, \mathbf{r}') dv'_i \right) \right], p_j \hat{l}_j \right\rangle\end{aligned}$$

$$+ \left\langle \sum_{m=1}^5 \left[q_m(t) \nabla \left(\int_{s'_m} G_{\Phi}(\mathbf{r}, \mathbf{r}') ds'_m \right) \right], p_j \hat{l}_j \right\rangle \quad (2.12)$$

For this purpose, the inner product can be defined as

$$\langle \hat{a}, \hat{b} \rangle = \int_v (\hat{a} \cdot \hat{b}) dv \quad (2.13)$$

where the volume integral is over the entire problem space. The testing functions have been chosen to be the same as the basis functions used in (2.5). This approach is similar to the Galerkin Method, [36], but the resulting equations will differ because of the basis functions used for the charge distribution.

Each of the terms in (2.12), with a sufficient amount of algebra, can be interpreted as various ideal circuit elements such as resistors, self and mutual inductances, and capacitances. Historically, these components have been referred to as partial elements (i.e. partial resistances, partial inductances, etc., [27], [37]). The following sections describe how each term is specifically related to an appropriate partial element. The resulting set of coupled circuit equations are the same as those found using Kirchoff's circuital laws.

2.2.1. Branch Voltages

The LHS of (2.12) can be related to the applied electric field as follows

$$\begin{aligned} \langle \mathbf{E}_o(\mathbf{r}, t), p_j \hat{l}_j \rangle &= \int_{v_j} (\mathbf{E}_o(\mathbf{r}, t) \cdot p_j \hat{l}_j) dv_j \\ &= \int_{a_j} \int_{l_j} \left(\frac{\mathbf{E}_o(\mathbf{r}, t)}{a_j} \cdot d\hat{l} \right) da_j \\ &= \frac{1}{a_j} \int_{a_j} \left(\int_{l_j} \mathbf{E}_o(\mathbf{r}, t) \cdot d\hat{l} \right) da_j \end{aligned}$$

$$\begin{aligned}
&= \frac{1}{a_j} \int_{a_j} [\Phi(\mathbf{r}^+, t) - \Phi(\mathbf{r}^-, t)] da_j \\
&= \tilde{\Phi}_j^+(t) - \tilde{\Phi}_j^-(t)
\end{aligned} \tag{2.14}$$

where $\Phi(\mathbf{r}^+, t)$ and $\Phi(\mathbf{r}^-, t)$ are the potentials at the positive and negative ends of branch j . These potentials are functions of the positions at the end-faces until the final step where the average over the end-faces is taken. The final result of (2.14) is the average voltage difference between nodes j and $j + 1$, or the voltage across branch j .

2.2.2. Partial Resistances

The first term on the RHS of (2.12) relates the unknown current to a portion of the induced electric field using the ohmic relationship. The inner product can be evaluated as

$$\begin{aligned}
\left\langle \frac{\sum_{i=1}^4 p_i I_i(t) \hat{l}_i}{\sigma}, p_j \hat{l}_j \right\rangle &= \int_{v_j} \frac{I_j(t)}{\sigma a_j^2} dv_j \\
&= I_j(t) \cdot \frac{l_j}{\sigma a_j} \\
&= I_j(t) \cdot R_j
\end{aligned} \tag{2.15}$$

where R_j can be interpreted as the partial resistance of branch j and $I_j(t)$ is the time-varying current in branch j .

2.2.3. Partial Self and Mutual Inductances

The second term on the RHS of (2.12) can be equated to the inductive coupling within the conductor structure as follows

$$\begin{aligned}
& \left\langle \sum_{i=1}^4 \left[\frac{\partial I_i(t)}{\partial t} \cdot \frac{\hat{l}_i}{a_i} \cdot \left(\int_{v'_i} G_A(\mathbf{r}, \mathbf{r}') dv'_i \right) \right], p_j \hat{l}_j \right\rangle \\
&= \int_{v_j} \sum_{i=1}^4 \left[\frac{\partial I_i(t)}{\partial t} \cdot \frac{\langle \hat{l}_i, \hat{l}_j \rangle}{a_i a_j} \cdot \left(\int_{v'_i} G_A(\mathbf{r}, \mathbf{r}') dv'_i \right) \right] dv_j \\
&= \sum_{i=1}^4 \left[\frac{\langle \hat{l}_i, \hat{l}_j \rangle}{a_i a_j} \cdot \int_{v_j} \int_{v'_i} G_A(\mathbf{r}, \mathbf{r}') dv'_i dv_j \right] \cdot \frac{\partial I_i(t)}{\partial t} \\
&= \sum_{i=1}^4 L_{ji} \frac{\partial I_i(t)}{\partial t} \tag{2.16}
\end{aligned}$$

The term inside square brackets is recognized as partial inductance. It is important to note that the dot product of the unit vectors, \hat{l}_i and \hat{l}_j , determines the sign of the mutual partial inductances and results in zero mutual inductance for anti-parallel segments. For practical implementations, closed form equations for partial inductance can be found in [38] and [39].

2.2.4. Partial Capacitances

Finally, the third term on the RHS of (2.12) can be interpreted as a relationship between charge and the potential of various parts of the conductor structure. In general, the charge-potential relationship in a multi-conductor system can be described using coefficients of potential. For an N conductor system the following matrix equation can be written

$$\begin{bmatrix} \Phi_1 \\ \Phi_2 \\ \vdots \\ \Phi_N \end{bmatrix} = \begin{bmatrix} p_{11} & p_{12} & \cdots & p_{1N} \\ p_{21} & p_{22} & \cdots & p_{2N} \\ \vdots & & & \\ p_{N1} & p_{N2} & \cdots & p_{NN} \end{bmatrix} \begin{bmatrix} Q_1 \\ Q_2 \\ \vdots \\ Q_N \end{bmatrix} \tag{2.17}$$

where Φ_N is the potential of conductor N with respect to ground, Q_N is the charge on conductor N , and p_{ij} are the coefficients of potential. These coefficients are

constants that depend on the shapes of the conductors as well as the surrounding media. In general,

$$p_{ij} = \frac{1}{a_j} \int_{s_j} G_{\Phi}(\mathbf{r}_i, \mathbf{r}') ds' \quad (2.18)$$

where $G_{\Phi}(\mathbf{r}_i, \mathbf{r}')$ is the Green's function appropriate to the problem space. The term r_i refers to the fact that the resulting function must be evaluated in some way at conductor i , examples are to average over conductor i (Galerkin's method), or to simply take the value at a single point (Collocation method). These coefficients of potential can be directly related to partial capacitances, [35]. The resulting partial capacitances can be represented by ideal capacitors that are connected amongst the nodes of the equivalent circuit. In light of this relationship, the goal of the following derivation is to relate the charges and potentials of the conductor system in terms of the coefficients of potential, with the understanding that the partial capacitances follow directly from them. Specifically, it is desired to show the following relationship:

$$\langle \nabla \Phi, p_j \hat{l}_j \rangle = \sum_{m=1}^5 (p_{jm}^+ - p_{jm}^-) Q_m(t) \quad (2.19)$$

where the L.H.S. of (2.19) is a simplified version of the third term on the RHS of (2.12) and p_{jm}^+ and p_{jm}^- are the coefficients of potential between charge cell m and the positive and negative ends of segment j respectively. With (2.19) as the goal, the development can proceed from the third term on the RHS of (2.12)

$$\begin{aligned} & \langle \nabla \sum_{m=1}^5 \left[q_m(t) \left(\int_{s'_m} G_{\Phi}(\mathbf{r}, \mathbf{r}') ds'_m \right) \right], p_j \hat{l}_j \rangle \\ &= \int_{v_j} \nabla \sum_{m=1}^5 \left[q_m(t) \int_{s'_m} G_{\Phi}(\mathbf{r}, \mathbf{r}') ds'_m \right] \cdot \frac{\hat{l}_j}{a_j} dv_j \end{aligned} \quad (2.20)$$

To clarify what follows, a substitution is made

$$F_m(\mathbf{r}) = \int_{s'_m} G_\Phi(\mathbf{r}, \mathbf{r}') ds'_m \quad (2.21)$$

which can be substituted into (2.20).

$$\begin{aligned} & \int_{v_j} \nabla \left[\sum_{m=1}^5 q_m(t) F_m(\mathbf{r}) \right] \cdot \frac{\hat{l}_j}{a_j} dv_j \\ &= \frac{1}{a_j} \int_{a_j} \int_{l_j} \nabla \left[\sum_{m=1}^5 q_m(t) F_m(\mathbf{r}) \right] \cdot \hat{dl}_j da_j \end{aligned} \quad (2.22)$$

In general, the gradient function will result in a vector with components in each direction. This result can be simplified by aligning the coordinate system properly in relation to the conductor structure as shown in Figure 2.1. In this case the gradient function combined with the dot product in (2.22) results in

$$\begin{aligned} & \frac{1}{a_j} \int_{a_j} \int_{l_j} \nabla \left[\sum_{m=1}^5 q_m(t) F_m(\mathbf{r}) \right] \cdot \hat{dl}_j da_j \\ &= \frac{1}{a_j} \int_{a_j} \int_{\gamma_j} \frac{\partial}{\partial \gamma_j} \left[\sum_{m=1}^5 q_m(t) F_m(\mathbf{r}) \right] d\gamma_j da_j \\ &= \frac{1}{a_j} \int_{a_j} \sum_{m=1}^5 \left[q_m(t) \int_{\gamma_j} \frac{\partial}{\partial \gamma_j} F_m(\mathbf{r}) d\gamma_j \right] da_j \end{aligned} \quad (2.23)$$

where γ_j can be either the x- or y-coordinate depending on the segment. At this point another simplification must be introduced, in general

$$\int_{\gamma_1}^{\gamma_2} \frac{\partial}{\partial \gamma} F(\gamma, \zeta, \eta) d\gamma = F(\gamma_2, \zeta, \eta) - F(\gamma_1, \zeta, \eta) \quad (2.24)$$

This can be applied to the integrand of (2.23) in the following way

$$\begin{aligned} & \frac{1}{a_j} \int_{a_j} \sum_{m=1}^5 \left[q_m(t) \int_{\gamma_j} \frac{\partial}{\partial \gamma_j} F_m(\mathbf{r}) d\gamma_j \right] da_j \\ &= \sum_{m=1}^5 q_m(t) \frac{1}{a_j} \int_{a_j} [F_m(\mathbf{r}^+) - F_m(\mathbf{r}^-)] da_j \end{aligned}$$

$$\begin{aligned}
&= \sum_{m=1}^5 \frac{Q_m(t)}{a_m} [\tilde{F}_m^+ - \tilde{F}_m^-] \\
&= \sum_{m=1}^5 Q_m(t) [\tilde{p}_{jm}^+ - \tilde{p}_{jm}^-]
\end{aligned} \tag{2.25}$$

where

$$\tilde{p}_{jm}^+ = \frac{1}{a_j} \int_{a_j} \left(\frac{1}{a_m} \int_{s'_m} G_{\Phi}(\mathbf{r}, \mathbf{r}') ds'_m \right) da_j \tag{2.26}$$

in which the parenthetical expression is recognized as being the same as (2.18). The integral over the cross-section of the segment takes place at the end-face and has the effect of averaging the coefficient of potential over the cross-section. The resulting coefficients of potential can be related to partial capacitances using the relationships stated in [35].

To address the practical necessity of calculating partial capacitances on modern silicon processes, researchers have developed many advanced techniques [40], [41], [42]. Section 2.3.3 describes an alternative method that finds partial capacitances using a transmission-line approximation.

2.2.5. Complete Partial Element Equivalent Circuit

To summarize the results of the last several sections the equivalent circuit for the conductor structure in Figure 2.1 is assembled. First, the system of coupled circuit equations that is described by (2.14), (2.15), (2.16), and (2.19) can be stated as

$$\Phi_{n_1} - \Phi_{n_2} = R_1 I_1 + L_{11} \frac{dI_1(t)}{dt} - M_{13} \frac{dI_3(t)}{dt} + \sum_{m=1}^5 (p_{1m}^+ - p_{1m}^-) Q_m(t) \tag{2.27}$$

$$\Phi_{n_2} - \Phi_{n_3} = R_2 I_2 + L_{22} \frac{dI_2(t)}{dt} - M_{24} \frac{dI_4(t)}{dt} + \sum_{m=1}^5 (p_{2m}^+ - p_{2m}^-) Q_m(t) \tag{2.28}$$

$$\Phi_{n_3} - \Phi_{n_4} = R_3 I_3 + L_{33} \frac{dI_3(t)}{dt} - M_{31} \frac{dI_1(t)}{dt} + \sum_{m=1}^5 (p_{3m}^+ - p_{3m}^-) Q_m(t) \quad (2.29)$$

$$\Phi_{n_4} - \Phi_{n_5} = R_4 I_4 + L_{44} \frac{dI_4(t)}{dt} - M_{42} \frac{dI_2(t)}{dt} + \sum_{m=1}^5 (p_{4m}^+ - p_{4m}^-) Q_m(t) \quad (2.30)$$

These equations can be recognized as relating branch voltages to branch currents and charges on the surface of the conductor system. The equivalent circuit described by eqs. (2.27), (2.28), (2.29), and (2.30) is shown in Figure 2.5. To clarify Figure

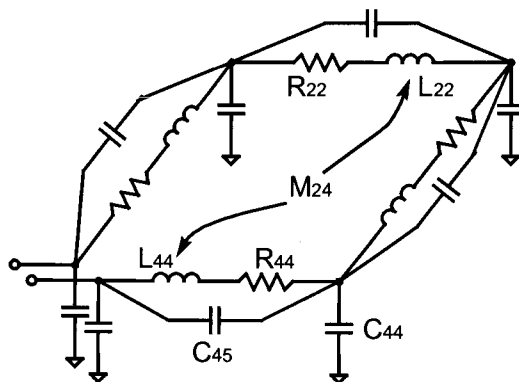


FIGURE 2.5. Equivalent circuit for single turn inductor.

2.5, only the self and nearest-node partial capacitances have been included in the equivalent circuit, and only a portion of the shown components are labeled.

2.3. Extensions to the Basic PEEC Model

It has been shown that by using a quasi-static assumption, ideal equivalent circuits can be found for spiral inductor structures. These equivalent circuits can be

valid into the GHz frequency region depending on the mesh size used in the analysis. For spiral inductors on low-loss substrates, such as GaAs, it is rarely necessary to extend the mesh beyond the spiral metallization. Spiral inductors on lossy silicon, on the other hand, often interact with the substrate material. This means that the substrate must be included as part of the mesh to produce an accurate model. This can increase the number of computations as well as the complexity of the equivalent circuit by several orders of magnitude. The next few sub-sections discuss efficient methods for taking the substrate effects into account with a PEEC model as well as a common technique for including the conductor-skin and proximity effects.

2.3.1. Spiral-Substrate Interaction Through the \vec{H} -Field

Consider the problem of a spiral inductor, at height h , on a lossless substrate with a perfect ground plane as shown in Figure 2.6. The addition of a ground plane

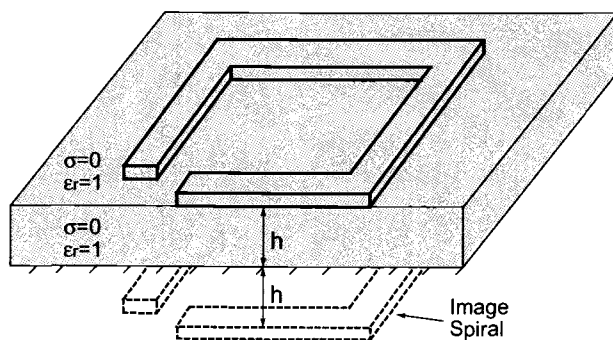


FIGURE 2.6. Single-turn rectangular spiral on lossless substrate.

could be problematic, given that all well-known closed-form equations for partial

inductance are for free-space. Using the method of images, the ground plane is replaced with an image of the inductor, with distance $2h$ between the two inductors. While this doubles the number of partial inductances that must be found, it still allows the use of existing closed-form equations for partial inductance in free-space.

To understand the effect of a ground plane on the spiral inductor, consider two coupled segments, as shown in Figure 2.7. The currents and voltages of the

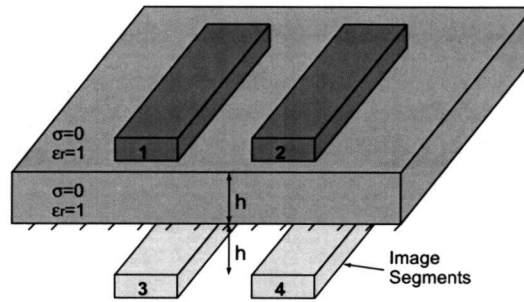


FIGURE 2.7. Coupled segments above perfect ground plane.

inductively coupled segments can be related with the branch equations

$$\begin{bmatrix} v_1 \\ v_2 \end{bmatrix} = \begin{bmatrix} L_{11} - L_{13} & L_{12} - L_{14} \\ L_{21} - L_{41} & L_{22} - L_{24} \end{bmatrix} \begin{bmatrix} \frac{di_1}{dt} \\ \frac{di_2}{dt} \end{bmatrix} = \begin{bmatrix} L_{11,total} & L_{12,total} \\ L_{21,total} & L_{22,total} \end{bmatrix} \begin{bmatrix} \frac{di_1}{dt} \\ \frac{di_2}{dt} \end{bmatrix} \quad (2.31)$$

where v_n and i_n are the branch voltage and current of conductor n , respectively. Each term of (2.31) involves a partial self-inductance and a partial mutual-inductance to the proper image segment. In general, the branch partial inductance matrix for N coupled segments can be summarized as

$$\mathbf{L}_{total}^{(N \times N)} = \mathbf{L}_{free-space} - \mathbf{L}_{image} \quad (2.32)$$

where $\mathbf{L}_{free-space}$ contains partial self- and mutual-inductances for coupled segments in free space and \mathbf{L}_{image} contains only partial mutual inductances between the physical segments and their images. As the distance between the coupled segments and the ground plane is varied, $\mathbf{L}_{free-space}$ will be constant, while the entries of \mathbf{L}_{image} are inversely proportional to the distance. Specifically, for the coupled segment case with reasonable dimensions, Figure 2.8 shows the self and mutual inductances as a function of h . At small values of h , the coupling to the image conductors is large

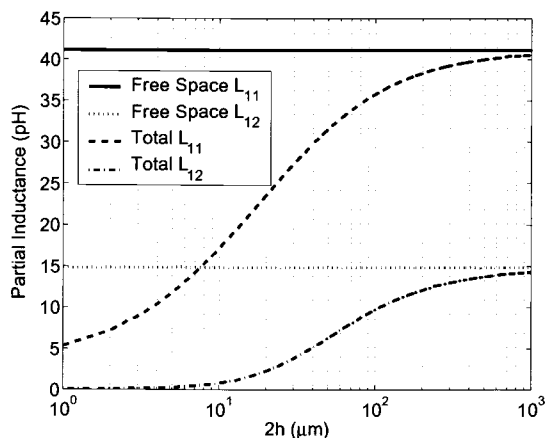


FIGURE 2.8. Partial inductances of coupled segments as the distance to the ground plane is varied.

causing the total inductance to decrease. As the height above the ground plane increases, the total inductance is increasingly dominated by the free-space inductance. This concept of total inductance as a function of height above a ground plane also applies to spiral inductors as they are essentially a set of coupled conductor segments.

For a spiral over a standard two-layer lossy substrate with a perfect ground plane, as in Figure 2.9, the solution would seem to be more complicated. However, as presented in [34], it is possible to approximately replace the lossy two layer substrate with a perfect ground plane at a complex distance, h_{eff} , below the spiral inductor. The complex distance is given by

$$h_{eff} = h_{ox} + \frac{1-j}{2} \delta \tanh \left(\frac{(1+j)h_{si}}{\delta} \right) \quad (2.33)$$

where h_{ox} is the oxide thickness, h_{si} is the bulk thickness, and δ is the skin depth

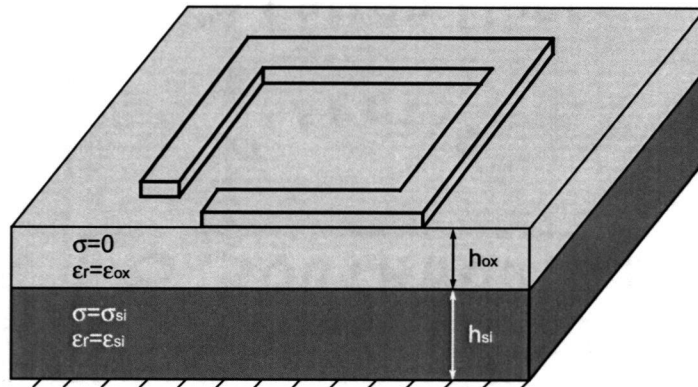


FIGURE 2.9. Standard Si-SiO₂ silicon substrate.

of the bulk silicon. To illustrate the frequency-dependence of the effective height, Figure 2.10 shows the real part of h_{eff} for different substrate conductivities, all with h_{ox} and h_{si} equal to $3\mu m$ and $500\mu m$, respectively. At low frequencies, the eddy currents in the substrate can be ignored, and the effective substrate height is equal to the combined oxide height and thickness of the bulk silicon. In the high frequency limit, the skin depth in the silicon substrate is much smaller than the

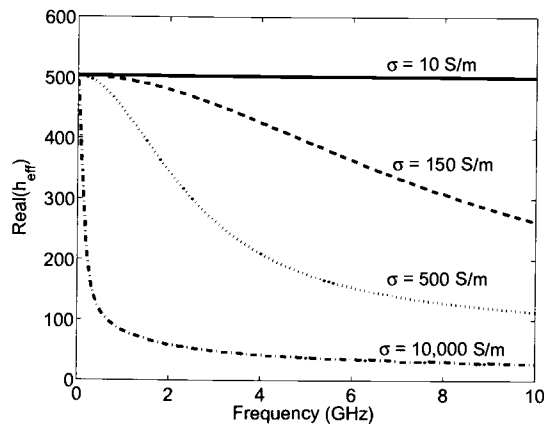


FIGURE 2.10. Real part of h_{eff} as a function of frequency for various substrate resistivities.

substrate thickness. Hence, the effective substrate height is reduced and approaches the limit of the oxide height. Again, the method of images can be used to replace the ground plane with an image spiral inductor, as shown in Figure 2.11. Because of the complex, frequency-dependent distance $2h_{eff}$ between the spiral inductor and its image, it can be expected that \mathbf{L}_{image} , and consequently \mathbf{L}_{total} , will also be complex and frequency dependent. This complex inductance can be interpreted using the following relationships

$$\mathbf{L}(\omega)_{total} = Re(\mathbf{L}(h_{eff})_{total}) \quad (2.34)$$

and

$$\mathbf{R}(\omega)_{total} = -\omega Im(\mathbf{L}(h_{eff})_{total}) + \mathbf{R}_{DC} \quad (2.35)$$

where $\mathbf{L}(\omega)_{total}$ contains the frequency-dependent total partial inductances and $\mathbf{R}(\omega)$ contains partial resistances due to the ohmic losses from eddy-currents in the substrate as well as the DC resistances of the conductors. In general, $\mathbf{R}(\omega)_{total}$ will

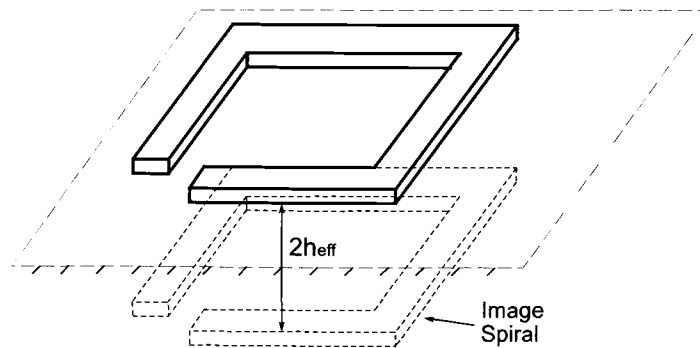


FIGURE 2.11. Complex image spiral replacing the lossy substrate.

contain mutual partial resistances as well as the usual self partial resistances. These mutual resistances arise because of the ohmic losses in the shared return paths for currents in separate segments. To illustrate the frequency dependent inductance and resistances described by (2.34) and (2.35), the case of coupled conductor segments can be re-examined, this time on a lossy substrate with h_{ox} and h_{si} equal to $3\mu m$ and $500\mu m$, respectively. The partial inductances and resistances for $\sigma_{si} = 10^4$ S/m and $\sigma_{si} = 10$ S/m can be seen in Figure 2.12(a) and (b) respectively.

For the $\sigma_{si} = 10$ S/m case, the partial inductances and resistances vary little over the frequency range. However, the $\sigma_{si} = 10^4$ S/m case is greatly affected by the substrate skin effect. At low frequencies, the eddy-currents are negligible and the inductances and resistances are close to their DC values. As frequency increases, the eddy-currents increase in magnitude and are restricted more to the area directly underneath the spiral inductor causing a strong opposing magnetic field. Ohmic losses due to the eddy-currents also increase with frequency as the eddy-currents increase and are restricted to a smaller cross-sectional area. This appears as an increase in the series partial resistance.

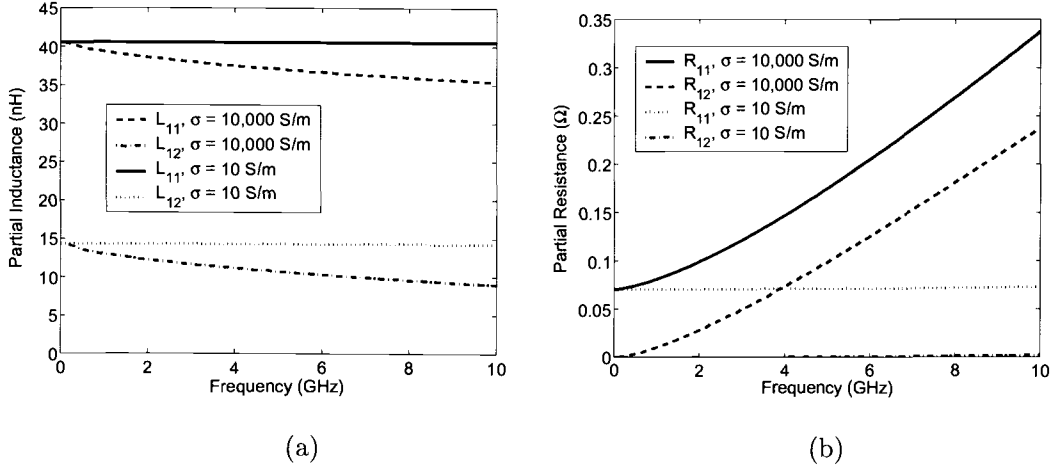


FIGURE 2.12. Frequency dependent partial inductance and resistance of coupled segments on silicon.

To increase the usefulness of the complex image method, it has been extended to substrates with an epitaxial layer (epi-layer). Epi-layer substrates have been developed to reduce the occurrence of “latch-up” in CMOS circuits, a standard epi-layer cross-section is shown in Figure 2.13. The bulk silicon is usually made very lossy, on the order of 10^4 S/m, while the epi-layer itself can be low loss, around 10 S/m. The lossy epi-layer substrate can be replaced with a perfect ground plane at an effective complex distance from the spiral, as is shown in Figure 2.11, where the new h_{eff} is defined as

$$h_{eff_{epi}} = h_{ox} + (1 - j) \left(\frac{\delta_{epi}}{2} \right) \varphi(f) \quad (2.36)$$

where $\varphi(f)$ is defined as

$$\varphi(f) = \frac{\left(\frac{1+j}{\delta_{si}\sigma_{si}} \right) \tanh \left((1+j) \frac{h_{si}}{\delta_{si}} \right) + \left(\frac{1+j}{\delta_{epi}\sigma_{epi}} \right) \tanh \left((1+j) \frac{h_{epi}}{\delta_{epi}} \right)}{\left(\frac{1+j}{\delta_{si}\sigma_{si}} \right) \tanh \left((1+j) \frac{h_{si}}{\delta_{si}} \right) \tanh \left((1+j) \frac{h_{epi}}{\delta_{epi}} \right) + \left(\frac{1+j}{\delta_{epi}\sigma_{epi}} \right)} \quad (2.37)$$

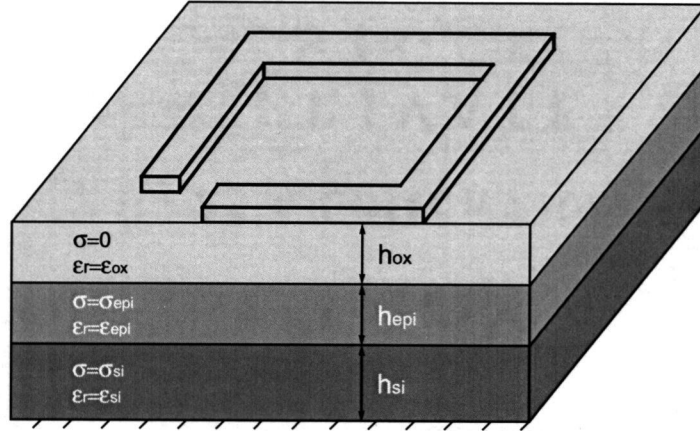


FIGURE 2.13. Standard epi-layer substrate cross-section.

and δ_{epi} and δ_{si} are defined as

$$\delta_{epi} = \frac{1}{\sqrt{\pi f \mu_0 \sigma_{epi}}} \quad (2.38)$$

and

$$\delta_{si} = \frac{1}{\sqrt{\pi f \mu_0 \sigma_{si}}} \quad (2.39)$$

This effective height can be combined with the method of images in exactly the same way as the single-lossy-layer case.

By combining the complex image technique with existing closed-form equations for partial inductance, the effect of eddy-currents in a lossy substrate can be modelled in an efficient manner. Because of the existence of closed-form equations for partial inductance of segments in nearly any relative position, this technique can be applied to spiral inductors of any popular geometry including rectangular, octagonal, hexagonal, etc. The extension of the method to the epi-layer substrate covers most popular types of CMOS and BiCMOS substrate configurations.

2.3.2. Conductor Skin and Proximity Effects

It was assumed in Section 2.2 that the current in each segment of the conductor structure was uniform over the cross-section. This assumption may be valid at low frequencies, depending on the cross-sectional size of the segments as well as the conductivity. However, as frequency increases, the current becomes concentrated at the periphery of the conductor cross-section. This phenomenon is known as the conductor skin-effect. Generally, if the cross-sectional size is much smaller than a skin-depth, where the skin-depth is defined as

$$\delta = \frac{1}{\sqrt{\pi f \mu \sigma}} \quad (2.40)$$

then the conductor skin-effect can be ignored. The skin depth as a function of frequency has been plotted in Figure 2.14 for a typical aluminum conductor. It can

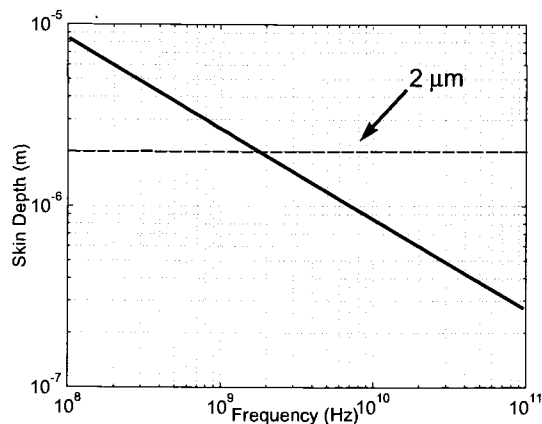


FIGURE 2.14. Skin depth for aluminum conductor.

be seen that the skin-effect will become noticeable between 1 and 2 GHz for an

aluminum spiral with $2\mu\text{m}$ metallization thickness. Obviously, for a scalable model to be accurate to at least 10GHz, this effect must be included. Another effect which is important even at low frequencies is the proximity effect. This effect is difficult to describe quantitatively but can be approached qualitatively. Essentially, two or more conductors that are physically close can have over-lapping magnetic fields, causing non-uniform currents. This effect is also dependent on frequency and is important in the 1 to 10GHz.

Both of these effects can be included in the PEEC model by using a technique described in [43]. To capture the effect of non-uniform current distribution over the conductors cross-section, each individual conductor segment can be discretized into multiple rectangular filaments. This technique is illustrated in Figure 2.15. Each of

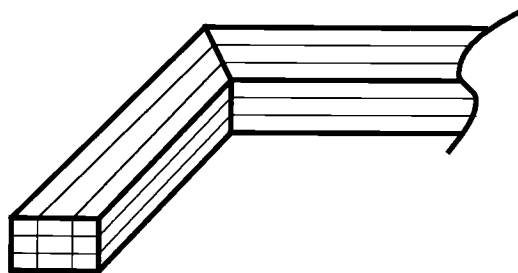


FIGURE 2.15. Sub-division of segments into multiple filaments.

the individual filaments is treated as a separate conductor with a partial inductance and resistance. The conductor skin effect is modeled through the partial mutual inductances between individual filaments inside a single conductor. Partial mutual inductances between filaments of different segments model the proximity effect.

Mathematically, this discretization can be summarized by reformulating (2.5) as

$$\mathbf{J}(\mathbf{r}, t) = \sum_{i=1}^K p_i I_i(t) \hat{l}_i \quad (2.41)$$

where the summation is now over all of the filaments in the entire conductor structure, and the functions p_i and $I_i(t)$ refer to the individual filaments. This change is a minor one and carries through all of the derivations in Section 2.2. Perhaps the most noticeable change is to the form of the equivalent circuit. As Figure 2.16 shows, each branch will now contain multiple, parallel branches containing partial resistances and partial inductances.

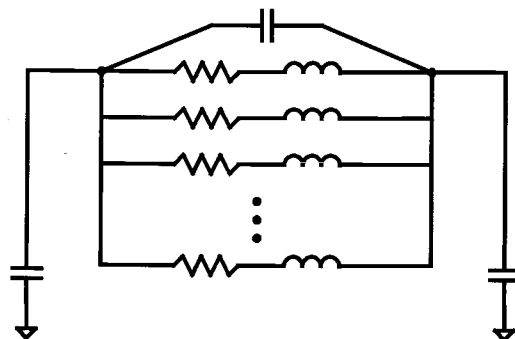


FIGURE 2.16. Equivalent circuit including the proximity and conductor skin-effect.

2.3.3. Spiral-Substrate Coupling Through the \vec{E} -Field

The coupling of signals through a lossy silicon substrate by the time-varying electric field is a well known problem and has been studied extensively, [40]. In

general, the coupling is a function of the substrate resistivity and frequency. In this section the PEEC model is extended to include the frequency-dependent electric field coupling through a multi-layer lossy substrate. The approach is based on considering adjacent segments of the spiral inductor as coupled transmission lines [33]. To facilitate this approach, only “nearest-neighbor” coupling is considered.

Considering the problem of a multi-turn spiral inductor, various segments can be classified according to whether they have neighboring segments on one or both sides. An example 2.5 turn spiral inductor is shown in Figure 2.17. The

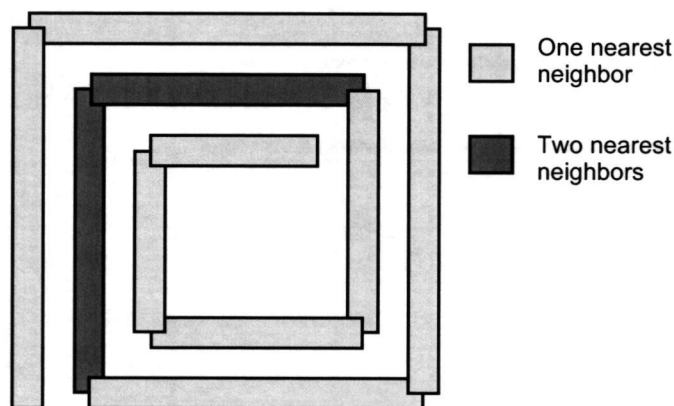


FIGURE 2.17. 2.5 turn spiral inductor with one- and two nearest-neighbor coupling.

coupling information for both of these types of segments can be approximately found from a 3-coupled transmission line simulation as shown in Figure 2.18. The substrate coupling is represented in terms of a frequency dependent network of Per-Unit-Length (PUL) conductances and capacitances. These frequency-dependent line parameters can be found using a fast quasi-static SDA technique [44]. For segments

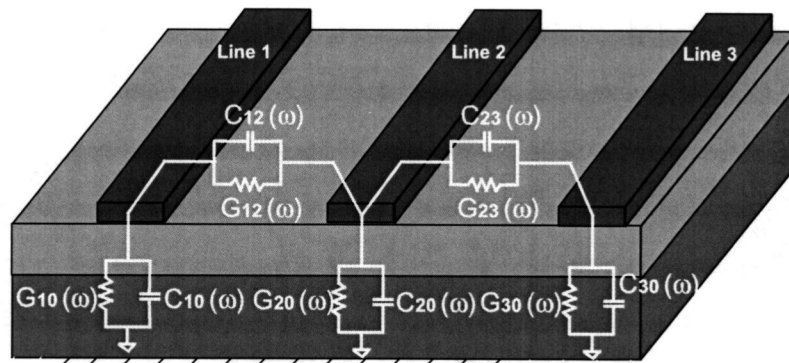


FIGURE 2.18. Symmetric 3-coupled transmission lines as approximation to spiral inductor segments.

with only one immediate neighbor, the self coupling can be obtained from lines 1 or 3 of the 3-coupled transmission line. Segments with two nearest neighbors will have self coupling similar to line 2, this takes into account the electric interaction of both neighbors. Mutual coupling for both types of segments can be obtained from either lines 1 and 2 or 2 and 3, due to the symmetry of the lines. The underpass segment is approximated as only having self coupling so the PUL information is obtained from a single transmission-line simulation.

The PUL line-parameters are converted to partial capacitances and conductances using the physical lengths of the various segments. The line-to-line partial coupling is found using the average length of two segments and the self coupling is found from the lengths of each segment separately. The partial components are split and applied at each end of the segments because of the locations of the equivalent circuit nodes.

By using a transmission-line approximation to the coupling between various segments in the spiral inductor, an efficient spectral domain approach can be used.

This technique obtains all of the necessary coupling information for the entire spiral inductor with only two transmission line simulations, 3-coupled line and single line. Due to the lossy substrate, the PUL line-parameters are frequency-dependent and must be obtained at each frequency point of interest. The PUL line-parameters are converted to partial components using the average lengths for mutual coupling and actual lengths for self coupling.

2.4. Solution of the Complete Equivalent Circuit

To summarize the extended PEEC model presented in the previous sections, the equivalent circuit for a 1.25 turn rectangular spiral, as shown in Figure 2.19, is described. The equivalent circuit for this inductor is shown in Figure 2.20 where

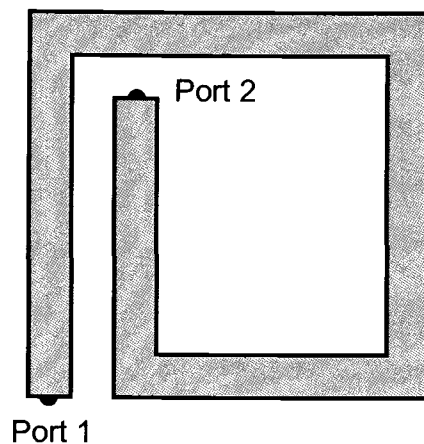


FIGURE 2.19. 1.25 turn rectangular spiral inductor.

all but the first and last segments have been omitted for clarification. Each segment is replaced with a parallel combination of partial resistances and inductances. Magnetic coupling between the various filaments and segments is represented in terms of mutual inductances and resistances. The electric coupling between each segment and the ground plane is included through the parallel G-C sub-circuits connected from each node to ground. Similar G-C sub-circuits are used to include the electric coupling between segments one and five according to the nearest-neighbor approximation.

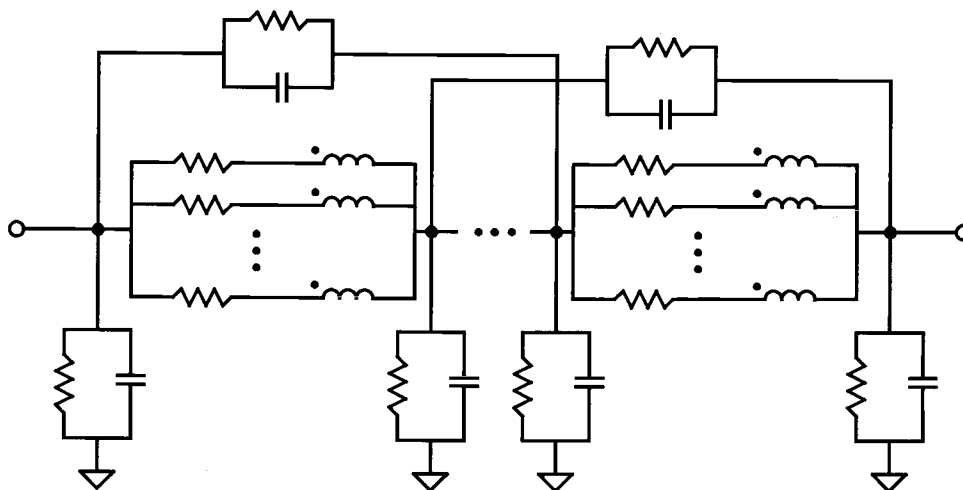


FIGURE 2.20. Equivalent circuit for 1.25 turn spiral inductor.

In general, the equivalent circuit of the spiral inductors considered in this research can be represented in terms of frequency-dependent network parameters. Specifically, the two-port Y-parameters are sought because they provide useful information about the frequency domain characteristics of the spiral inductor including

the inductance, resistance, and Q. The two-port Y-parameters are defined by the matrix equation

$$\begin{bmatrix} i_1 \\ i_2 \end{bmatrix} = \begin{bmatrix} y_{11} & y_{12} \\ y_{21} & y_{22} \end{bmatrix} \begin{bmatrix} v_1 \\ v_2 \end{bmatrix} \quad (2.42)$$

where the current and voltages are defined in Figure 2.21. Because of their simple

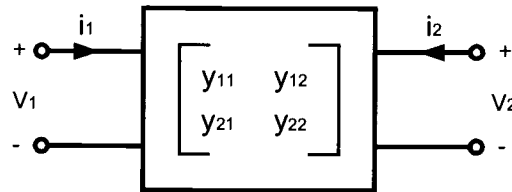


FIGURE 2.21. Current and voltage definitions for Y-parameters.

relationship to the voltages and currents at the ports of the equivalent circuit, the Y-parameters can be found in a straight-forward manner. The Y-parameters, y_{1x} and y_{2x} , can be found by applying a unit voltage source to port x and shorting the other port to ground. The branch currents at the ports give the desired Y-parameters with perhaps a sign change to account for the defined current directions.

In the following, Modified Nodal Analysis (MNA), [45], [46], is presented as an efficient method for finding the branch currents, and hence the Y-parameters, of the equivalent circuits of spiral inductors. MNA was chosen because of its ability to provide a solution for the complete equivalent circuit while using separate network descriptions for the R-L-M and G-C portions of the circuit. This is important because of the variable complexity of each sub-circuit depending on the number

of filaments-per-segment and the coupling approximation used. This separation is clear in the general tableau formulation of MNA which can be stated as

$$\begin{bmatrix} \mathbf{J}_n \\ \mathbf{W}_{b2} \end{bmatrix} = \begin{bmatrix} \mathbf{A}_1 \mathbf{Y}_{b1} \mathbf{A}_1^t & \mathbf{A}_2 \\ \mathbf{Y}_{b2} \mathbf{A}_2^t & \mathbf{Z}_{b2} \end{bmatrix} \begin{bmatrix} \mathbf{V}_n \\ \mathbf{I}_{b2} \end{bmatrix} \quad (2.43)$$

The sub-matrices in (2.43) with a subscript of “1” are used to describe a portion of the equivalent circuit with a branch admittance formulation. The sub-matrices with a subscript of “2” describe a part of the circuit with a branch impedance formulation. The unknowns in (2.43), \mathbf{V}_n and \mathbf{I}_{b2} , are the node voltages of the entire circuit and the branch currents of the circuit in partition 2, respectively. The source vector consisting of \mathbf{J}_n and \mathbf{W}_{b2} includes the effects of independent current sources and independent voltage sources, respectively. The matrix equation stated in (2.43) can be solved for the unknown branch currents, hence the Y-parameters, by inversion of the tableau.

The tableau is assembled in a systematic way from the values of the partial elements and the structure of the equivalent circuit. Because of the natural separation of the equivalent circuit in Figure 2.20 into an R-L-M series sub-circuit and a G-C coupling sub-circuit, construction of the tableau can be performed in two major steps; first assembling the \mathbf{Y}_{b2} , \mathbf{Z}_{b2} , \mathbf{W}_{b2} , and \mathbf{A}_2 matrices for the R-L-M sub-circuit, then assembling the \mathbf{Y}_{b1} and \mathbf{A}_1 , for the G-C sub-circuit.

2.4.1. RLM Sub-Circuit

The network description of the R-L-M sub-circuit is considered first. The branch relations for the elements in this partition can be stated as

$$\mathbf{Y}_{b2} \mathbf{V}_{b2} + \mathbf{Z}_{b2} \mathbf{I}_{b2} = \mathbf{W}_{b2} \quad (2.44)$$

Entries in \mathbf{Y}_{b2} , \mathbf{Z}_{b2} , and \mathbf{W}_{b2} for several common components can be found by examining the individual constitutive relations

$$\text{Resistor} : V_b - R_b I_b = 0$$

$$\text{Inductor} : V_b - j\omega L_b I_b = 0$$

$$\text{Voltage - Source} : V_b = E_b$$

(2.45)

The entries in \mathbf{Y}_{b2} would be 1 for each of these components. The entries in \mathbf{Z}_{b2} would be $-R_b$, $-j\omega L_b$, and 0 for the resistor, inductor, and voltage source, respectively. Furthermore, the entries in the source vector, \mathbf{W}_{b2} would be 0 for the resistor and inductor, and the magnitude, E_b , for the voltage source. These ideas can be extended to the complete R-L-M sub-circuit of the 1.25 turn spiral inductor, as shown in Figure 2.22. The \mathbf{Z}_{b2} matrix for this circuit can be formed by combining the branch

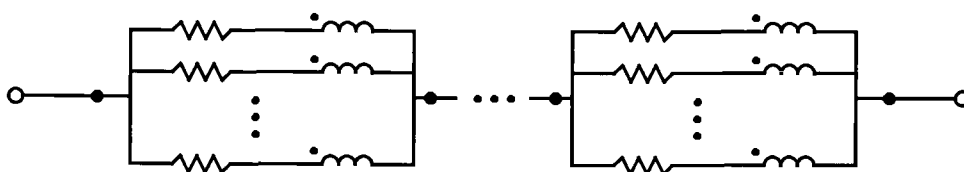


FIGURE 2.22. Series R-L-M sub-circuit for 1.25 turn spiral inductor.

impedance matrix for the R-L-M circuit with two extra columns and rows of zeros for the voltage sources that will be used at ports 1 and 2.

$$\mathbf{Z}_{b2} = \begin{bmatrix} 0 & 0 & \cdots & 0 \\ 0 & 0 & \cdots & 0 \\ \vdots & \vdots & -\mathbf{Z}_b & \cdots \\ 0 & 0 & \vdots & \ddots \end{bmatrix} \quad (2.46)$$

The branch impedance matrix, \mathbf{Z}_b , is defined as

$$\mathbf{Z}_b = \mathbf{R}_{b_{DC}} + j\omega\mathbf{L}_b \quad (2.47)$$

where $\mathbf{R}_{b_{DC}}$ is the branch resistance matrix of the inductor at DC and contains non-zero entries only along the diagonal. For example, $\mathbf{R}_{b_{DC}}(x, x)$, would be the self partial resistance of filament(branch) x and so on. The matrix \mathbf{L}_b is the complex-valued, branch inductance matrix as described by (2.32). Both of these matrices contain partial component values found using the techniques described in Sections 2.2.2 and 2.3.1. Overall, the \mathbf{Z}_{b2} matrix is $(m+2)$ by $(m+2)$, where m is the number of filaments in the equivalent circuit and the extra two rows and columns are due to the voltage sources.

The matrix \mathbf{Y}_{b2} is also an $(m+2)$ by $(m+2)$ matrix, although for this type of circuit it becomes the identity matrix. In general, \mathbf{Y}_{b2} would contain entries for branches in partition 2 that are described by admittances.

The source vector \mathbf{W}_{b2} , in general, contains the magnitudes of all independent voltage sources in the circuit. In this case, only two entries can be non-zero, and \mathbf{W}_{b2} can be written as

$$\mathbf{W}_{b2} = \begin{bmatrix} E_{b1} \\ E_{b2} \\ 0 \\ \vdots \\ 0 \end{bmatrix} \quad (2.48)$$

Here the voltage sources have been defined as branches one and two of the equivalent circuit. To find y_{11} and y_{21} , $E_{b1} = 1\text{v}$ while $E_{b2} = 0\text{v}$ and vice versa to find y_{12} and y_{22} .

While the constitutive relationships described by (2.44) relate the branch currents and voltages of the R-L-M sub-circuit, they do not describe how the circuit is assembled. In fact, the branch and node numbering scheme is completely arbitrary. To include this information, \mathbf{A}_2 , the “branch incidence matrix”, must be formulated. This matrix describes to what nodes each branch is connected as well as the directions defined for positive branch currents. In general, a branch incidence matrix must satisfy KCL for the circuit being solved. KCL can be stated in matrix form as

$$\mathbf{A}\mathbf{I}_b = \mathbf{0} \quad (2.49)$$

It also must satisfy KVL which can be stated as

$$\mathbf{A}^T\mathbf{V}_n = \mathbf{V}_b \quad (2.50)$$

Where \mathbf{I}_b , \mathbf{V}_b , and \mathbf{V}_n are the branch currents, branch voltages, and node voltages of the R-L-M sub-circuit, respectively. Each column of the incidence matrix corresponds to a branch of the circuit while each row corresponds to a node. Every column will have only one or two non-zero entries. For branches connected between two circuit nodes, a 1 is placed in the row corresponding to the node that the branch current leaves and a -1 in the row corresponding to the node that the branch current enters. Branches connected between a circuit node and the ground node have only a single non-zero entry, a 1 or -1 (depending on the current direction) in the row corresponding to the circuit node. The repetitive nature of the series R-L-M

components make this matrix straight-forward to assemble. A possible formulation of the incidence matrix for the R-L-M sub-circuit could be

$$\mathbf{A}_2 = \begin{bmatrix} 1 & 0 & 1 & 0 & 0 & \cdots & 0 \\ 0 & 0 & -1 & 1 & 0 & \cdots & 0 \\ 0 & 0 & 0 & -1 & 1 & \cdots & 0 \\ 0 & 0 & 0 & 0 & -1 & \cdots & 0 \\ \vdots & \vdots & \vdots & \vdots & \vdots & \ddots & \vdots \\ 0 & 0 & 0 & 0 & 0 & \cdots & 1 \\ 0 & 1 & 0 & 0 & 0 & \cdots & -1 \end{bmatrix} \quad (2.51)$$

The first two columns show the connections of the two voltage sources as being between ports one and two and ground, this also infers that the sources are branches one and two. This formulation assumes that the branch currents in all of the filaments are assumed to flow from port one towards port two, the nodes and filaments are numbered starting from port one and ending at port two, and that there is only one filament per segment, i.e. no discretization. If the segments were discretized, the incidence matrix would have multiple identical columns for each parallel filament.

2.4.2. GC Sub-Circuit

The G-C coupling portion of the equivalent circuit, shown in Figure 2.23, can be described with the branch-admittance relationship

$$\mathbf{Y}_{b1} \mathbf{V}_{b1} = \mathbf{I}_{b1} \quad (2.52)$$

where \mathbf{V}_{b1} and \mathbf{I}_{b1} are the branch voltages and currents and \mathbf{Y}_{b1} is the branch admittance matrix. For the G-C sub-circuit in Figure 2.23 the branch admittance matrix can be formulated as

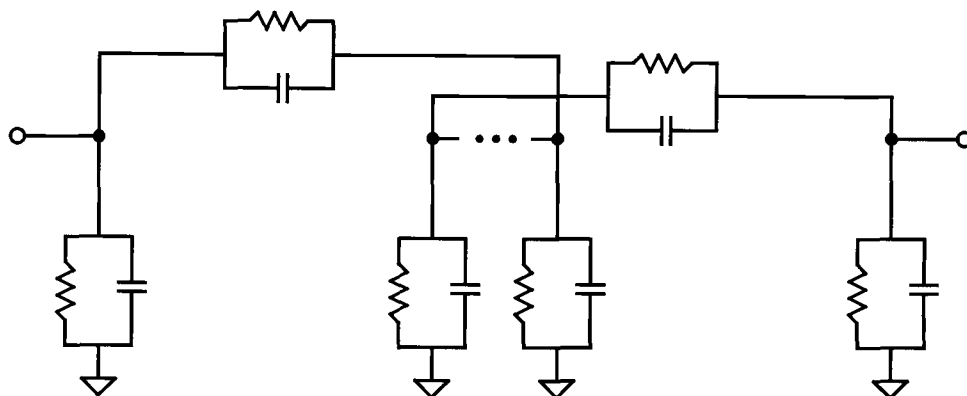


FIGURE 2.23. G-C coupling sub-circuit for 1.25 turn spiral inductor.

$$\mathbf{Y}_{b1} = \mathbf{G}_{b1} + j\omega\mathbf{C}_{b1} \quad (2.53)$$

For this type of sub-circuit, both \mathbf{G}_{b1} and \mathbf{C}_{b1} contain non-zero entries only along their diagonals. The entries can be found using the technique explained in Section 2.3.3. The branch numbering scheme determines the order of the entries, while the number of segments and the coupling approximation used affects the number of entries (i.e. the overall size of the branch admittance matrix). For rectangular spiral inductors, the “nearest-neighbor” approximation results in $4t + 1$ self coupling terms, as well as $4t - 3$ nearest-neighbor terms, where t is the number of turns.

It is also necessary to formulate an incidence matrix, \mathbf{A}_1 , for the G-C sub-circuit. For the 1.25 turn rectangular spiral in Figure 2.19, the \mathbf{A}_1 matrix can be written as

$$\mathbf{A}_1 = \begin{bmatrix} 1 & 0 & 0 & 0 & 0 & 0 & 1 & 0 \\ 0 & 1 & 0 & 0 & 0 & 0 & 0 & 1 \\ 0 & 0 & 1 & 0 & 0 & 0 & 0 & 0 \\ 0 & 0 & 0 & 1 & 0 & 0 & 0 & 0 \\ 0 & 0 & 0 & 0 & 1 & 0 & -1 & 0 \\ 0 & 0 & 0 & 0 & 0 & 1 & 0 & -1 \end{bmatrix} \quad (2.54)$$

where the first six columns describe the connections of the shunt coupling from each node to ground and the last two columns include the lateral coupling between segments one and five.

Finally, the vector \mathbf{J}_n contains n entries, where n is the number of nodes. Each entry of this vector contains the sum of all independent current sources connected to a particular node. For the equivalent circuits considered in this thesis, the vector \mathbf{J}_n contains all zeros as there is no need for current sources.

Because of the frequency dependent nature of many of the partial elements that comprise the equivalent circuits, the \mathbf{Y}_{b1} , \mathbf{Y}_{b2} , and \mathbf{Z}_{b2} sub-matrices must be computed at each frequency point. Hence, the tableau must be constructed and inverted at each frequency point. Despite this drawback, the MNA approach provides an efficient method for solving the equivalent circuits determined from the enhanced PEEC analysis.

2.5. Conclusion

The need for accurate frequency-domain information from spiral inductors has increased as wireless applications have become popular. This chapter has presented an alternative to the time-consuming full-wave simulations that typically

must be used to obtain accurate results. Specifically, a PEEC model has been presented which allows the complex electromagnetic problem to be replaced with an equivalent circuit built from frequency-dependent lumped elements. The conductor-skin and proximity effects are included through subdivision of the spiral inductor segments. Magnetic field losses in the lossy silicon substrate are included using an efficient complex-image technique. This complex-image approach makes use of existing closed-form equations for partial inductance in free-space. The frequency-dependent electric field coupling is included using a transmission-line approximation. This allows the use of a fast quasi-static SDA solver to find the partial component values. The complete equivalent circuit is assembled and solved at each frequency point for the two-port Y-parameters through MNA. This circuit solution technique allows the series R-L-M and G-C coupling networks to be described with different methods, while providing a solution for the entire equivalent circuit. This combined approach includes all major non-ideal effects and can be used for a number of spiral inductor geometries and substrate configurations.

3. COMPACT EQUIVALENT-CIRCUIT MODELLING

3.1. Introduction

While the frequency-domain information obtained from the enhanced PEEC model presented in Chapter 2 is useful for predicting how a spiral inductor will perform, it lacks the ability to be directly used in a time-domain simulation. This is due, in part, to the large number of circuit elements composing the equivalent circuit. Perhaps more importantly, most commercial circuit simulators lack the ability to incorporate frequency dependent components into time-domain simulations. As such, ideal compact circuit models, usable for time-domain simulations, can be very useful to the RFIC design engineer. To give designers a real benefit, the compact model topology should use a minimum number of ideal lumped elements while offering a maximum amount of modeling flexibility. Furthermore, having a robust automated extraction procedure is desirable to reliably and efficiently extract the model parameters for a given spiral inductor design.

This chapter presents a methodology for wide-band compact modeling of spiral inductors on lossy silicon substrate including automated parameter extraction. Section 3.2 discusses the typical frequency domain behavior of spiral inductors on lossy silicon, as an understanding of these trends is critical to developing wide-band compact models. Emphasis is given to the series and shunt information obtained from a frequency dependent pi-model calculated from the two port Y-parameters. Section 3.3 discusses the commonly used nine-element compact model and addresses its inability to accurately reproduce several of the trends discussed in Section 3.2. A new wide-band compact model suitable for spiral inductors on high-loss substrates

is described in Section 3.4. Finally, Section 3.5 details the extraction procedure developed for the new wide-band compact model.

3.2. Frequency Domain Trends of Spiral Inductors

To develop wide-band compact models for spiral inductors, it is useful to first explore their frequency domain characteristics. This understanding can provide a logical basis for developing new compact models as well as choosing from existing ones. Most often, when spiral inductors are characterized over a wide frequency

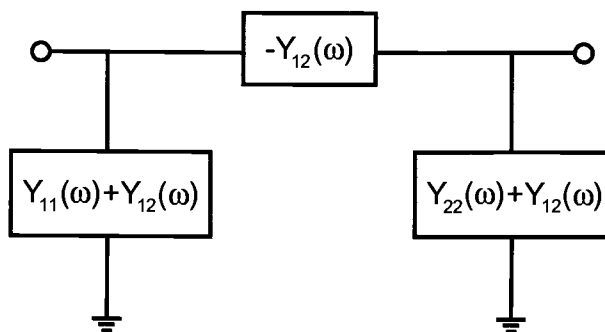


FIGURE 3.1. Generic Two-Port Y-parameter Pi-model.

range, a network analyzer is used to measure the S-parameters. While this can provide accurate wide-band information about a spiral inductor, it gives little insight to component characteristics such as Q or inductance. However, this information can be easily obtained through Y-parameters. Y-parameters are particularly useful to this study because of their natural relationship to the two-port pi-model shown in Figure 3.1. This pi-model configuration can be used to separate the series and shunt

information from a set of measurements. By making some assumptions about the

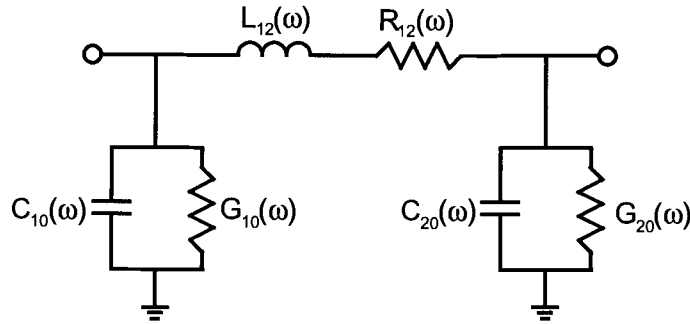


FIGURE 3.2. Frequency-dependent pi-model for spiral inductors on silicon substrates.

physical nature of a spiral, a frequency-dependent compact equivalent circuit can be found, based on the Y-parameter pi-model. This equivalent circuit for spiral inductors, shown in Figure 3.2, is mainly useful as a way to interpret the Y-parameter measurements. Logically, the series circuit is chosen to consist of a frequency dependent inductance, $L_{12}(\omega)$, and resistance, $R_{12}(\omega)$, connected in series between ports one and two. Each shunt circuit contains a parallel-connected conductance, $G_{x0}(\omega)$, and capacitance, $C_{x0}(\omega)$ ($x = 1, 2$). These components can be calculated from Y-parameters using the following relationships

$$L_{12}(\omega) = \frac{\mathbf{Im}\left(\frac{-1}{Y_{12}(\omega)}\right)}{\omega}$$

$$R_{12}(\omega) = \mathbf{Re}\left(\frac{-1}{Y_{12}(\omega)}\right)$$

$$C_{x0}(\omega) = \frac{\mathbf{Im}(Y_{xx}(\omega) + Y_{12}(\omega))}{\omega}$$

$$G_{x0}(\omega) = \mathbf{Re}(Y_{xx}(\omega) + Y_{12}(\omega))$$

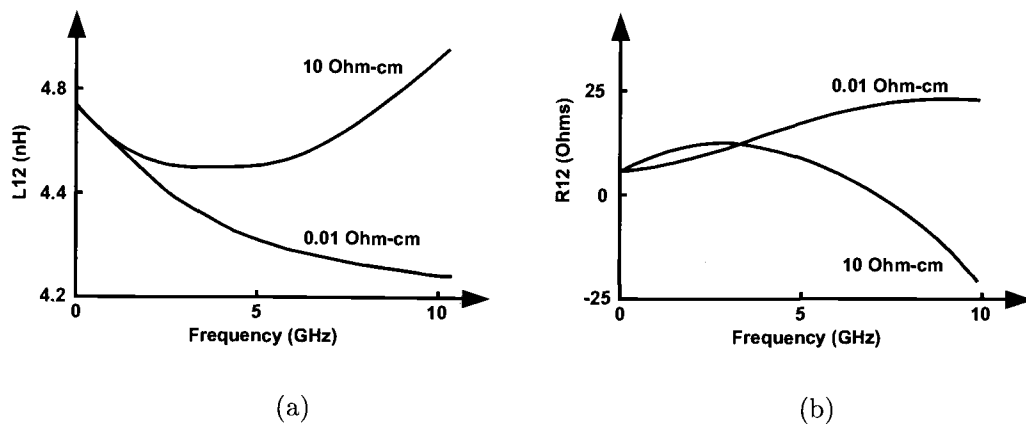


FIGURE 3.3. Trends for $L_{12}(\omega)$ and $R_{12}(\omega)$.

(3.1)

The resulting six circuit parameters are not only functions of frequency, but are also geometry and substrate dependent. Unfortunately, there can be drastic differences in several of these trends as substrate resistivity is varied. In the following, average frequency domain behavior is described for a medium sized spiral inductor on low- and high-loss substrates. Figures 3.3, 3.4, 3.6, 3.8, and 3.9 have been created with vertical axes to give the reader an idea of the magnitudes and units associated with the various trends.

Typical trends of $L_{12}(\omega)$ and $R_{12}(\omega)$ for a medium sized spiral inductor on high and low-loss substrates have been plotted in Figure 3.3(a) and (b), respectively. In Figure 3.3(a), both cases of substrate resistivity result in a series inductance that decreases at low frequencies due to the conductor skin- and proximity-effect. As frequency increases, however, the higher resistivity case begins to increase in anticipation of a resonance. This resonance is not the same as the self-resonance of

the spiral inductor which can be observed when one of the ports is excited and the other is shorted to ground. In contrast, the series inductance of the lower resistivity case continues to decrease as the eddy currents move closer to the spiral, effectively cancelling the flux of the inductor. The series resistance shown in Figure 3.3(b) is also quite different for both substrate cases. The high-resistivity case exhibits a peak and then becomes increasingly negative. This phenomenon is usually attributed to the distributed nature of the spiral inductor and signifies the increasing phase delay between ports one and two. For the lower-resistivity case, the trend in $R_{12}(\omega)$ is dominated by the losses associated with the eddy-currents flowing in the substrate. Generally, spiral inductors on high loss substrates will not exhibit a negative series resistance until a much higher frequency as compared to the low-loss case. This can be explained by considering the different propagation modes of on-chip microstrip transmission lines. Using Hasegawa's nomenclature, [47], microstrip on the low-loss substrate (between 1 and 10 GHz) operates in the transition region between the "slow-wave" and "dielectric quasi-TEM" modes, resulting in a lower phase velocity. By comparison, microstrip on the high-loss substrate, over the same frequency range, is operating in the "skin-effect" mode which has a much larger phase velocity, hence a smaller phase delay between ports one and two.

Figure 3.4(a) and (b) show the typical trends for the shunt capacitances and conductances as functions of frequency and substrate resistivity. The trends have similar shapes for both substrate cases but the lower loss case has a much stronger dependence on frequency in the low GHz range. This behavior can also be related to the transition from slow-wave to dielectric quasi-TEM propagation modes. In general, the shunt information at ports one and two will be somewhat different because of the asymmetric nature of most spiral inductors.

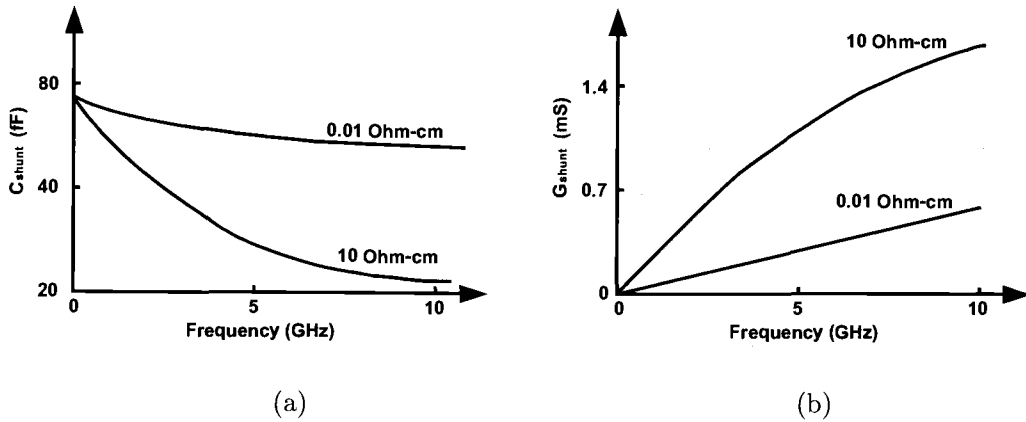


FIGURE 3.4. Trends for shunt G and C.

3.3. Nine-Element Compact Model

Although the frequency dependent model shown in Figure 3.2 is a step in the right direction, it does not achieve the goal of a (true) time-domain model built from ideal lumped components. One of the most commonly used compact spiral inductor models, which can be used in the time-domain, is the standard “9-element” pi-model (e.g. [31], [32]), which is shown in Figure 3.5. The series branch of the 9-element model consists of a series combination of a fixed ideal inductor, L_s , and resistor, R_s , together with a parallel-connected capacitor, C_c . The coupling capacitance, C_c , is usually thought of as representing the capacitive coupling to the underpass as well as between the turns of the spiral inductor. While this model has been successfully used over a wide frequency range for spiral inductors on low-loss substrates such as high-resistivity silicon (HRS) or sapphire [48], it does not properly model wide-band eddy-current loss in the silicon substrate for medium to heavily doped silicon processes. As mentioned previously, this loss effect (along with several others) can

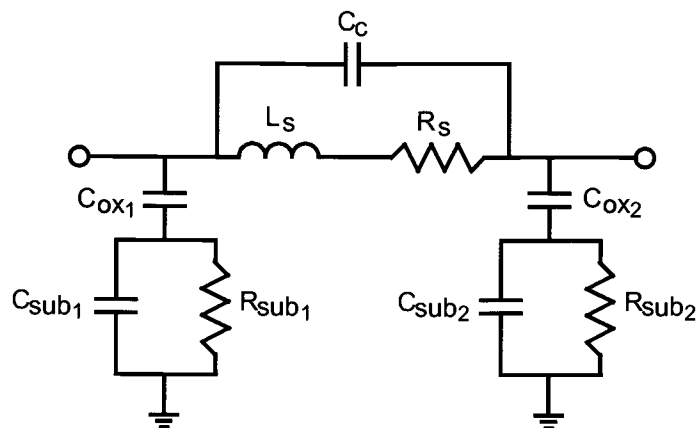


FIGURE 3.5. Nine-element compact model.

cause a pronounced dip in the inductance as a function of frequency. The trends obtainable from the series circuit of a typical 9-element model are shown in Figure 3.6(a) and (b). It can be observed that below the resonant frequency of the 9-element model's series branch, the inductance and resistance are both monotonically increasing functions of frequency. These trends limit the usefulness of the 9-element model's series-circuit as part of a wide-band compact model for spiral inductors on low resistivity substrates.

The shunt circuit used in the 9-element model is usually known as a standard "C-GC" circuit topology and has been successfully used in wide-band modelling of transmission lines on Si-SiO₂ substrates [49], [50]. The trends of the C-GC shunt circuit, as well as a more generalized version, are discussed in detail in the following section.

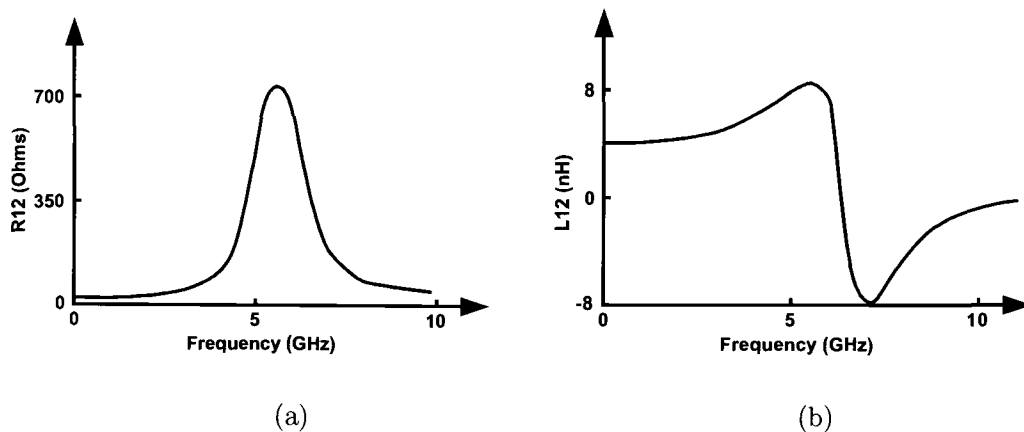


FIGURE 3.6. Trends for L12 and R12 for the 9 element model.

3.4. Transformer-Loop Compact Model

Due to the shortcomings of the 9-element model when applied to spirals on lossy substrates, a new compact model has been developed which is particularly suited to this case. The new compact model achieves high accuracy over a wide frequency range by using transformer loops (similar to the substrate current loops used in the equivalent circuit model for on-chip interconnects [49], [50]) to model the effects of frequency-dependent losses in spiral inductors, in particular eddy-current loss in low-resistivity silicon substrates. This new topology is also desirable because it leads to a simple automated extraction procedure, described in detail in Section 3.5.

Figure 3.7 shows the wide-band transformer-loop compact model for spiral inductors, [51], [52]. In what follows, the series and shunt circuits of the new model are described in detail as well as the frequency domain trends they are capable of producing.

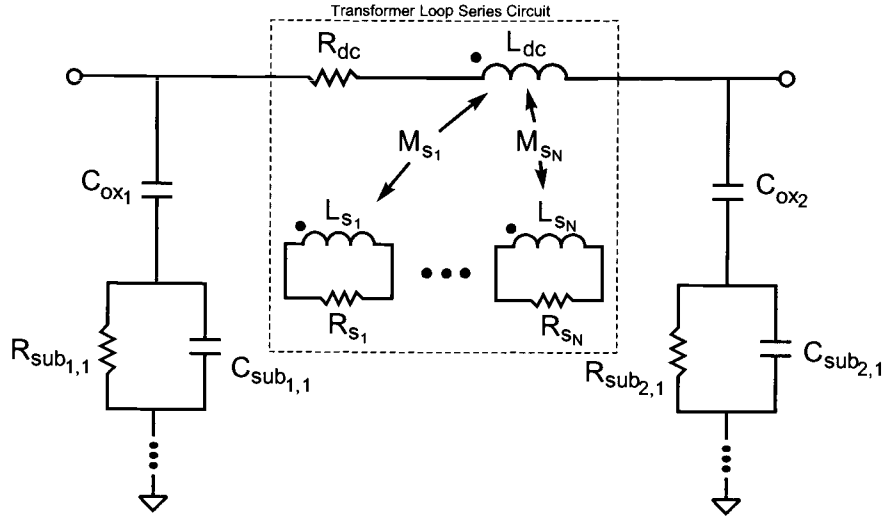


FIGURE 3.7. Wide-band compact equivalent-circuit model for spiral inductors on lossy substrates.

3.4.1. Series Circuit

The inductance L_{dc} and resistance R_{dc} in the series branch represent the spiral inductor's series resistance and inductance at the low frequency limit. The coupling capacitance, commonly used in the 9-element model, has been neglected to obtain the correct trends for $L_{12}(\omega)$ and $R_{12}(\omega)$. The inductance L_{s_i} and resistance R_{s_i} simulate the i th transformer loop to account for the frequency-dependent losses. The mutual inductances M_{s_i} between L_{s_i} and L_{dc} can be thought of representing the inductive coupling between the spiral metallization and the semiconducting substrate. The impedance of the series branch with transformer loops is given by [50]:

$$Z_{series}(\omega) = R_{dc} + j\omega L_{dc} - \sum_{i=1}^N \frac{M_{s_i}^2(j\omega)^2}{R_{s_i} + j\omega L_{s_i}} \quad (3.2)$$

where N is the number of transformer loops. With only a single loop, the series

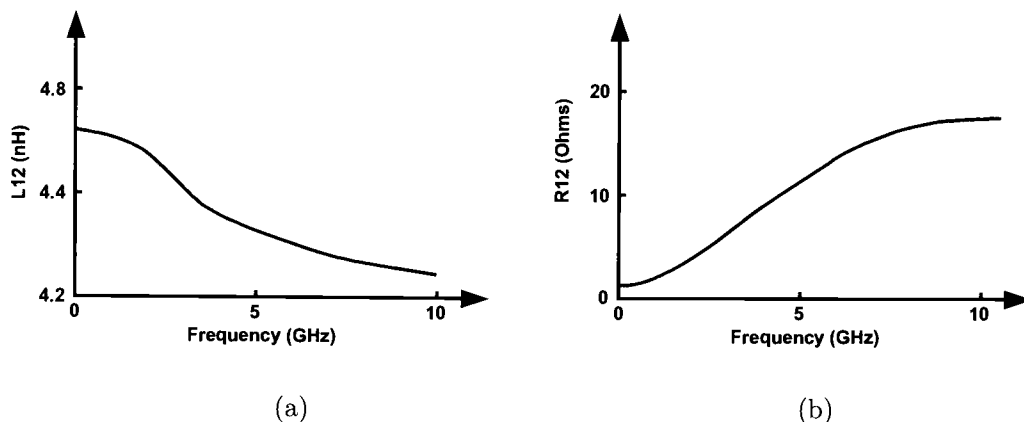


FIGURE 3.8. Trends for L_{12} and R_{12} for the transformer-loop model.

circuit is effectively a simple transformer with a resistive load. Each additional transformer loop adds an extra term to the summation in (3.2), which allows for more variability in the frequency response. In general, one or two loops are sufficient to provide a reasonable match to measured data.

Figures 3.8(a) and (b) show typical trends for $L_{12}(\omega)$ and $R_{12}(\omega)$ obtained with the transformer loop series circuit. At low frequencies the transformer loops are weakly coupled to L_{dc} such that the frequency response of the series circuit is dominated by L_{dc} and R_{dc} . As frequency increases, losses from the transformer loops are reflected back to L_{dc} causing a decrease in the series inductance and an increase in the series resistance.

3.4.2. Shunt Circuit

The standard C - GC topology consisting of ideal G and C elements is used for the shunt branches in the π -configuration of the wide-band compact model. In

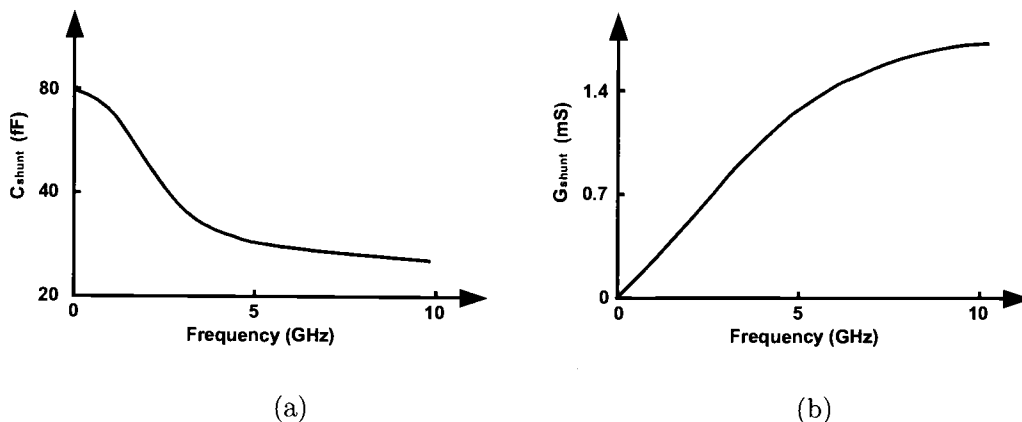


FIGURE 3.9. Trends for $C_{X0}(\omega)$ and $G_{X0}(\omega)$ for the C-GC shunt circuit.

certain cases, increased accuracy of the overall model can be obtained by using a more general shunt circuit. This can be realized by adding one or more parallel G - C combinations in series with the basic C - GC circuit. The input impedance of these augmented circuits is:

$$Z_{shunt_k}(\omega) = \frac{1}{j\omega C_{ox_k}} + \sum_{i=1}^N \frac{1}{G_{sub_{k,i}} + j\omega C_{sub_{k,i}}} \quad (3.3)$$

where N is the total number of GC combinations in the shunt circuit and k ($k = 1, 2$) is the port number. The typical trends that can be obtained with the basic C-GC and extended shunt circuits can be seen in Figures 3.9(a) and (b).

3.5. Extraction Procedure

An important consideration in developing compact models is the need for a fast and accurate means of extracting the component values. Typically, compact models, such as the 9-element model, are extracted using a time-consuming opti-

mizer. Because most optimizers involve an iterative solution process they can be prone to convergence problems, depending on the initial values supplied by the user. The optimizer may converge to a “local minimum” or possibly never reach convergence. To avoid these problems with the more complex transformer loop model, a robust CAD-oriented extraction methodology has been developed using a least-squares (LS) fitting procedure. Because of the large number of frequency points and limited number of components, the LS fitting procedure involves the solution of an over-determined system of equations.

As (3.2) and (3.3) show, both the series and shunt impedance functions include summations of single pole terms which can be combined as rational polynomial functions of $j\omega$. To take advantage of the rational polynomial form, Cauchy’s method [53], [54] is used to extract the component values involved in the summations. To illustrate the extraction procedure, the main steps are described for the series circuit branch. The shunt circuit extraction is similar, the main differences are explained.

3.5.1. Series Circuit

The series impedance can be directly obtained from the measured Y_{12} admittance parameter as

$$Z_{series}(\omega) = \frac{-1}{Y_{12}(\omega)} = R_{12}(\omega) + j\omega L_{12}(\omega) \quad (3.4)$$

The dc values of $L(\omega)$ and $R(\omega)$ can be found by separating the measured data, according to (3.4), into the resistive and inductive parts and extracting the low frequency asymptotes of both curves. After obtaining R_{dc} and L_{dc} , the remaining unknowns in (3.2) are isolated as follows

$$T(j\omega) =: \frac{R_{dc} + j\omega L_{dc} - Z_{series}(\omega)}{(j\omega)^2} = \sum_{i=1}^N \frac{M_{s_i}}{R_{s_i} + j\omega L_{s_i}} \quad (3.5)$$

The remaining terms on the RHS of (3.5) are due to the transformer loops and are contained in a summation of single pole functions. This summation can be rewritten as a rational polynomial in $j\omega$

$$T(j\omega) = \frac{a_0 + a_1(j\omega) + \dots + a_{N-1}(j\omega)^{N-1}}{b_0 + b_1(j\omega) + \dots + b_N(j\omega)^N} = \frac{N(j\omega)}{D(j\omega)} \quad (3.6)$$

Rewriting (3.6) and applying it at each frequency point ω_m ($m = 1, 2, \dots, M$) results in a set of M complex equations of the form

$$T(j\omega_m) * D(j\omega_m) - N(j\omega_m) = 0 \quad (3.7)$$

For the series circuit with two transformer-loops, (3.7) would be written as

$$T(j\omega_m) * (b_0 + b_1(j\omega) + b_2(j\omega)^2) - (a_0 + a_1(j\omega)) = 0 \quad (3.8)$$

It is desirable to satisfy (3.8) at all frequency points of interest, generating a system of equations. A matrix equation can be written to represent the system

$$\begin{bmatrix} T(j\omega_1) & (j\omega_1) * T(j\omega_1) & (j\omega_1)^2 * T(j\omega_1) & -1 & -(j\omega_1) \\ T(j\omega_2) & (j\omega_2) * T(j\omega_2) & (j\omega_2)^2 * T(j\omega_2) & -1 & -(j\omega_2) \\ \vdots & \vdots & \vdots & \vdots & \vdots \\ T(j\omega_M) & (j\omega_M) * T(j\omega_M) & (j\omega_M)^2 * T(j\omega_M) & -1 & -(j\omega_M) \end{bmatrix} * \begin{bmatrix} b_0 \\ b_1 \\ b_2 \\ a_0 \\ a_1 \end{bmatrix} = \begin{bmatrix} 0 \\ 0 \\ \vdots \\ 0 \end{bmatrix} \quad (3.9)$$

To force the coefficients to be real, each of the complex equations are further divided each into separate real and imaginary equations. The resulting system consists of $2M$ equations and $2N+1$ unknowns, where N is the number of transformer loops and

M is the number of frequency points. For most practical situations 1 or 2 transformer loops are used, resulting in 3 or 5 unknown coefficients, and the number of frequency points may be on the order of 100. The resulting system is vastly over-determined and cannot be solved by simple inversion.

At this point it is useful to summarize what is being attempted. Not only is the system over-determined but it is also a homogeneous equation, meaning a non-trivial solution will be needed. There are two reasons why attempting to find the exact solution to this system is a waste of time. First, it can be shown that if the column vectors of the coefficient matrix, A , are linearly independent then the only solution to the homogeneous equation $Ax = 0$ is the trivial solution, [55]. Second, because the frequency data can come from measurements, it is likely to contain noise which is undesirable for the equivalent circuit to reproduce. It is known, by inspection, that the column vectors of A are linearly independent so a different way to obtain the coefficients must be used.

If an arbitrary coefficient vector x , is considered as a possible solution, then the resulting error vector produced from this sub-optimal solution is

$$A\mathbf{x} = \mathbf{e} \quad (3.10)$$

It is possible to minimize the magnitude of the error, with respect to the Euclidian inner product, by rewriting (3.10) as the corresponding normal equation

$$A^T A\mathbf{x} = A^T \mathbf{e} = \mathbf{e}' \quad (3.11)$$

where the vector, \mathbf{e}' , can still be considered as the error of the approximation. The minimum error vector can be found by solving the eigenvalue equation

$$A^T A\mathbf{x} = \lambda_{min}\mathbf{x} \quad (3.12)$$

where λ_{min} is the minimum eigenvalue of A and \mathbf{x} is its associated eigenvector. The components of the resulting eigenvector provide the coefficients of the rational polynomial function, (3.5).

Now that the coefficients of the rational polynomial are known, a partial fraction expansion must be performed to obtain the poles and residues of the system

$$\frac{a_0 + a_1(j\omega) + \cdots + a_{n-1}(j\omega)^{n-1}}{b_0 + b_1(j\omega) + \cdots + b_n(j\omega)^n} \rightarrow \frac{r_1}{(j\omega) - p_1} + \cdots + \frac{r_n}{(j\omega) - p_n} \quad (3.13)$$

And finally, the component values can be obtained for the series circuit from the single pole functions

$$\frac{r_i}{(j\omega) - p_i} = \frac{\frac{M_{si}^2}{L_{si}}}{(j\omega) + \frac{R_{si}}{L_{si}}} \quad (3.14)$$

Obviously, only two of the three transformer loop components are exactly specified. For instance, L_{si} , the transformer loop self inductance, can be chosen arbitrarily as $1\mu H$. Note that this extraction approach is feasible because of the simple mapping between the coefficients of the resulting rational polynomial and the component values.

Some caution must be used with this approach however, in regard to the poles and zeros of the resulting rational polynomial function. Although this approach guarantees real coefficients, only solutions that have the proper poles and zeros can be used. The transformer loop series circuit, as with all RL or RC circuits, can only exhibit poles and zeros in a particular constellation, as shown in Figure 3.10. This restriction can be translated into the following rules for the poles and residues resulting from the partial fraction expansion

$$r_i > 0, \text{Im}(r_i) = 0 \quad (3.15)$$

and

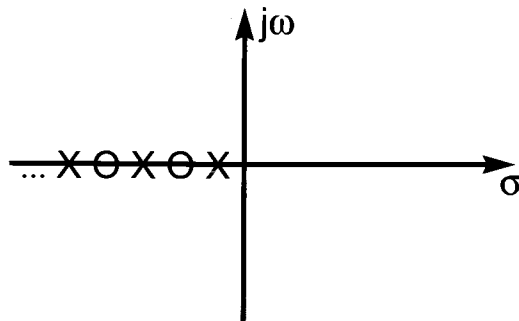


FIGURE 3.10. Pole-zero map for the series circuit of the transformer-loop model.

$$p_i < 0, \text{Im}(p_i) = 0 \quad (3.16)$$

There is nothing inherent in this least squares solution method that guarantees the resulting poles and residues will conform to (3.15) and (3.16). Experimentally, several factors have been determined which can influence the success of the extraction in terms of the pole/zero locations.

Two of the most important variables are the amount of noise and the overall shape, or trends, of the measurement data. Excessive noise can encourage complex pole pairs which the transformer loop circuit is unable to reproduce. This can be avoided by use of a noise reduction technique, such as LS polynomial curve fitting. The trends of the data used in the extraction can be adjusted by varying the values of the components L_{dc} and C_{ox} for the series and shunt circuit extractions, respectively. This is possible because base-line values for these components are calculated from the raw measurement data first, then used to transform the data prior to extraction. A change of only a few percent in these components can have a very distinct effect on the transformed data's, (3.5) and (3.17), frequency domain trends.

3.5.2. Shunt Circuit

The impedance function of the shunt circuits is similar in form to that of the series branch circuit, as can be seen from (3.3). C_{ox} can be extracted from the low frequency asymptote of the shunt impedance, and the impedance function is rearranged as follows:

$$Z_{shunt_k}(\omega) - \frac{1}{j\omega C_{ox_k}} = \sum_{i=1}^N \frac{1}{G_{sub_{k,i}} + j\omega C_{sub_{k,i}}} \quad (3.17)$$

This form directly leads to an extraction using Cauchy's method as explained above.

Because of the similarities in the impedance functions of the series and shunt circuits of the transformer-loop compact model, the same algorithm can be used to extract all three branches of the equivalent circuit, which leads to a very compact and efficient extraction procedure.

3.6. Conclusion

A new methodology for compact equivalent-circuit modelling of spiral inductors on lossy silicon has been presented. The modelling methodology consists of both a wide-band compact equivalent circuit model and an automated extraction procedure. The frequency-dependence in the series resistance and inductance of the spiral is modelled using coupled transformer loops, which mainly represent the effects of eddy-current loss in the semiconducting substrate. The automated extraction procedure is based on Cauchy's method and takes advantage of the simple mapping between the coefficients of the rational impedance functions and the equivalent circuit elements. The extracted transformer-loop model leads to a significant improvement in the ability to model the Q of a class of on-chip spiral inductors.

4. RESULTS

4.1. Octagonal Spiral on High-Loss Substrate

A 2.0nH octagonal spiral inductor on high-loss epi-substrate was chosen to demonstrate the wide-band accuracy of the enhanced-PEEC scalable-model and the transformer-loop compact-model. A representation of the spiral inductor layout is pictured in Figure 4.1. The underpass has been omitted to clarify the figure. This

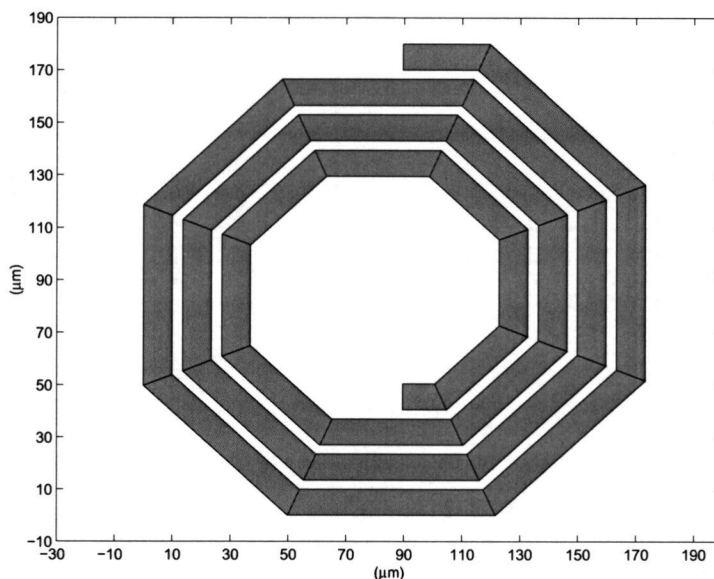


FIGURE 4.1. Layout of the 3.5 turn, 2.0 nH, octagonal spiral inductor on high-loss substrate.

spiral inductor was fabricated on a BiCMOS process with bulk and epi-layer conductivities of approximately 10^4 S/m and 10 S/m, respectively. The high conductivity of the bulk silicon indicates that eddy currents will have a strong effect on the per-

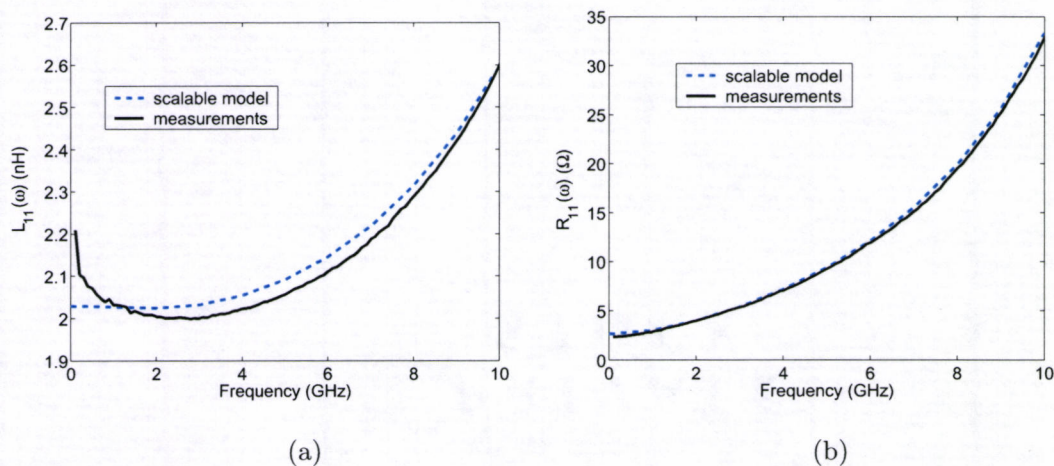


FIGURE 4.2. $L_{11}(\omega)$ and $R_{11}(\omega)$ for the 2.0nH spiral compared with PEEC model results.

formance of the spiral inductor. To reduce the series resistance of the spiral, a thick “bump-metal” layer was used. The underpass is fabricated in the next metal layer below the inductor.

4.1.1. Scalable Model Results

In this case, the PEEC model was configured to have 7 filaments in the width direction and 4 filaments in the height direction of each segment. The resulting one-port L, R, and Q are shown in Figures 4.2(a), (b), and 4.3, respectively. The scalable model is able to accurately predict the Q peak of 7.2 at approximately 4GHz. The series inductance and resistance are shown in Figures 4.4 and 4.5. As predicted in chapter 2, the series inductance decreases with frequency due to the eddy currents in the substrate, in this case nearly 20% over the 10 GHz frequency span. The combination of the conductor skin-effect and the reflected losses from the

substrate cause the series resistance to increase an astonishing 360% from its DC value.

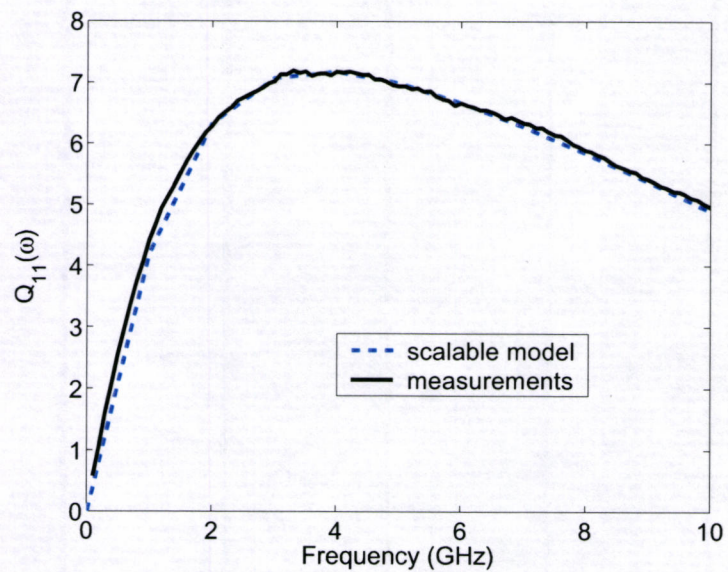


FIGURE 4.3. $Q_{11}(\omega)$ of the 2.0nH spiral compared with PEEC model results.

The shunt capacitance and conductance at port 1 are displayed in Figures 4.6 and 4.7, respectively. The excessive noise in the measurements at low frequencies can be attributed to inaccuracies in the de-embedding.

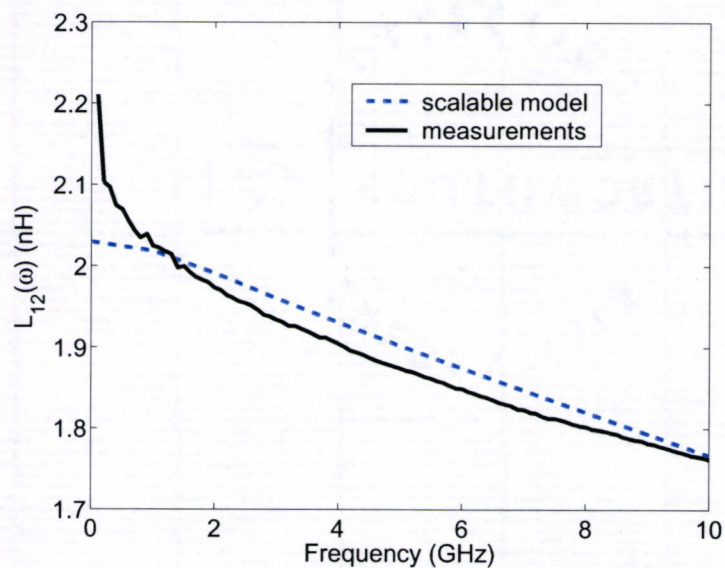


FIGURE 4.4. Series inductance of the 2.0nH spiral compared with PEEC model results.

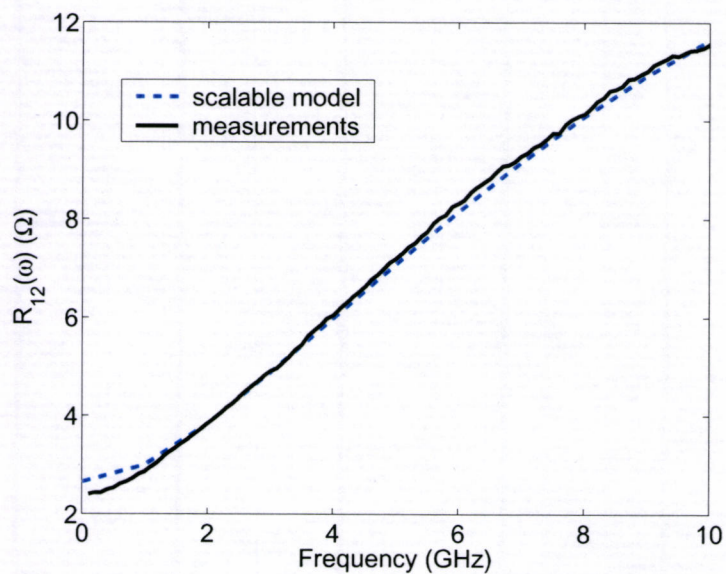


FIGURE 4.5. Series resistance of the 2.0nH spiral compared with PEEC model results.

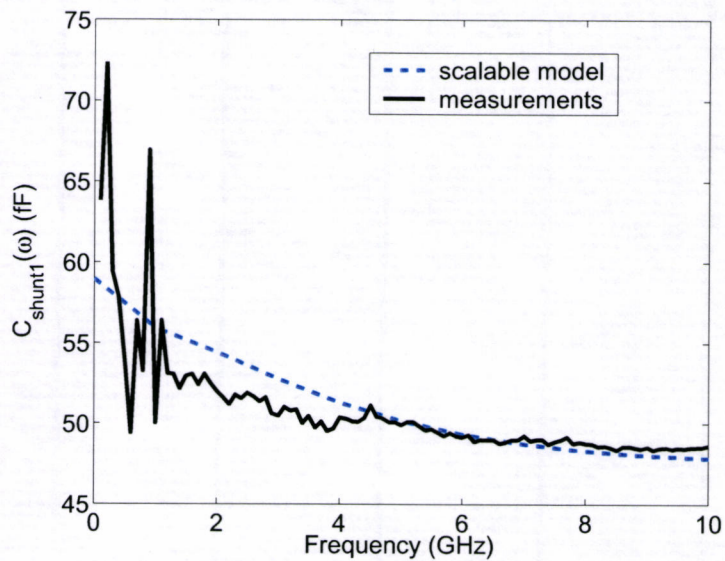


FIGURE 4.6. Shunt capacitance at port one of 2.0nH spiral compared PEEC model results.

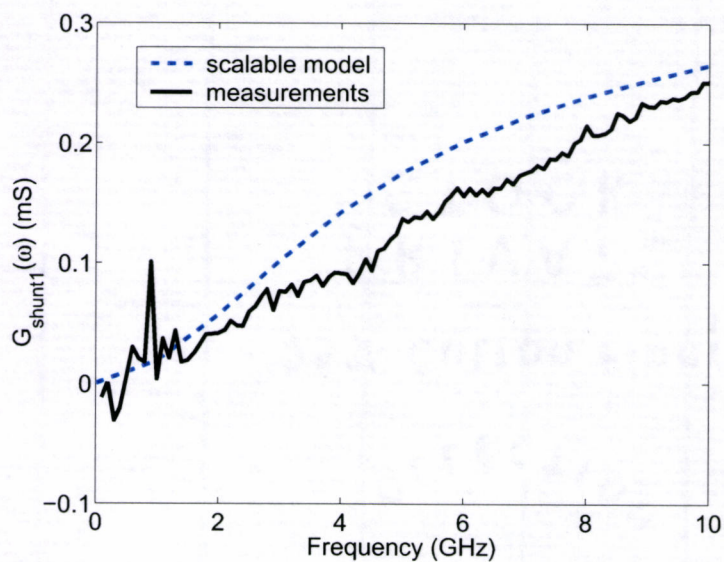


FIGURE 4.7. Shunt conductance at port one of 2.0nH spiral compared with PEEC model results.

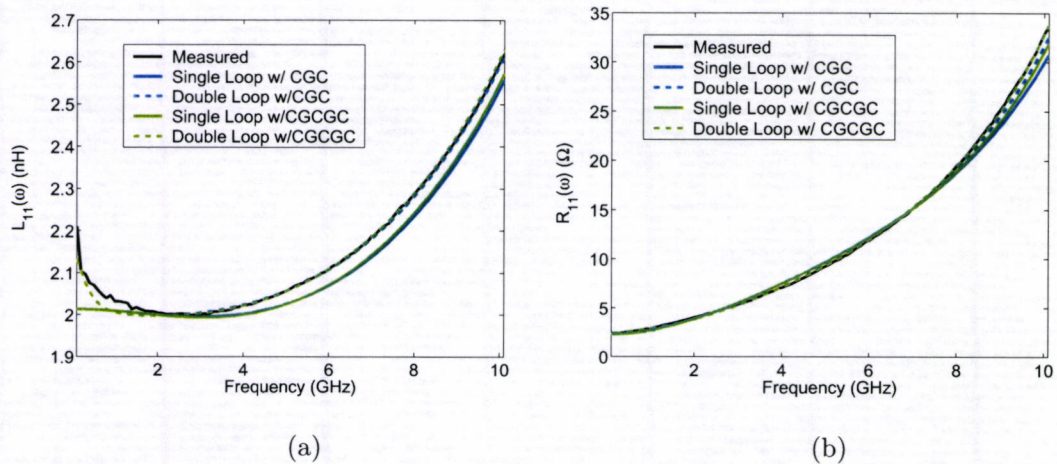


FIGURE 4.8. $L_{11}(\omega)$ and $R_{11}(\omega)$ for the 2.0nH spiral compared with transformer-loop compact model results.

4.1.2. Compact Model Results

Four different versions of the transformer-loop compact model were extracted from measurements of the 2.0nH spiral inductor. These different models are assembled from the single- and double-loop series circuits and the C-GC and C-GC-GC shunt circuits. The total L, R, and Q for the four models can be seen in Figures 4.8(a), (b), and 4.9. In this case, the addition of a second transformer loop provides a noticeable improvement in the overall response. The extra GC shunt circuit, on the other hand, does little to improve the overall response. Specifically, for Q_{11} , the average relative error for the single-loop CGC model is approximately 4.2%, while the additional transformer loop reduces this error to 1.5% over the 100MHz - 10GHz frequency range. The additional GC circuit reduces both of these errors by another 0.5%, approximately. The series inductances and resistances for the single- and double-loop models are shown in Figures 4.10(a) and (b), respectively. By adding a

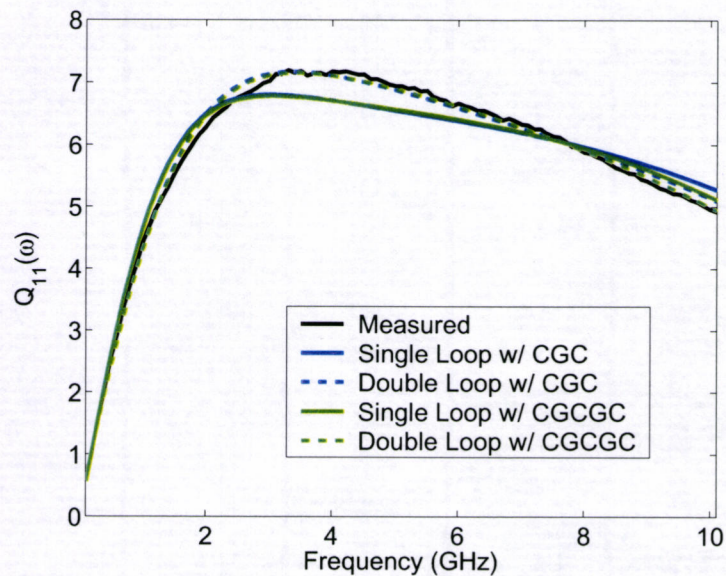


FIGURE 4.9. $Q_{11}(\omega)$ for the 2.0nH spiral compared with transformer-loop compact model results.

second transformer-loop, the average relative error for L_{12} and R_{12} decrease by 1% and 2.7% respectively. The component values extracted for the single and double loop series circuits are listed in Table 4.1.

The shunt capacitance and conductance for port one of the spiral inductor is compared with the extracted C-GC and C-GC-GC shunt circuits in Figure 4.11. It can be observed that the additional GC sub-circuit allows for greater flexibility in the shunt circuit response, similar to the difference between single- and double-loop series circuits. The component values extracted for the shunt circuits at ports one and two are listed in Table 4.2.

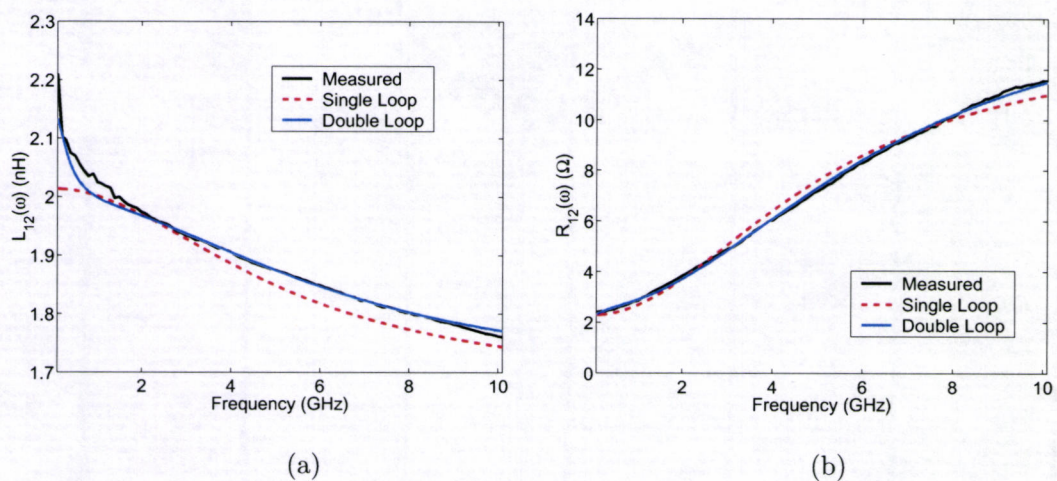


FIGURE 4.10. Series inductance and resistance of the 2.0nH spiral compared with the extracted single- and double-loop series circuits.

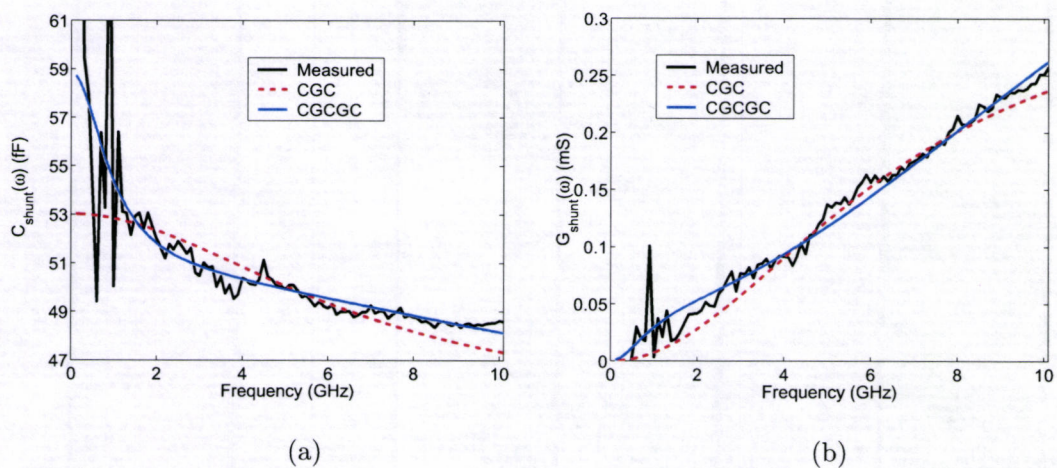


FIGURE 4.11. Shunt capacitance and conductance of the 2.0nH spiral compared with the extracted C-GC and C-GC-GC shunt circuits.

Component	Single-Loop	Double-Loop
R_{DC}	2.283 Ω	2.299 Ω
L_{DC}	2.014 nH	2.146 nH
R_{s1}	32,317.7 Ω	40,491.8 Ω
L_{s1}	1.0 μ H	1.0 μ H
M_{s1}	18.439 nH	17.563 nH
R_{s2}	—	2,126.9 Ω
L_{s2}	—	1.0 μ H
M_{s2}	—	12.520 nH

TABLE 4.1. Component values for the single- and double-loop series circuits for the transformer-loop compact model of the 2.0nH spiral.

Component	Port 1		Port 2	
	C-GC	C-GC-GC	C-GC	C-GC-GC
C_{ox}	53.02 fF	58.82 fF	51.55 fF	51.97 fF
R_{sub1}	69.75 Ω	31.60 Ω	83.66 Ω	14.38 Ω
C_{sub1}	292.04 fF	300.07 fF	213.97 fF	4.73 fF
R_{sub2}	—	399.78 Ω	—	87.34 Ω
C_{sub2}	—	360.15 fF	—	308.70 fF

TABLE 4.2. Component values for the C-GC and C-GC-GC shunt circuits for the transformer-loop compact model of the 2.0nH spiral.

4.2. Octagonal Spiral on Low-Loss Substrate

To further test the versatility of the scalable PEEC model, a comparison is made with measurements from a 4.3nH octagonal spiral inductor on low-loss substrate. A representation of the layout is pictured in Figure 4.12. In this case the spiral consists of 6.5 turns. The underpass has been omitted to clarify the figure. This spiral inductor was fabricated on a non-epi BiCMOS process with a

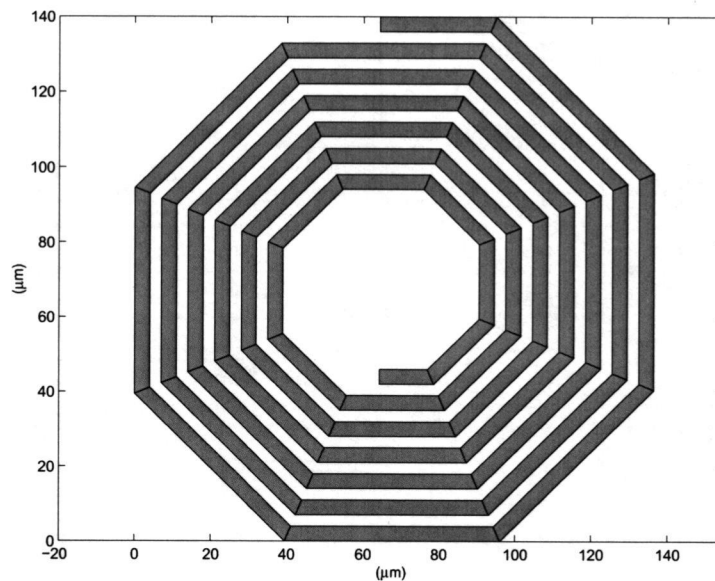


FIGURE 4.12. Layout of the 4.3 nH octagonal spiral inductor on low-loss substrate.

bulk conductivity of approximately 10 S/m. With this type of substrate, the eddy currents are negligible and $[L]_{image}$ is purely real. The spiral has been built using a

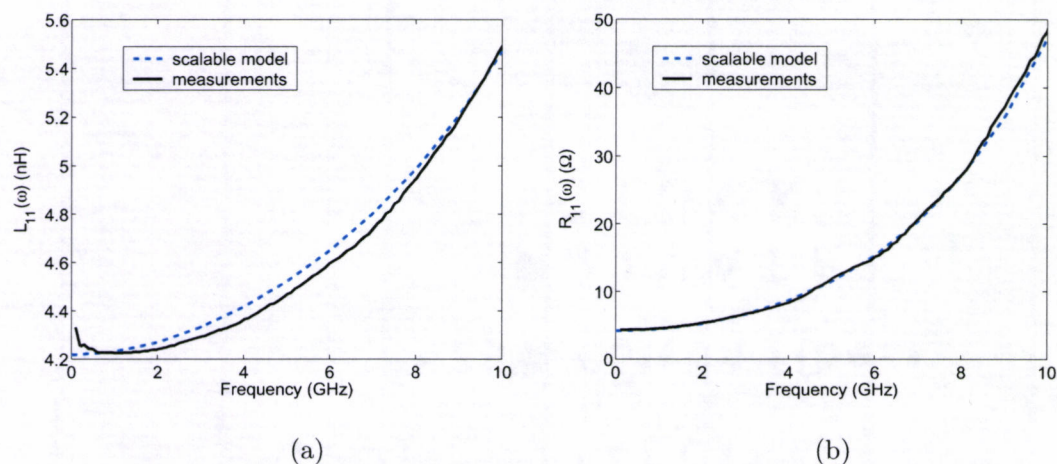


FIGURE 4.13. $L_{11}(\omega)$ and $R_{11}(\omega)$ for the 4.3nH spiral compared with PEEC model results.

thick “inductor-metal” layer at the top of the metal-dielectric stack. The underpass is fabricated in the next metal layer below the inductor.

To accurately model the non-uniform current distribution in this spiral, each segment was divided into 7 filaments along the width and 4 along the height direction. It is particularly important, in this case, to sub-divide in the vertical direction because of the interaction (i.e. proximity effect) between the underpass and the spiral metallization. For spirals on high-loss substrate, these effects are considered second-order and can often be ignored.

The total inductance and resistance looking into port one with port two shorted to ground can be seen in Figures 4.13(a) and (b). Again, the PEEC model is able to accurately predict the $Q_{11}(\omega)$ peak of approximately 13 at 4GHz. The series inductance and resistance are shown in Figure 4.15(a) and (b). The series inductance displays a trend quite different from the 2.0nH spiral, after an initial dip caused by the conductor skin-effect and proximity effects, the inductance begins to

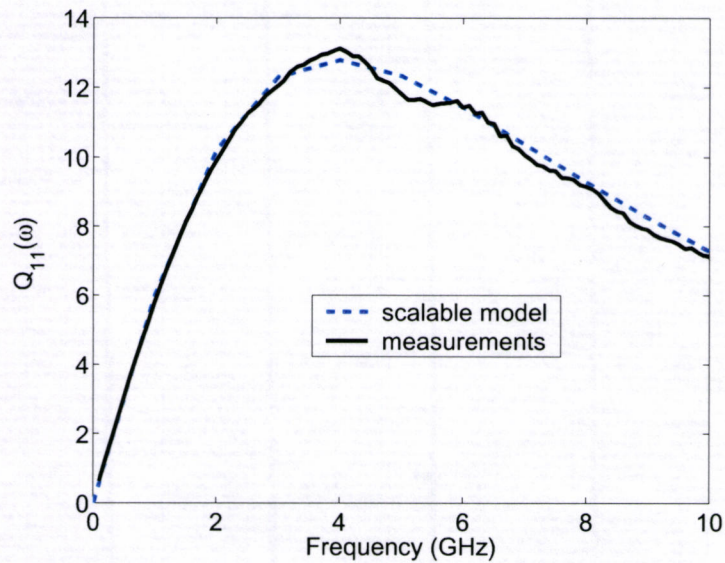


FIGURE 4.14. $Q_{11}(\omega)$ of the 4.3nH spiral compared with PEEC model results.

rise as the “series resonance” approaches. The shunt capacitance and conductance for port one of the 4.3nH spiral are shown in Figures 4.16 and 4.17, respectively.

4.3. Conclusion

Results for the scalable enhanced-PEEC model has been compared with measurements from two octagonal spiral inductors. The wide-band transformer-loop compact model was also extracted from and compared to measurements taken from the spiral inductor on high-loss substrate. The comparison shows that both models exhibit good accuracy over a 100MHz to 10GHz frequency range, in particular for the one-port L, R, and Q.

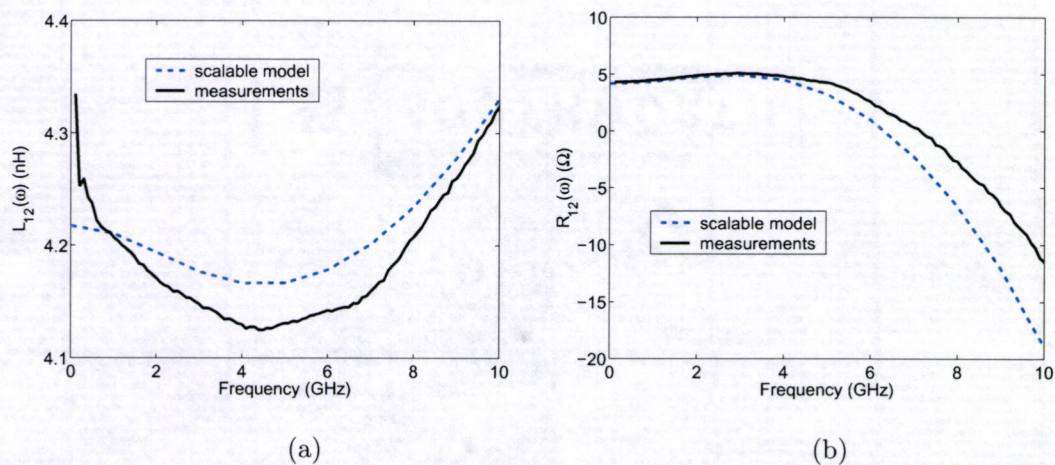


FIGURE 4.15. Frequency dependent partial inductance and resistance of coupled segments on silicon.

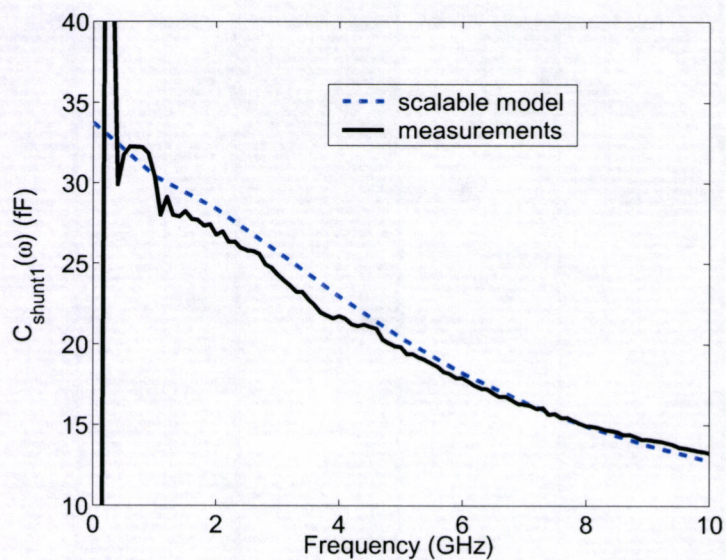


FIGURE 4.16. Shunt capacitance at port one of 4.3nH spiral compared PEEC model results.

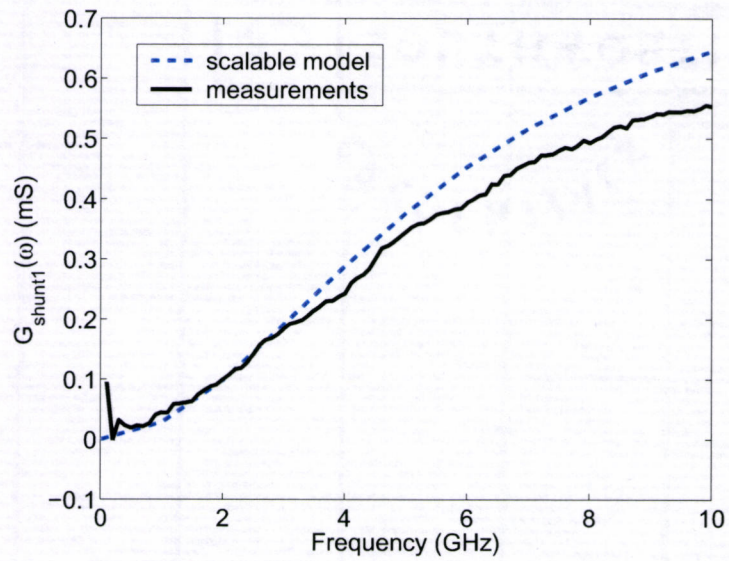


FIGURE 4.17. Shunt conductance at port one of 4.3nH spiral compared with PEEC model results.

5. CONCLUSIONS AND FUTURE RESEARCH

5.1. Conclusions

As wireless applications become increasingly popular, the demand for high quality on-chip spiral inductors has grown exponentially. The people behind that increased demand are, of course, the circuit designers who need accurate compact models for their circuit simulations. More importantly, the proposed spiral inductor that the compact model is extracted from should meet or exceed all of their expectations in terms of Q , inductance, etc. Much, if not all, of this work typically falls to the device engineer who often has limited resources for designing and modelling spiral inductors. This thesis presents a complete modelling methodology allowing a device engineer or circuit designer to design, test, and model on-chip spiral inductors for RF applications.

A scalable, predictive model, based on an enhanced PEEC formulation, was presented in chapter 2. The PEEC model utilizes a new complex-image technique to accurately include the eddy current losses affecting spirals on lossy silicon substrate. This flexible approach can provide frequency domain information such as $Q_{11}(\omega)$, $L_{11}(\omega)$, or $R_{11}(\omega)$ for a variety of spiral geometries and substrate configurations.

A new wide-band compact equivalent-circuit model for spiral inductors on high-loss substrates was presented in chapter 3. The new compact model is useful for frequency- or time-domain simulations in any popular circuit simulation program. Wide-band accuracy is achieved through the use of “transformer-loops” to model substrate and conductor losses. To further extend the usefulness of the transformer-loop compact model, a fast extraction technique was presented, based on a least-squares fitting technique.

Results for both the scalable and compact models were presented in chapter 4. Measurements from a 2.0nH octagonal spiral inductor on a high-loss epi-substrate were compared with results from the scalable PEEC model. A transformer-loop compact model was also extracted from the measurements for comparison. Good agreement was demonstrated over a 100MHz to 10GHz frequency range for both of the models. To further illustrate the versatility of the enhanced PEEC approach, a comparison with measurements from a 4.3nH octagonal spiral on a low-loss substrate is made. Again, good agreement is shown over the 100MHz to 10GHz frequency range.

5.2. Future Research

The future of this research lies mainly in two different directions: improving the scalable model and development of new compact modelling techniques.

The most immediate improvement to the scalable model will most likely be the development of a more flexible technique for calculating the partial capacitances and resistances coupling the segments to one-another and to ground. The present technique involving a transmission-line simulation is fast but ignores many second-order phenomena such as corner effects and coupling between the underpass and the spiral. A more versatile technique such as a Green's function method is a possibility.

To allow the scalable model to be used to its fullest design capabilities, more work must be done to provide an automated optimization methodology. In many cases, a design is desired where a peak Q is needed at a particular frequency with a limited amount of chip real-estate. This problem is classified as a constrained opti-

mization problem and many techniques could be adapted and improved to provide this capability to the scalable model presented in this thesis.

Another definite direction for the enhanced-PEEC scalable model will be the addition of new types of spiral inductor structures such as multi-layer spirals (series and shunt connections), transformer structures, and differential spiral inductors.

Similarly, future research for the wide-band compact modelling effort will involve the development of new compact models for transformers as well as differential spirals. Additionally, there is a high demand for compact models with the ability to demonstrate a significant phase delay. In general, a focus on a new class of compact models with variable complexity will be necessary to meet the demands of the wireless industry. New flexible extraction techniques optimized for robustness and either speed, or wide-band accuracy must also be developed to allow a faster design-cycle.

BIBLIOGRAPHY

- [1] T.S. Perry, "Kilby and the IC," *IEEE Spectrum*, pp.40-41, December 1988.
- [2] D.L. Harnage et al., "Current Status and Future Trends of SiGe BiCMOS Technology," *IEEE Trans. Electron Devices*, vol. 48, pp.2575-2594, November 2001.
- [3] J.M.C. Dukes, *Printed Circuits: Their Design and Application*, MacDonald, London, 1961.
- [4] R.M. Warner and J.N. Fordemwalt, Eds., *Integrated Circuits, Design Principles and Fabrication*, New York: McGraw-Hill, 1965, p.267.
- [5] G.C. Temes and J.W. LaPatra, *Introduction to Circuit Synthesis and Design*, New York: McGraw-Hill, 1977, pp.251-254.
- [6] E. Pettenpaul et al., "CAD Models of Lumped Elements on GaAs up to 18 GHz," *IEEE Trans. Microwave Theory Tech.*, vol. 36, pp.294-304, February 1988.
- [7] N.M. Nguyen, R.G. Meyer, "Si IC-Compatible Inductors and LC Passive Filters," *IEEE J. Solid-State Circuits*, vol. 25, pp.1028-1031, August 1990.
- [8] C.C. Tang et al., "Miniature 3-D Inductors in Standard CMOS Process," *IEEE J. Solid-State Circuits*, vol. 37, pp.471-480, April 2002.
- [9] T.K.K. Kan et al., "A 2-V 1.8-GHz Fully Integrated CMOS Dual-Loop Frequency Synthesizer," *IEEE J. Solid-State Circuits*, vol. 37, pp.1012-1020, August 2002.
- [10] T.K.K. Kan et al., "A 1.75-GHz Highly Integrated Narrow-Band CMOS Transmitter With Harmonic-Rejection Mixers," *IEEE J. Solid-State Circuits*, vol. 36, pp.2003-2015, December 2001.
- [11] T. Soorapanth and S.S. Wong, "A 0-dB IL 2140 \pm 30 MHz Bandpass Filter Utilizing Q-Enhanced Spiral Inductors in Standard CMOS," *IEEE J. Solid-State Circuits*, vol. 37, pp.579-586, May 2002.
- [12] J.N. Burghartz et al., "Microwave Inductors and Capacitors in Standard Multi-level Interconnect Silicon Technology," *IEEE Trans. Microwave Theory Tech.*, vol. 44, pp.100-104, January 1996.
- [13] J. Craninckx and M.S.J. Steyaert, "A 1.8-GHz Low-Phase-Noise CMOS VCO Using Optimized Hollow Spiral Inductors," *IEEE J. Solid-State Circuits*, vol. 32, pp.736-744, May 1997.

- [14] S. Jenei et al., "Add-on Cu/SiLK Module for High Q Inductors," *IEEE Electron Device Lett.*, vol. 23, pp.173-175, April 2002.
- [15] J.J. Zhou and D.J. Allstot, "Monolithic Transformers and Their Application in a Differential CMOS RF Low-Noise Amplifier," *IEEE J. Solid-State Circuits*, vol. 33, pp.2020-2027, December 1998.
- [16] A. Zolfaghari et al., "Stacked Inductors and Transformers in CMOS Technology," *IEEE J. Solid-State Circuits*, vol. 36, pp.620-628, April 2001.
- [17] S.M. Yim et al., "The Effects of a Ground Shield on the Characteristics and Performance of Spiral Inductors," *IEEE J. Solid-State Circuits*, vol. 37, pp.237-244, February 2002.
- [18] C.P. Yue and S.S. Wong, "On-Chip Spiral Inductors with Patterned Ground Shields for Si-Based RF IC's," *IEEE J. Solid-State Circuits*, vol. 33, pp.743-751, May 1998.
- [19] J.Y.C. Chang et al., "Large Suspended Inductors on Silicon and Their Use in a 2- μ m CMOS RF Amplifier," *IEEE Electron Device Lett.*, vol. 14, pp.246-248, May 1993.
- [20] H. Jiang et al., "On-Chip Spiral Inductors Suspended over Deep Copper-Lined Cavities," *IEEE Trans. Microwave Theory Tech.*, vol. 48, pp.2415-2423, December 2000.
- [21] C.H. Chen et al., "A Deep Submicron CMOS Process Compatible Suspending High-Q Inductor," *IEEE Electron Device Lett.*, vol. 22, pp.522-523, November 2001.
- [22] J. Zou et al., "Plastic Deformation Magnetic Assembly (PDMA) of Out-of-Plane Microstructures: Technology and Application," *Journal of Microelectromechanical Systems*, vol. 10, pp.302-309, June 2001.
- [23] J. Zou et al., "Development of Vertical Planar Coil Inductors Using Plastic Deformation Magnetic Assembly (PDMA)," *IEEE MTT-S International Microwave Symposium Digest*, pp.193-196, Phoenix, Arizona, May 20-25, 2001.
- [24] Agilent Technologies, Palo Alto, CA 94303, USA.
- [25] Sonnet Software, Inc., Liverpool, NY 13088, USA.
- [26] Ansoft Corporation, Pittsburgh, PA 15219, USA.

- [27] A.E. Ruehli, "Equivalent Circuit Models for Three-Dimensional Multiconductor Systems," *IEEE Trans. Microwave Theory Tech.*, vol. 22, pp.216-221, March 1974.
- [28] Cadence Design Systems Inc., San Jose, CA 95134, USA.
- [29] Y. Papananos and Y. Koutsoyannopoulos, "Efficient Utilization of On-Chip Inductors in Silicon RF IC design Using a Novel CAD Tool; The LNA Paradigm," *IEEE ISCAS '98 International Symposium on Circuits and Systems Proceedings*, pp.118-121, vol. 6, Monterey, California, May 31- June 3, 1998.
- [30] A.M. Niknejad and R.G. Meyer, *Design, Simulation, and Applications of Inductors and Transformers for Si RF ICs*, Kluwer Academic Publishers, 2000
- [31] J.R. Long, M.A. Copeland, "The Modeling, Design, and Characterization of Monolithic Inductors for Silicon RF IC's," *IEEE J. Solid-State Circuits*, vol. 32, pp.357-368, March 1997.
- [32] S.S. Mohan, M.d.M. Hershensen, S.P. Boyd, and T.H. Lee, "Simple Accurate Expressions for Planar Spiral Inductors," *IEEE J. Solid-State Circuits*, vol. 34, pp. 1419-1424, Oct. 1999.
- [33] R.D. Lutz, et al., "Modeling and analysis of multilevel spiral inductors for RFICs," *IEEE MTT-S International Microwave Symposium Digest*, vol. 1, pp. 43-46, 1999.
- [34] A. Weisshaar and H. Lan, "Accurate closed-form expressions for the frequency-dependent line parameters of on-chip interconnects on lossy silicon substrate," *IEEE MTT-S International Microwave Symposium Digest*, pp. 1735-1756, Phoenix, Arizona, May 20-25, 2001.
- [35] D.K. Cheng, *Field and Wave Electromagnetics, 2nd Ed.*, Addison-Wesley Publishing Company, 1992
- [36] M.N.O. Sadiku, *Numerical Techniques in Electromagnetics, 2nd Ed.*, CRC Press, 2001
- [37] A.E. Ruehli, "Inductance Calculations in a Complex Integrated Circuit Environment," *IBM J. Res. Develop*, pp.470-481, September 1972.
- [38] C. Hoer and C. Love, "Exact Inductance Equations for Rectangular Conductors With Applications to More Complicated Geometris," *J. Research, National Bureau of Standards-C. Engineering and Instrumentation*, Vol. 69C, No. 2, pp.127-137, April-June 1965.

- [39] F.W. Grover, *Inductance Calculations, Working Formulas and Tables.*, D. Van Nostrand Company, Inc., 1946.
- [40] R. Gharpurey, "Modeling and Analysis of Substrate Coupling in Integrated Circuits," *PhD Dissertation*, Department of Electrical Engineering and Computer Sciences, University of California at Berkeley, 1995.
- [41] A.E. Ruehli and P.A. Brennan, "Efficient Capacitance Calculations for Three-Dimensional Multiconductor Systems," *IEEE Trans. Microwave Theory Tech.*, vol. 21, pp.76-82, February 1973.
- [42] K. Nabors and J. White, "FastCap: A Multipole Accelerated 3-D Capacitance Extraction Program," *IEEE Trans. Computer Aided Design*, vol. 10, pp.1447-1459, February 1973.
- [43] M. Kamon et al., "FASTHENRY: A Multipole-Accelerated 3-D Inductance Extraction Program," *IEEE Trans. Microwave Theory Tech.*, vol. 42, pp.1750-1758, September 1994.
- [44] Y. C. Hahm, "Field theoretic analysis of a class of planar microwave and optoelectronics structure," *PhD Dissertation*, Department of Electrical and Computer Engineering, Oregon State University, Jan. 2000.
- [45] C.W. Ho et al., "The Modified Nodal Approach to Network Analysis," *IEEE Trans. Circuits and Systems*, vol. CAS-22, pp.504-509, June 1975.
- [46] J. Vlach and K. Singhal, *Computer Methods for Circuit Analysis and Design*, 2nd. Ed., Van Nostrand Reinhold, New York, 1994
- [47] H. Hasegawa, M. Furukawa, and H. Yanai, "Properties of microstrip line on Si-SiO₂ system," *IEEE Trans. Microwave Theory Tech.*, vol. 19, pp. 869-881, Nov. 1971.
- [48] J.N. Burghartz, D.C. Edelstein, K.A. Jenkins, and Y.H. Kwark, "Spiral Inductors and Transmission Lines in Silicon Technology Using Copper-Damascene Interconnects and Low-Loss Substrates," *IEEE Trans. Microwave Theory Tech.*, vol.45, Oct. 1997.
- [49] J. Zheng, V.K. Tripathi, and A. Weisshaar, "Characterization and Modeling of Multiple Coupled On-Chip Interconnects on Silicon Substrate," *IEEE Trans. Microwave Theory Tech.*, vol.49, Oct. 2001.

- [50] J. Zheng, Y.-C. Hahm, V.K. Tripathi, and A. Weisshaar, "CAD-Oriented Equivalent Circuit Modeling of On-Chip Interconnects on Lossy Silicon Substrate," *IEEE Trans. Microwave Theory Tech.*, vol.48, pp.1443-1451, Sept. 2000.
- [51] D. Melendy et al., "A New Wide-Band Compact Model for Spiral Inductors in RFICs," *IEEE Electron Device Lett.*, vol. 23, pp. 273-275, May 2002.
- [52] D. Melendy et al., "Wide-Band Compact Modeling of Spiral Inductors on RFICs," *IEEE MTT-S International Microwave Symposium Digest*, pp. 717-720, June 2002.
- [53] E.C.Levy, "Complex-curve fitting," *IRE Trans. Automatic Control*, vol. 4, pp.37-43, May 1959.
- [54] K.L. Choi, N. Na, and M. Swaminathan, "Characterization of Embedded Passives Using Macromodels in LTCC Technology," *IEEE Trans. Comp. Packag., Manufact. Technol. B*, vol.21, pp.258-268, Aug. 1998.
- [55] H. Anton and C. Rorres, *Elementary Linear Algebra, 8th. Ed.*, J. Wiley and Sons, Inc., 2000

APPENDICES

APPENDIX A. Integral Formulation for PEEC

Faraday's law can be stated in differential form as

$$\nabla \times \mathbf{E} = -\frac{\partial \mathbf{B}}{\partial t} \quad (\text{A1})$$

The vector magnetic potential \mathbf{A} can now be defined using the curl relationship

$$\mathbf{B} = \nabla \times \mathbf{A} \quad (\text{A2})$$

Equation (A2) is valid because of the solenoidal nature of \mathbf{B} ($\nabla \cdot \mathbf{B} = 0$). The vector magnetic potential can be combined with Faraday's law

$$\begin{aligned} \nabla \times \mathbf{E} &= -\frac{\partial}{\partial t}(\nabla \times \mathbf{A}) \\ \nabla \times \left(\mathbf{E} + \frac{\partial \mathbf{A}}{\partial t}\right) &= 0 \end{aligned} \quad (\text{A3})$$

The parenthetical portion of (A3) is curl-free, thus it can be expressed as the gradient of a scalar field. The scalar electric potential can be used, as this is consistent with the electrostatic case.

$$\mathbf{E} + \frac{\partial \mathbf{A}}{\partial t} = -\nabla V \quad (\text{A4})$$

At this point the total electric field is split into two parts: $\mathbf{E} = \mathbf{E}_o + \mathbf{E}'$ where \mathbf{E}_o is the applied electric field and \mathbf{E}' is the field induced by charges and currents in the circuit. With this understanding (A4) can be rewritten eq.A4

$$\begin{aligned} \mathbf{E} &= -\nabla V - \frac{\partial \mathbf{A}}{\partial t} \\ \mathbf{E}_o + \mathbf{E}' &= \mathbf{E}_o - \nabla V - \frac{\partial \mathbf{A}}{\partial t} \end{aligned} \quad (\text{A5})$$

It is also known that the total electric field must obey Ohm's law at all points in the circuit:

$$\mathbf{E} = \frac{\mathbf{J}}{\sigma} \quad (\text{A6})$$

where the conductivity σ can be a function of space coordinates. As such, (A5) and (A6) can be combined as

$$\begin{aligned} \mathbf{E}_o + \mathbf{E}' &= \mathbf{E}_o - \nabla V - \frac{\partial \mathbf{A}}{\partial t} = \frac{\mathbf{J}}{\sigma} \\ \mathbf{E}_o &= \nabla V + \frac{\partial \mathbf{A}}{\partial t} + \frac{\mathbf{J}}{\sigma} \end{aligned} \quad (\text{A7})$$

Where (A7) is the differential equation governing the PEEC modelling methodology.

APPENDIX B. Automated Layout of Spiral Inductors

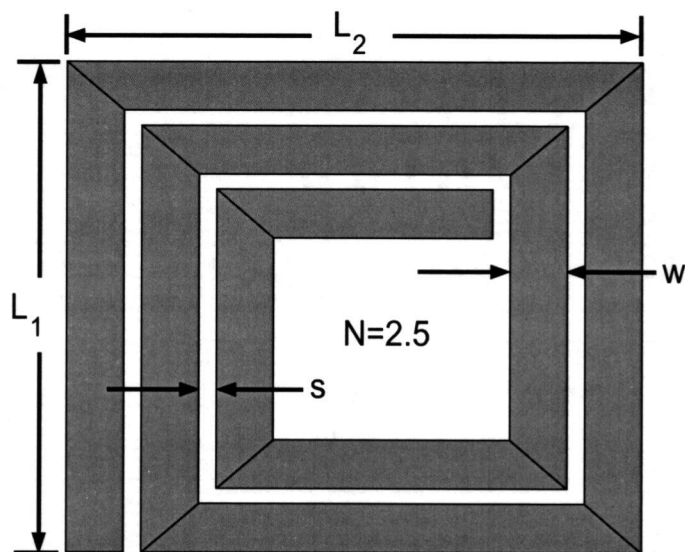


FIGURE B.1. Layout of 2.5 turn rectangular spiral inductor.

The PEEC method presented in chapter 2 obtains the frequency domain behavior of spiral inductors by replacing the spiral inductor with an equivalent circuit. To assemble the equivalent circuit for a particular inductor, the partial self- and mutual-inductances must be calculated between all segments of the spiral. This creates a need for the relative locations of all segments in the inductor. Commonly, this information is obtained from a layout file, typically in GDSII format, which can be time-consuming to create. To have a more efficient design-cycle, particularly for optimization, a fast method has been developed which finds the relative locations of all segments in a spiral inductor using a concise physical description. This method

is based on linear equations and has been applied to the rectangular and octagonal spiral inductor geometries. The technique is first described for the rectangular geometry and is then applied to the more complex octagonal geometry.

Figure B.1 shows the layout for a 2.5 turn rectangular spiral inductor. The physical information needed to automatically generate the layout has been labelled as w , the width of the conductors, s , the conductor spacing, L_1 , L_2 , the outer lengths of both sides, and N , the number of turns. The underpass layer has been neglected to clarify the important features. To find an equivalent circuit for this spiral inductor it is necessary to replace the ideal layout with an approximation as shown in Figure B.2, where black dots label the corresponding nodes of the equivalent circuit. This approach neglects the non-uniform currents that flow in the corners of the spiral inductor by extending the straight segments to meet at a mid-point. This simplifies the application of the PEEC method by allowing standard closed-form equations for partial inductance to be used. Four straight lines can be drawn which intersect the end-points of each of the segments as shown in Figure B.3. It can be shown that these lines are described by the following linear equations

$$y_1 = L_1 - x \tag{B1}$$

$$y_2 = L_1 - L_2 + x \tag{B2}$$

$$y_3 = L_2 - x \tag{B3}$$

$$y_4 = x - (w + s) \tag{B4}$$

The origin has been arbitrarily placed at the lower left-hand corner of the outermost segment resulting in positive co-ordinates for all segments. The x-coordinates of the vertical segments can be found by inspection and used as inputs to the linear equations to find the proper Y co-ordinates of the end-points. The end-points of the

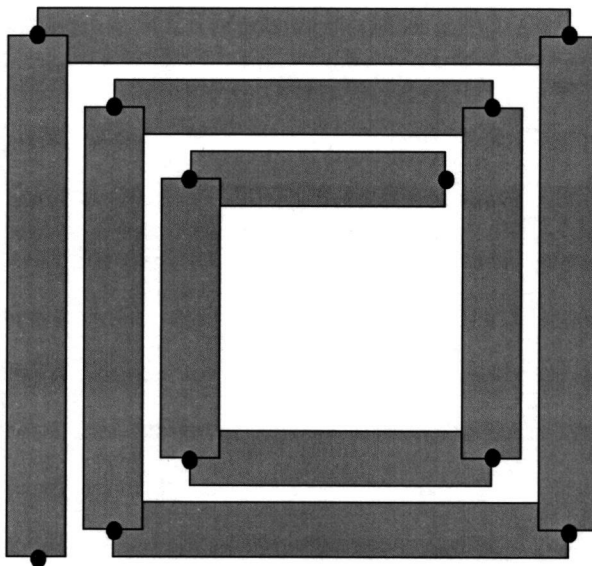


FIGURE B.2. PEEC approximation of 2.5 turn rectangular spiral inductor.

horizontal segments are then found from the end-points of the vertical segments. The coordinates of the very first and last nodes can be set to any suitable locations, with regard to applicable layout rules.

This technique can also be used with the enhanced PEEC approach which includes the proximity and conductor skin-effects. Figure B.4 shows the same four equations super-imposed on a 2.5 turn rectangular spiral inductor with each segment sub-divided into five filaments along the width. By extending each of the filaments end-points to meet at the lines, each segment becomes a stair-step approximation of a polygon.

This method has been extended to the case of octagonal spiral inductors as shown in Figure B.5. The physical parameters needed to automatically create the

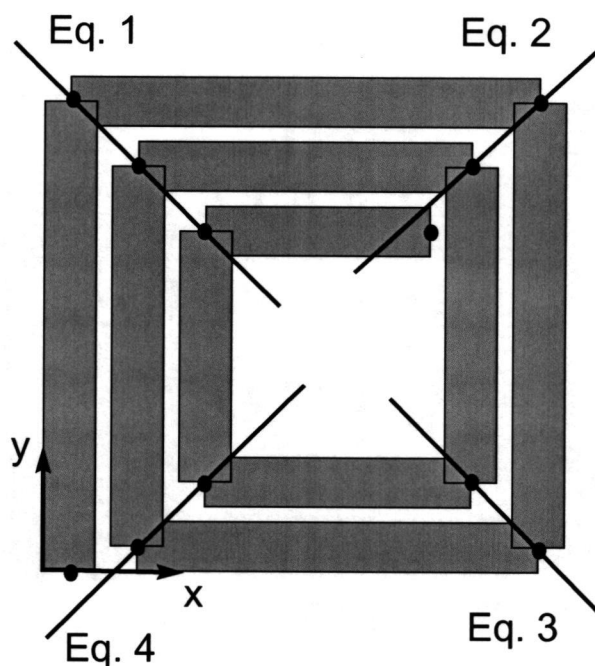


FIGURE B.3. Linear equations describing all end-points of the PEEC approximation for the rectangular spiral inductor.

layout are illustrated as N , the number of turns, w , the conductor width, L_h , the horizontal outer width, and s , the spacing between conductors. The ideal layout shown in Figure B.5 can be approximated using straight segments as shown in Figure B.6. Again, the segments have been extended to meet at the mid-point of the corners. Black dots have been used to indicate the nodes of the equivalent circuit. Eight lines can be drawn which intersect all of the connection nodes for the PEEC layout as shown in Figure B.7. These lines can be written as linear equations, $y = m_i x + b_i$, where the slopes and Y-intercepts are

$$m_1 = -(1 + \sqrt{2}) \quad (\text{B5})$$

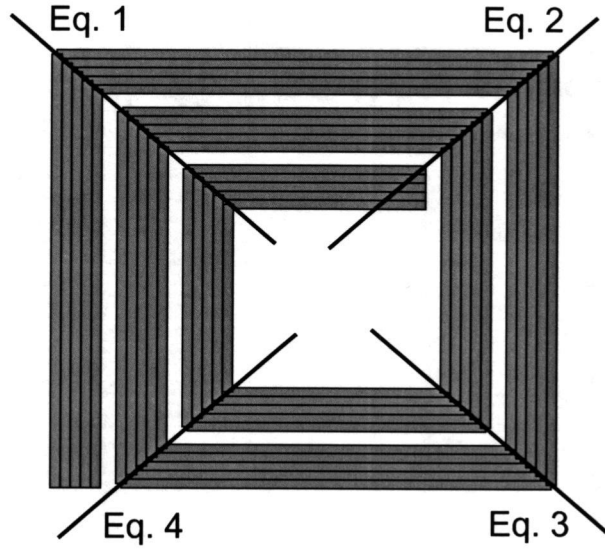


FIGURE B.4. Filamental PEEC approximation of the 2.5 turn rectangular spiral inductor.

$$b_1 = - \left(13 + \frac{19}{\sqrt{2}} \right) \Delta + \left(2 + \frac{3}{\sqrt{2}} \right) \Omega \quad (\text{B6})$$

$$m_2 = (1 + \sqrt{2}) \quad (\text{B7})$$

$$b_2 = \left(9 + \frac{11}{\sqrt{2}} \right) \Delta - \left(1 + \frac{1}{\sqrt{2}} \right) \Omega \quad (\text{B8})$$

$$m_3 = \sqrt{2} - 1 \quad (\text{B9})$$

$$b_3 = \left(\frac{1}{\sqrt{2}} \right) \Delta + \left(2 - \frac{3}{\sqrt{2}} \right) \Omega \quad (\text{B10})$$

$$m_4 = 1 - \sqrt{2} \quad (\text{B11})$$

$$b_4 = - \left(4 + \frac{3}{\sqrt{2}} \right) \Delta + \left(1 + \frac{1}{\sqrt{2}} \right) \Omega \quad (\text{B12})$$

$$m_5 = -(\sqrt{2} + 1) \quad (\text{B13})$$

$$b_5 = - \left(9 + \frac{13}{\sqrt{2}} \right) \Delta + \left(2 + \frac{3}{\sqrt{2}} \right) \Omega \quad (\text{B14})$$

$$m_6 = \sqrt{2} + 1 \quad (\text{B15})$$

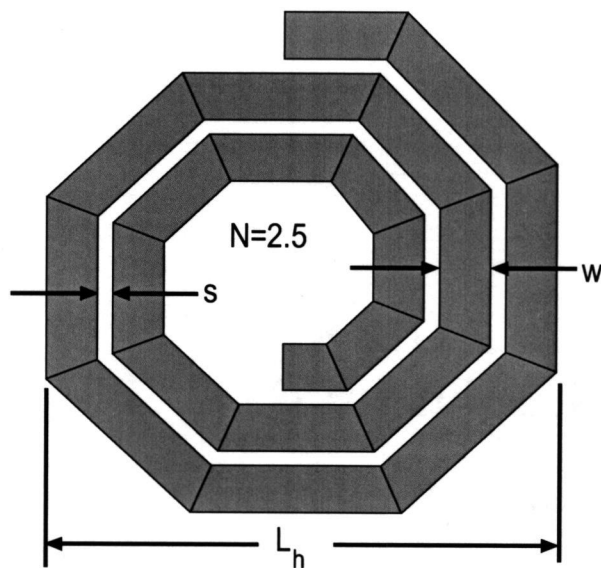


FIGURE B.5. Layout of 2.5 turn octagonal spiral inductor.

$$b_6 = \left(5 + \frac{5}{\sqrt{2}}\right) \Delta - \left(1 + \frac{1}{\sqrt{2}}\right) \Omega \quad (\text{B16})$$

$$m_7 = \sqrt{2} - 1 \quad (\text{B17})$$

$$b_7 = -\left(\frac{5}{\sqrt{2}}\right) \Delta + \left(\frac{1}{\sqrt{2}}\right) \Omega \quad (\text{B18})$$

$$m_8 = 1 - \sqrt{2} \quad (\text{B19})$$

$$b_8 = -\left(6 + \frac{5}{\sqrt{2}}\right) \Delta + \left(1 + \frac{1}{\sqrt{2}}\right) \Omega \quad (\text{B20})$$

$$(\text{B21})$$

and Δ and Ω are given by

$$\Delta = \frac{w + s}{4 + \frac{8}{\sqrt{2}}} \quad (\text{B22})$$

and

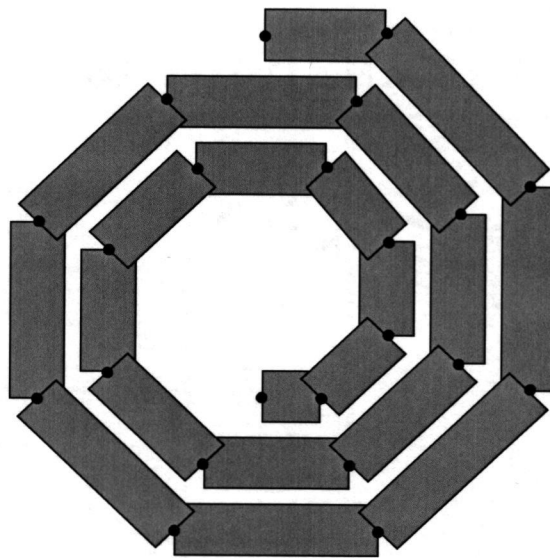


FIGURE B.6. PEEC approximation of 2.5 turn octagonal spiral inductor.

$$\Omega = \frac{L_h + w + s}{1 + \frac{2}{\sqrt{2}}} \quad (\text{B23})$$

These equations assume that the origin is located in the lower left-hand corner of the layout, this gives positive coordinates for all end-points.

The eight linear equations can be used similarly to the equations given for the rectangular case. Here, the vertical and horizontal segments have x- and y-coordinates that can be found by inspection. Equations 1, 2, 5, and 6 can be inverted to give the x-coordinates of the nodes for the horizontal segments, while equations 3, 4, 7, and 8 can be used to obtain the y-coordinates of the nodes for the vertical segments. The coordinates for the angled segments can then be obtained from the end-points of the vertical and horizontal segments.

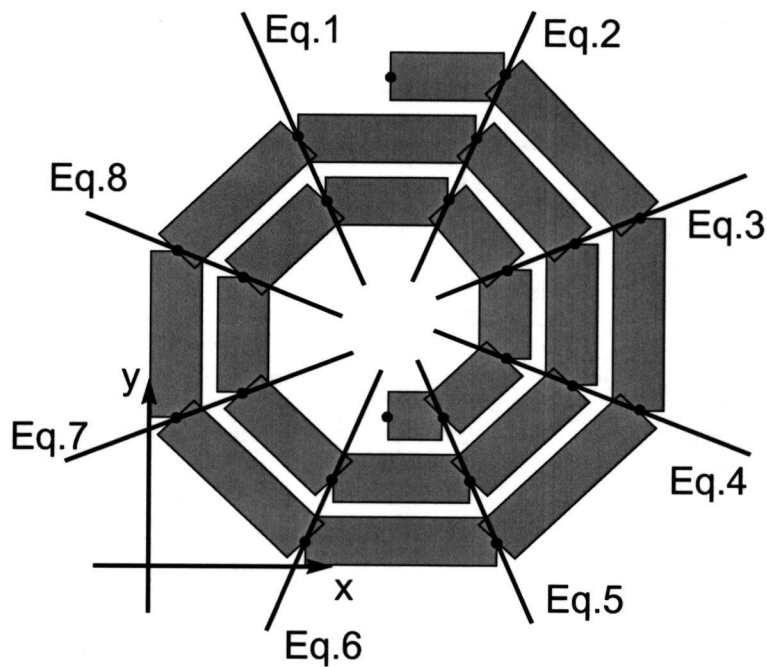


FIGURE B.7. Linear equations describing all end-points of the PEEC approximation for the octagonal spiral inductor.

This method can be used with the enhanced PEEC technique where each segment is divided into multiple filaments. Figure B.8 illustrates the relationship between the filament nodes and the linear equations.

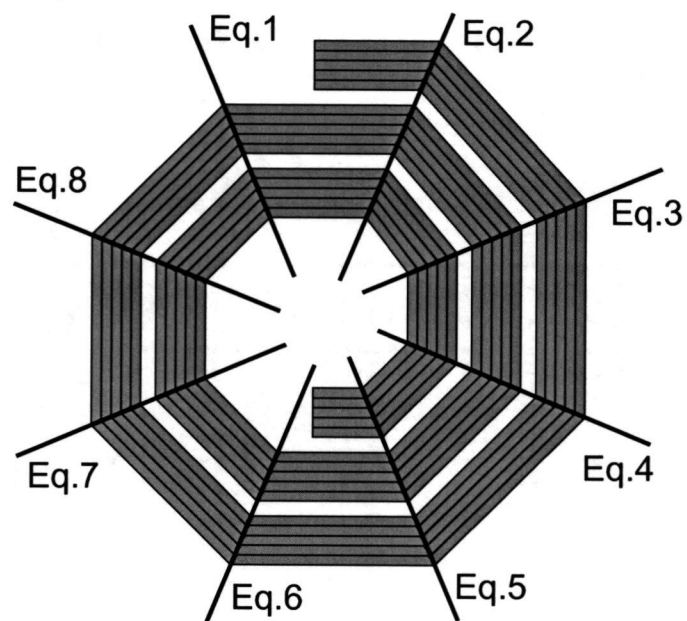


FIGURE B.8. Filamental PEEC approximation of the 2.5 turn octagonal spiral inductor.

APPENDIX C. Partial Inductance Formulas

The research presented in this thesis makes use of several different formulas for partial inductance. These formulas can be divided into two categories: formulas for parallel conductors and formulas for angled conductors. The formulas for parallel conductors are presented first.

C.1. Formulas for Parallel Conductors

C.1.1. Parallel Rectangular Bars

The following formula is useful for calculating the self- and mutual-inductance of rectangular bars, [38]

$$\begin{aligned}
 M = \frac{\mu_0}{4\pi abcd} & \left[\left[\left(\frac{y^2 z^2}{4} - \frac{y^4}{24} - \frac{z^4}{24} \right) x \ln \left(\frac{x + \sqrt{x^2 + y^2 + z^2}}{\sqrt{y^2 + z^2}} \right) \right. \right. \\
 & + \left(\frac{x^2 z^2}{4} - \frac{x^4}{24} - \frac{z^4}{24} \right) y \ln \left(\frac{y + \sqrt{x^2 + y^2 + z^2}}{\sqrt{x^2 + z^2}} \right) \\
 & + \left. \left. \left(\frac{y^2 x^2}{4} - \frac{x^4}{24} - \frac{y^4}{24} \right) z \ln \left(\frac{z + \sqrt{x^2 + y^2 + z^2}}{\sqrt{y^2 + x^2}} \right) \right. \right. \\
 & + \frac{1}{60} (x^4 + y^4 + z^4 - 3x^2 y^2 - 3y^2 z^2 - 3z^2 x^2) \sqrt{x^2 + y^2 + z^2} \\
 & - \frac{xyz^3}{6} \tan^{-1} \left(\frac{xy}{z\sqrt{x^2 + y^2 + z^2}} \right) - \frac{xy^3 z}{6} \tan^{-1} \left(\frac{xz}{y\sqrt{x^2 + y^2 + z^2}} \right) \\
 & \left. \left. - \frac{x^3 yz}{6} \tan^{-1} \left(\frac{yz}{x\sqrt{x^2 + y^2 + z^2}} \right) \right]_{E+d-a, E}^{E-a, E+d} (x) \right]_{P+c-b, P}^{P-b, P+c} (y) \right]_{l_3+l_2-l_1, l_3}^{l_3-l_1, l_3+l_2} (z) \quad (C1)
 \end{aligned}$$

Equation (C1) has been modified to give inductance in henries if the input parameters are in meters. Figure C.1 shows the relative positions of two rectangular bars

with all of the information needed to calculate the mutual inductance using (C1). E , P , or l_3 can be positive or negative depending on the quadrants of the two conductors. Self-inductance can be found by calculating the mutual inductance of two identical bars in the same location, i.e. $E = 0$, $P = 0$, and $l_3 = 0$. Because of

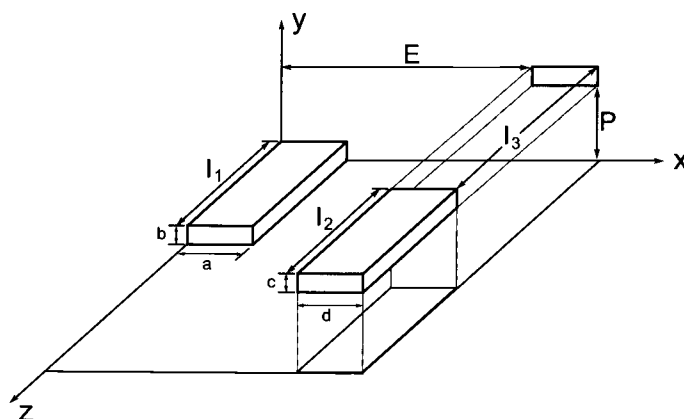


FIGURE C.1. Parallel rectangular bars.

the complexity of the calculation involved, a short-hand notation has been used to simplify (C1). Equation (C2) shows how to correctly interpret (C1).

$$\left[\left[\left[f(x, y, z) \right]_{q_1, q_3}^{q_2, q_4} (x) \right]_{r_1, r_3}^{r_2, r_4} (y) \right]_{s_1, s_3}^{s_2, s_4} (z) \equiv \sum_{i=1}^4 \sum_{j=1}^4 \sum_{k=1}^4 (-1)^{i+j+k+1} f(q_i, r_j, s_k) \quad (\text{C2})$$

Some caution must be exercised in using (C1). For cases where the distances between the bars, E , P , or l_3 , are large compared to the width, height, or length, of the bars, respectively, the resulting numerical noise can become significant.

C.1.2. Parallel Filaments

For cases in which the distance between the bars is large compared to the dimensions, the following filamental formula can be used with good accuracy, [39].

$$M = \frac{\mu_0}{4\pi} \left[\alpha \sinh^{-1} \frac{\alpha}{d} - \beta \sinh^{-1} \frac{\beta}{d} - \gamma \sinh^{-1} \frac{\gamma}{d} + \delta \sinh^{-1} \frac{\delta}{d} - \sqrt{\alpha^2 + d^2} + \sqrt{\beta^2 + d^2} + \sqrt{\gamma^2 + d^2} - \sqrt{\delta^2 + d^2} \right] \quad (\text{C3})$$

where

$$\alpha = l + m + \delta, \quad \beta = l + \delta, \quad \gamma = m + \delta. \quad (\text{C4})$$

Equation (C3) has been modified from the original version to give inductance in henries with inputs of meters. The input parameters for C3 are shown in Figure C.2. If the filaments overlap, δ becomes negative. Again, caution must be used

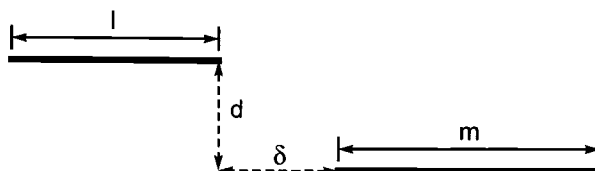


FIGURE C.2. Parallel filaments.

with this formula; for cases where the bars are in close proximity to each other, the filamental approximation can be inaccurate.

In general, for rectangular bars that are relatively close to each other, Equation (C1) should be used, while for distant bars, (C3) gives accurate results with a

fraction of the computation time needed.

C.2. Angled Conductors

All of the following formulas are for the filamental approximation due to the lack of closed-form equations for partial mutual inductance between angled rectangular bars. These formulas are taken from [39] with slight modifications to give inductance in henries when the input parameters are in meters.

C.2.1. Unequal Angled Filaments Meeting at a Point

Figure C.3 illustrates the first, and simplest, case of angled filaments with unequal lengths meeting at a point. The following formula gives the mutual inductance

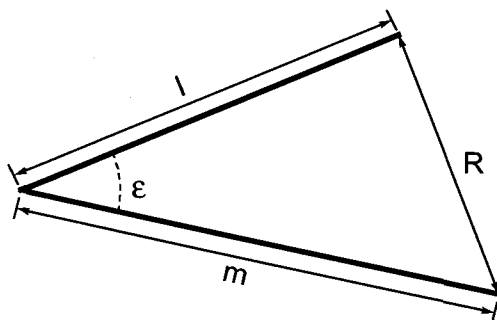


FIGURE C.3. Unequal angled filaments meeting at a point.

between the touching filaments.

$$M = \frac{\mu_0}{2\pi} \cos(\varepsilon) \left[l \tanh^{-1} \frac{m}{l+R} + m \tanh^{-1} \frac{l}{m+R} \right] \quad (\text{C5})$$

In some situations, only one of ε or R will be easily obtainable. The following equations demonstrate how ε can be calculated from R and vice versa.

$$\cos(\varepsilon) = \frac{l^2 + m^2 - R^2}{2lm} \quad (\text{C6})$$

$$\frac{R^2}{l^2} = 1 + \frac{m^2}{l^2} - 2\frac{m}{l} \cos(\varepsilon) \quad (\text{C7})$$

C.2.2. Unequal Angled Filaments in the Same Plane, Not Touching

Figure C.4 illustrates the case of filaments in the same plane without an intersection. Formula (C8) gives good accuracy for this case. All of the necessary

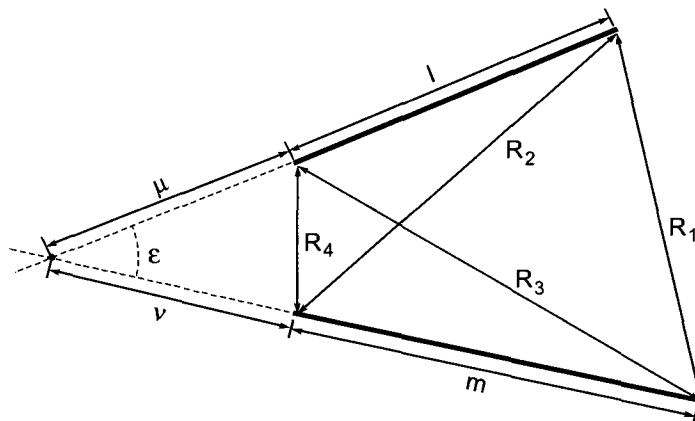


FIGURE C.4. Unequal angled filaments in the same plane, not touching.

input parameters are labelled in Figure C.4.

$$M = \frac{\mu_0}{2\pi} \cos(\varepsilon) \left[(\mu + l) \tanh^{-1} \frac{m}{R_1 + R_2} + (\nu + m) \tanh^{-1} \frac{l}{R_1 + R_4} - \mu \tanh^{-1} \frac{m}{R_3 + R_4} - \nu \tanh^{-1} \frac{l}{R_2 + R_3} \right] \quad (\text{C8})$$

In some situations, only ε , μ and ν or R_1 , R_2 , R_3 , and R_4 will be easily obtainable. The following equations demonstrate how ε , μ and ν can be calculated from R_1 , R_2 , R_3 , and R_4 .

$$\mu = \frac{2m^2l(R_2^2 - R_3^2 - l^2) + \alpha^2l(R_4^2 - R_3^2 - m^2)}{4l^2m^2 - \alpha^4} \quad (\text{C9})$$

$$\nu = \frac{2ml^2(R_4^2 - R_3^2 - m^2) + \alpha^2m(R_2^2 - R_3^2 - l^2)}{4l^2m^2 - \alpha^4} \quad (\text{C10})$$

$$\cos(\varepsilon) = \frac{\alpha^2}{2lm} \quad (\text{C11})$$

where

$$\alpha^2 = R_4^2 - R_3^2 + R_2^2 - R_1^2 \quad (\text{C12})$$

The following relationships can be used to find R_1 , R_2 , R_3 , and R_4 from μ , ν , and ε .

$$R_1^2 = (\mu + l)^2 + (\nu + m)^2 - 2(\mu + l)(\nu + m) \cos(\varepsilon) \quad (\text{C13})$$

$$R_2^2 = (\mu + l)^2 + \nu^2 - 2\nu(\mu + l) \cos(\varepsilon) \quad (\text{C14})$$

$$R_3^2 = \mu^2 + \nu^2 - 2\mu\nu \cos(\varepsilon) \quad (\text{C15})$$

$$R_4^2 = \mu^2 + (\nu + m)^2 - 2\mu(\nu + m) \cos(\varepsilon) \quad (\text{C16})$$

C.2.3. Unequal Angled Filaments in any Position, Not Touching

The most complex case of angled filaments is illustrated in Figure C.5. The

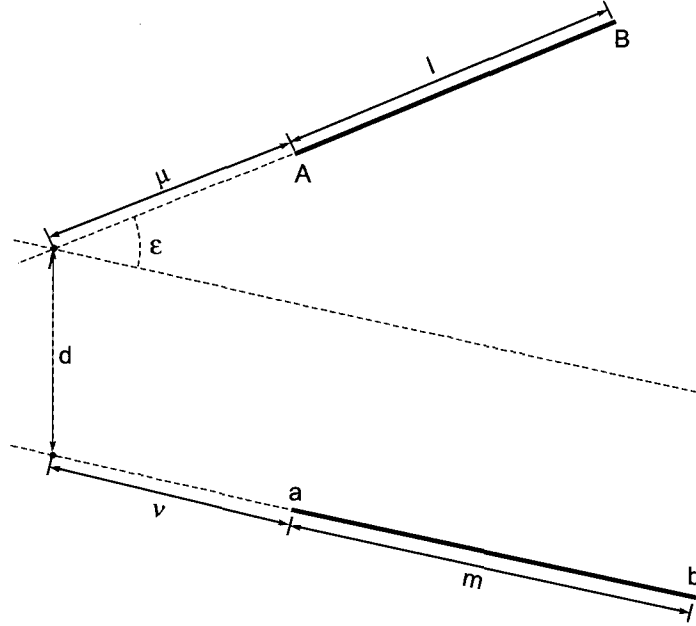


FIGURE C.5. Unequal angled filaments in any position, not touching.

following equation can be used to calculate the mutual inductance for this case.

$$M = \frac{\mu_0}{2\pi} \cos(\varepsilon) \left[(\mu + l) \tanh^{-1} \frac{m}{R_1 + R_2} + (\nu + m) \tanh^{-1} \frac{l}{R_1 + R_4} \right. \\ \left. - \mu \tanh^{-1} \frac{m}{R_3 + R_4} - \nu \tanh^{-1} \frac{l}{R_2 + R_3} \right] - \frac{\Omega d}{\sin(\varepsilon)} \quad (\text{C17})$$

where

$$\Omega = \tan^{-1} \left(\frac{d^2 \cos(\varepsilon) + (\mu + l)(\nu + m) \sin^2(\varepsilon)}{dR_1 \sin(\varepsilon)} \right) \\ - \tan^{-1} \left(\frac{d^2 \cos(\varepsilon) + (\mu + l)\nu \sin^2(\varepsilon)}{dR_2 \sin(\varepsilon)} \right) \\ + \tan^{-1} \left(\frac{d^2 \cos(\varepsilon) + \mu\nu \sin^2(\varepsilon)}{dR_3 \sin(\varepsilon)} \right) \\ - \tan^{-1} \left(\frac{d^2 \cos(\varepsilon) + \mu(\nu + m) \sin^2(\varepsilon)}{dR_4 \sin(\varepsilon)} \right). \quad (\text{C18})$$

In some situations, only ε , d , μ and ν or R_1 , R_2 , R_3 , and R_4 will be easily obtainable. The following equations demonstrate how ε , μ , ν , and d can be calculated from R_1 , R_2 , R_3 , and R_4 .

$$\mu = \frac{2m^2l(R_2^2 - R_3^2 - l^2) + \alpha^2l(R_4^2 - R_3^2 - m^2)}{4l^2m^2 - \alpha^4} \quad (\text{C19})$$

$$\nu = \frac{2ml^2(R_4^2 - R_3^2 - m^2) + \alpha^2m(R_2^2 - R_3^2 - l^2)}{4l^2m^2 - \alpha^4} \quad (\text{C20})$$

$$\cos(\varepsilon) = \frac{\alpha^2}{2lm} \quad (\text{C21})$$

$$d^2 = R_3^2 - \mu^2 - \nu^2 + 2\mu\nu \cos(\varepsilon) \quad (\text{C22})$$

$$\alpha^2 = R_4^2 - R_3^2 + R_2^2 - R_1^2 \quad (\text{C23})$$

The following relationships can be used to find R_1 , R_2 , R_3 , and R_4 from d , μ , ν , and ε .

$$R_1^2 = d^2 + (\mu + l)^2 + (\nu + m)^2 - 2(\mu + l)(\nu + m) \cos(\varepsilon) \quad (\text{C24})$$

$$R_2^2 = d^2 + (\mu + l)^2 + \nu^2 - 2\nu(\mu + l) \cos(\varepsilon) \quad (\text{C25})$$

$$R_3^2 = d^2 + \mu^2 + \nu^2 - 2\mu\nu \cos(\varepsilon) \quad (\text{C26})$$

$$R_4^2 = d^2 + \mu^2 + (\nu + m)^2 - 2\mu(\nu + m) \cos(\varepsilon) \quad (\text{C27})$$

In general, care must be taken when using Equations (C.3), (C.4), and (C.5). All of these equations involve trigonometric functions which can give the resulting mutual inductance a negative sign, regardless of the current directions. In any implementation, the most effective method to test the results of one of these equations is to compare the resulting mutual inductance of two filaments with a very small ε with the mutual inductance between two parallel filaments having the same lengths and spacing. As ε approaches zero, the mutual inductance should converge to the output of Equation (C3).